Thermoplastic polyurethanes. Domain morphology evolution under mechanical and thermal load as a function of composition

---

A thesis
submitted to the Department of Chemistry
in partial fulfilment of the requirements for
German academic degree Dr. rer. nat.
by
Farhad Jokari-Sheshdeh

University of Hamburg
2017 in Hamburg

The present copy of the dissertation is approved for publication on 03.Nov.2017

Reviewers/Gutachter

1. Prof. Dr. Almut Sandra Stribeck

2. Prof. Dr. Simone Mascotto

03.11.2017

Table of Contents

Nomenclature

$\mathbf{r} = (r_1, r_2, r_3)$ real space vector and its components

$\mathbf{s} = (s_1, s_2, s_3)$ reciprocal space vector and its components

$\rho(\mathbf{r})$ electron density

$I_{id}(s_{12}, s_3)$ scattering intensity of ideal multi-phase system

2θ scattering angle

Δ laplacian operator

$\gamma(\mathbf{r})$ autocorrelation function

$\{\}$ projection mapping

$\mathscr{F}_3$ 3D Fourier transform

$\mathscr{F}_3^{-1}$ inverse Fourier transform

μ linear absorption coefficient

$A(\mathbf{s})$ scattering amplitude

$g(r)$ Chord Length Distribution (CLD)

$g_1(r)$ Interface Distribution Function (IDF)

I_{Fl} fluctuation background

$P(\mathbf{r})$ Patterson function

Q scattering power

R sample-detector distance

v	volume fraction
$z(\mathbf{r})$	Chord Distribution Function (CDF)
1D	one-dimensional
2D	two-dimensional
3D	three-dimensional
HDO	1,6-hexanediol
PDO	1,3-propanediol
PTHF	polytetrahydrofuran

Abstract

In this work three groups of thermoplastic polyurethane (TPU) materials have been studied. In the first group, Machine-cast TPUs are strained and monitored by small-angle X-ray scattering (SAXS). In the second study TPUs with varying diisocyanates and chain extenders are strained and monitored by (SAXS). In the third study TPUs in presence of nucleating agents are monitored by SAXS under thermal load. Upon stretching hard domains are destroyed. Most stable are the domains of materials with Hard Segment Content (HSC)=30. Domain stability decreases with increasing HSC. Chord distribution functions (CDF) exhibit the same sequence of static long-period bands. The band positions form a Fibonacci series, related to the underlying polyaddition process. This indicates a nearly quasicrystalline arrangement of stringed hard domains, identified as the strain probes of the discrete SAXS. In the second study, the model-free data inspection shows the difference in nanoscopic straining mechanisms. From these results a one-dimensional morphological model for the analysis of the longitudinal SAXS is built. Its components are particle scattering and the two strongest scattering entities made of 2 hard domains with some soft phase in between (soft domain). Thus the model comprises 1 (solo) and 2 (duos). For all materials the average hard domains are about 6 nm high, and the domain heights vary by 38 to 48 percent. In the third study, two groups of TPUs based on polyester (ES) and polyether (ET) in presence of two classes of nucleating agents and without them are compared. By adding the nucleating agents to ET, the melting point results showed significant changes in comparison to ES materials. The ET without nucleating agent has a very inhomogeneous structure in melting process, with grains, which has a broad diameter distribution. In the solidification its phases are fairly homogeneous. The first nucleating agent (ET1) is melting as well as solidifying in the metastable phase. In (ET2) leads the second class of nucleating agents to homogeneity both in the melting and solidification. The ES shows a heterogeneous state in melting, which consist of many small grains and a few large ones. The heterogeneity increased during the melting process. The heterogeneity remains almost the same during solidification. The (ES1) shows a significant increase during solidification. The (ES2) shows a high 3D heterogeneity in melting, but during cooling it condenses into equal mass, that leads to a homogeneous phase.

Zusammenfassung

In dieser Arbeit wurden drei Gruppen von thermoplastischen polyurethanen (TPU) untersucht. In der ersten Gruppe wurde die Dehnung von TPUs mit Röntgenkleinwinkelstreuung (SAXS) analysiert. In der zweiten Gruppe wurden die TPUs mit unterschiedlichen Diisocyanate und Kettenverlängerungsmittel gedehnt und mit SAXS untersucht. Die Dritte Gruppe beinhaltete die Analyse von TPUs in Gegenwart von Nukleierungsmitteln unter thermischer Belastung mit SAXS. In der ersten Gruppe zerstörte Dehnung die harten Domänen der TPUs. Am stabilsten stellten sich Materialen mit einem Hartsegmentanteil (HSC) von 30 % heraus. Die Domänenstabilität reduzierte sich mit zunehmendem HSC. Chordverteilungsfunktionen (CDF) zeigten die gleiche Sequenz von statischen Langzeitbanden, wobei die Bandenpositionen eine Fibonacci-Folge bildeten, die auf den zugrunde liegenden Polyadditionsverfahren zurückgeführt werden kann. Dies deutet auf eine fast quasikristalline Anordnung der harten Domänen hin. In der zweiten Gruppe zeigte die modellfreie Datenkontrolle den Unterschied von Dehnungsmechanismen im Nanometerbereich. Aus diesen Ergebnissen wurde ein eindimensionales Modell für die morphologische Analyse auf der Längsachse des SAXS entwickelt. Die darin einfließenden Komponenten sind die Partikelstreuung und die beiden am stärksten streuenden Einheiten, bestehend aus zwei harten Domänen mit einer Weichdomäne dazwischen. Damit besteht das Modell aus 1 (solo) und 2 (Duo). Im Durchschnitt sind die harten Domänen aller Materialien dieser Gruppe etwa 6 nm hoch. Im dritten Abschnitt wurden TPU auf Polyethern (ET) und Polyesterbasis (ES) mit und ohne Zusatz von zwei Klassen von Nukleierungsmitteln (N1 und N2) miteinander verglichen. Das polyetherbasierte TPU ohne Nukleierungsmittel (ET) hat eine sehr inhomogene Schmelze mit ungelösten Teilchen Größen. Im festen Zustand sind seine Phasen recht homogen. Fügt man N1 zu, geht das Material (ET1) sowohl beim Heizen als auch beim Abkühlen durch den metastabilen Zustand einer sehr körnigen Schmelze. In ET2 führt das Nukleierungmittel zu Homogeneität sowohl in der Schmelze als auch im festen Material. Die polyesterbasierten TPUs zeigen immer Schmelzen mit vielen kleinen

aber wenigen großen grains. Bei der Probe auf Polyesterbasis bleibt diese Heterogeneität während des Abkühlens fast gleich. ES1 zeigt eine deutliche Zunahme beim Abkühlen. ES2 zeigt eine hohe 3D Heterogeneität in der Schmelze, die sich zu gleich großen Klümpchen verdichtet, dann aber zu einem Feststoff mit homogener Hart und Weichphase führt.

Chapter I

Introduction

1.1 Materials

Thermoplastic Polyurethane (TPU) is a class of polyurethanes with the special feature of being simultaneously melt-processable and elastic. TPUs are soft and processable when heated, hard when cooled and capable of being re-processed several times without losing their structural integrity. TPUs offer very good mechanical properties, such as high elongation, strength, and to some degrees good chemical resistance against oils and solvents. Therefore, TPUs are very popular across a wide range of markets and applications. TPUs can be extruded or injection molded on conventional thermoplastic manufacturing machines to produce solid components for footwear, cable and wire, hose and tube, film and sheet or other products. They can also be processed using organic solvents to form laminated textiles, protective coatings or functional adhesives[1].

1.2 General classification

There are many types of TPUs that are supplied as granules or pellets which can be converted into end-use items by conventional thermoplastic processing techniques. TPUs can generally be classified according to their chemical structure into two main types: polyether and polyester type.

TPUs can also be classified according to their production methods. There are three production methods currently in use to produce TPUs[1]:

- Batch
- Band-casting
- Reactive-Extrusion

TPUs are also be classified according to the processing method (e.g. injection, extrusion), form (e.g. film, sheet) or application area (e.g. automotive, footwear).

1.3 The Outstanding properties

- Mechanical behavior: TPUs have a combination of high elongation and tensile strength. In addition, they have high toughness and excellent abrasion and tear resistance[2]. The hardness range of TPUs can vary from as low as 10 shore A to greater than 75 shore D[1].

- Thermoplasticity: The TPUs thermal properties are outstanding in polyurethane family. To process TPUs requires repeat melt and freeze Cycles, using a combination of temperature and pressure. To produce TPUs it is necessary to build a high molecular weight linear polymer that will at the same time be both thermoplastic and yet has the required degree of toughness and high physical strength characteristics[2].

The combination of elasticity with thermoplasticity makes TPUs well known as a bridge between rubbers and thermoplastic materials.

1.4 Practical applications and the scientific question

The broad range of applications

TPUs provide a considerable number of physical property combinations making them an extremely versatile material adaptable for dozens of uses. TPUs can be sterilized, welded, colored, dyed, printed on, die-cut and slit. They have low-temperature flexibility and, in some grades, exhibit biocompatibility, hydrolytic stability, optical clarity, plus flame retardant and anti-static properties. These properties make TPUs extremely useful for many of the products. Some of the end-uses are shown in Table 1.1[1]

Table 1.1: End-use application for TPUs[1]

Application	Articles	Key Properties
Automotive	Protective films	Toughness, abrasion resistance, durability
	Adhesive films	flexibility, adhesive, low temperature
Clothing	Labels	Adhesive, fast crystallization, wash-ability
	Apparel	Adhesive, water resistance, light-weight
Fashion	Synthesis leather	Soft-touch, durability, light-weight, abrasion-resistance, elasticity, leather-like feel
Footwear	Bladder, Pumps	Elasticity, Toughness, heat stability, low air-permeability
Industrial Textile	Laminates	Strength, adhesive, abrasion resistance
	Conveyor belts	Elasticity, toughness, cut resistance
	Heat seal tape	High crystallinity, heat stability
Medical	Wound dressing, Surgical drapes	Flexibility, Moisture permeability, strength

Variability offers the possibility to tailor

The wide range of TPUs application refers to its outstanding properties. Adopting the properties of the final product according to the expected applications is a challenge in TPUs production.

TPUs are synthesized from various materials, that determine the properties of the final product. TPUs are typically produced by reacting a diisocyanate, a high molecular weight polyol, and a low molecular weight chain extender. Each component itself is a class of chemical structures that consist of a broad range of materials. To achieve a high elasticity in the final TPU, the materials must be interconnected or cross-linked in ways that allow them to return to their original shape

once the deforming force is removed[1]. The thermo plasticity relies almost exclusively on physical cross-links, that is derived from the thermodynamic incompatibility of the relatively non-polar segment and the polar segment. The non-polar segment made by polyol component (soft segment) and the polar segment made by diisocyanate+chain extender (hard segment). The incompatibility of segments causes to phase separation into microdomains of soft and hard domains[1,2].

To achieve the expected properties, it is necessary to control the component variables. It seems that the hard segment is one of the effective variables for the tailoring of TPU properties.

Tailoring in a multi-parameter system is a challenge

The effectiveness of the hard segment is simultaneously related to many parameters. The diisocyanate and the chain extender combine to form the hard segment structure. The ability to phase separate depends on both the structure and the weight fraction of the hard segment. In some cases, also additives are used to control the production process; like using nucleating agents to reduce the time of domain formation.

- Weight fraction of hard segment: By increasing the weight fraction of the hard segment, the average length of the hard segment becomes longer; in result, the phase separation will increase, that will change the mechanical properties[1].

- Structure of hard segment: The affinity between the hard segments is strongly related to the diisocyanate chemical structure. A symmetrical and planar structure and an aliphatic or aromatic structure has a great effect on packing the hard segments tightly together[1]. The chain extender as one part of the hard segment also has an impact on the structure of the hard segment. The chain extenders with an odd or even number of carbon atoms will change the packing of the hard domain. The chain extenders with an even number of carbons are represented to form straight hydrogen bonds between neighboring urethane groups in three dimensions, on the other hand the chain extender with an odd number of carbon in its structure have to contract into a higher energy conformation. As a result, they are low melting[1,3,4].

- Nucleating agents (as a function of processing conditions): The short time of domain formation or crystallization-time is very important for acceptable productivity for some applications, such as footwear[1,5]. A number of organic and inorganic compounds have been used as nucleating agents, i.e., crystallization initiators and accelerators that allow a higher degree of crystallization, smaller crystallites, and faster crystallization time. For that, polymer agent interaction must reduce the interfacial free-energy. Studies on the crystallization of TPUs in the presence of nucleating agents are hard to find[1].

Optimization of these parameters is a challenge to achieve the expected properties of the final product.

Systematic study and dependence of manufacturing and structure

The domains correlation during the process is key to answering the question, as to how we can modify the properties of TPUs for different demands. To this aim, it is important to have a morphological study on the domains under process.

- Under (mechanical) load

The TPUs nonlinear stress–strain behavior is initially stiff with a rollover yield to a more compliant response. In order to obtain a deeper understanding of the mechanical behavior of TPU, it is important to study the loading process with different techniques to study different aspects. The studies will result in in-situ quantitative and representative information which will help us gain a clear understanding of their morphology and structure.

- Under (thermal) process

The thermal process consists of melting and solidification. During melting the domains are destroyed and during solidification, the domains will form. The domain formation or the crystallization process can noticeably affect the morphology and, as a consequence, the physical and mechanical properties of semi-crystalline TPUs[1].

In this study it is tried to show the influence of the hard segment variables on the hard domains correlation during the physical changes. To approach this goal,

morphological studies are used to monitor the evolution of domain morphology of TPU samples with different hard segments under the mechanical and thermal process.

Chapter II

Background knowledge

2.1 The chemistry

TPUs are typically the product of a chemical reaction involving three components: a diisocyanate (aromatic or aliphatic), a polyol (or "macrodiol") and a chain-extender (diol or diamine), as illustrated in Figure 2.1 [5].

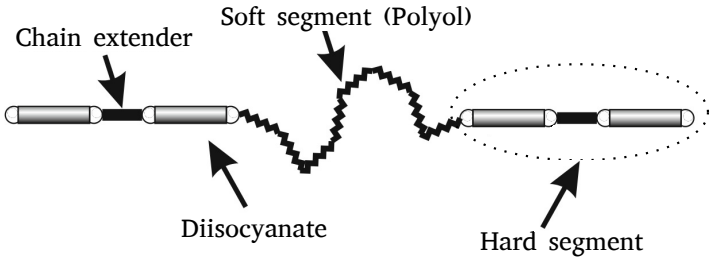

Figure 2.1: Structure of repeat of a typical TPU [5].

The resulting polymer is a copolymer of the "macrodiol" and "diisocyanate+chain-extender", which are named as the soft segment (SS) and the hard segment (HS), respectively. The reason for this naming is due to different thermal behavior of SS and HS. The SS glass transition is below ambient temperature, whereas the HS glass transition is above ambient temperature[2].

2.1.1 Diisocyanate

The high reactivity of the diisocyanate is the key to the chemistry of TPUs, that refer to electron deficiency of the central carbon atom in the isocyanate structure toward nucleophilic attack, then most reactions take place across the $C = N$ bond. The Structure becomes more important if an aromatic structure like benzene ring

distribute the negative charge on the nitrogen. As a general principle, any electron withdrawing group linked to the nitrogen atom will increase the partial positive charge on carbon and increase the reaction of the isocyanate group, conversely electron donating group will reduce the reactivity of diisocyanate[1,3].

In aromatic diisocyanates, the steric hindrance also plays an important role in reactivity of diisocyanates, the ortho substituents on aromatic isocyanate present lower reactivity in comparison to para substituents. Therefore both electronic and steric hindrances are important[1,2,6].

In this study three common diisocyanates, are used .

- MDI: or pure $4,4'MDI$ is a symmetrical molecule with two aromatic isocyanate groups of equal reactivity. Commercial products normally contain one to two percent $2,4'$ asymmetrical isomer.

- $H_{12}MDI$: is commercially available as a 90/10 blend of $4,4'/2,4'$ isomers. The predominant $4,4'$-diisocyanatedicyclohexylmethane consists of two conformational isomers, $cis-cis$, $cis-trans$.

- HDI: is a flexible, linear, symmetrical molecule with two primary aliphatic isocyanate groups of equal reactivity. Their reactivity is at least two orders of magnitude lower than these of MDI. Of all the commercially available polyisocyanates, it has the highest isocyanate content. Because it is aliphatic, it can be used in the manufacturing of light-stable polyurethanes. The three mentioned diisocyanate structures are given in figure 2.2.

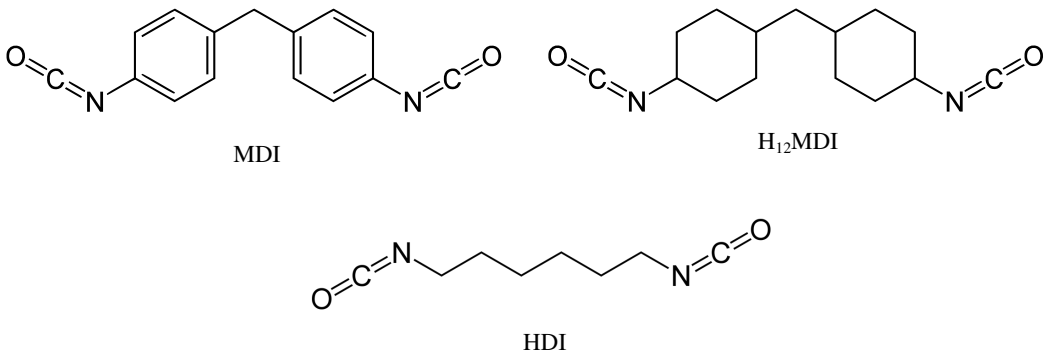

Figure 2.2: Aromatic and aliphatic, symmetric diisocyanate structure.

2.1.2 *Polyol*

In addition to the diisocyanate, it is the polyol that in a large part determines the properties of the final products.

The term "polyol" describes compounds with terminal hydroxyl groups that react with diisocyanates to produce the TPU. Typically, the "polyols" contain two reactive hydroxyl groups and have average molecular weights from 1000 to 2000 g/mol.

The two current classes of products are based on polyether and polyester polyols. The ether bond ($C-O$) in the polyether and the ester bond ($CO-O$) in the polyester is capable of hydrogen bonding with the urethane linkages ($NH-CO$) between neighbor chains. Polyesters are generally stronger hydrogen bond acceptors than polyethers. These general features are dependent upon the crystallinity or ordering of the SS , which is a function of molecular weight [7–9].

Polytetrahydrofuran ($PTHF$) used in this study is a polyether polyol.

- $PTHF$: or polytetrahydrofuran also called poly(tetramethylene oxide) is a chemical compound with formula $HO\left[(CH_2)_4O\right]_nH$. The product is sold under various trade names including Terathane from Invista and PolyTHF from BASF. The BASF plant in Ludwigshafen at one point was producing 250,000 metric tons per year[10]. It is manufactured by the cationic polymerization of tetrahydrofuran. The $PTHF$ is available commercially with molecular weights in the range 650 to 3000 and the polyols are waxy solids that melt into clear liquids at temperature in the range 28 to 40^o C. PTHF, in general, is less compatible with many diisocyanates especially MDI and the products derived from them show a higher degree of phase separation.[1]

2.1.3 *Chain-extender*

The chain-extenders are low molecular weight polyfunctional compounds, reacting with diisocyanates. The chain-extenders used in preparation of TPUs are difunctional glycols such as diols. The small diols react with diisocyanates and form the HS and serve as the physical crosslink for the polyurethane systems [1, 11].

The common chain-extenders in commercial TPUs are linear low-molecular-weight diols, such as 1,4-butanediol and 1,6-hexandiol[12].

There are numerous studies to indicate the effect of chain-extenders on the physical behavior of TPUs, most of them showed the role of symmetrical chain-extenders on hydrogen bonding[1,2,6].

2.1.4 Phase separation

Thermodynamic incompatibility between the HS and SS results in phase separation, and subsequent organization into hard and soft domains with a nanoscale texture, which gives TPUs their distinct mechanical properties and thermoplastic utility[2,13]. Figure 2.3 showed a schematic form of domains formation.

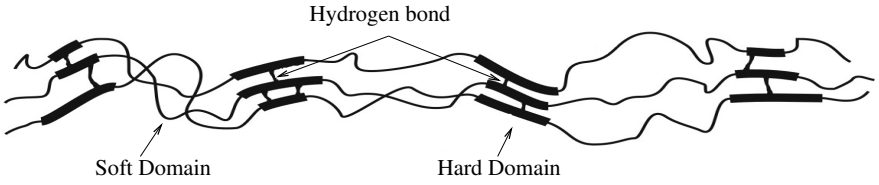

Figure 2.3: TPUs alternating hard segment (HS)–soft segment (SS) structure [5].

The shapes of the hard domains can be in the form of spheres with diameters of 5-20 *nm*, or long needles with 5 *nm* thickness and 50-300 *nm* length. The mean domain size increases from 10 to 20 *nm* as the HS content and the molecular weight of the polyol increases[2].

The degree of phase separation depends on several factors including, HS size and amount, the type of HS component (Diisocyanate, chain-extender) and the SS molecular composition and molecular weight. It is also influenced by the manufacturing process and reaction conditions [4,14,15]. TPU phase separation strongly depends on the hydrogen bond formation between the urethane linkage [2].

Hydrogen bonding The urethane groups link the HS and SS together by means of both covalent bonds and hydrogen bonds. Urethane groups are known for their ability to self-associate via hydrogen bonding, Figure 2.4. They form linear hydrogen bonds, in either a parallel or an anti-parallel way[3,16].

There are many studies to show the effect of hydrogen bonding on phase separation and the TPU properties. Tiffan and Terenzi found that almost all NH groups

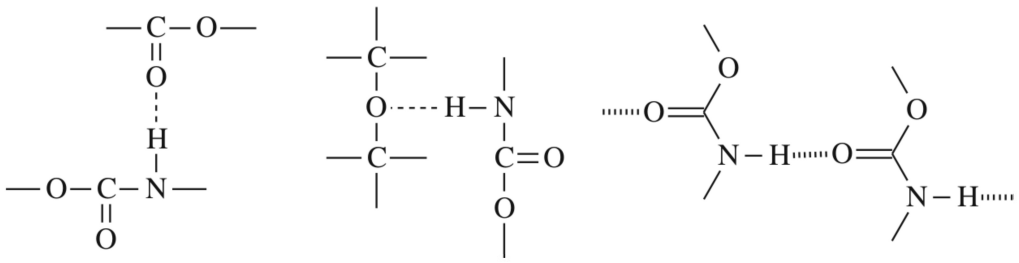

Figure 2.4: Hydrogen bonding interaction in polyurethanes [5].

at room temperature are hydrogen bonded [17]. Similar observations were made by Boyarchuk et al, both for polyether and polyester TPUs[18]. Mc Kiernan studied the influence of the hydrogen bonding on the crystallization behavior of a series of linear, aliphatic TPUs. The studies showed that hydrogen bonding influenced the crystallization process of the long-chain, aliphatic TPUs. X-ray, electron diffraction and infrared spectroscopy indicated that long alkane TPUs segments have inter-chain and inter-sheet distances similar to that observed for TPUs of higher hydrogen bonding densities. The hydrogen bonding controls the crystallization, packing, and morphology of such materials. In addition, high-temperature infrared studies showed the existence and high concentration (approximately 75%) of hydrogen bonding in such TPUs, even in the melt [19,20].

Annealing In order to obtain the ultimate dynamic properties the material needs to be annealed, Annealing favors stronger hydrogen bonds and improves the TPU melting points and their mechanical behavior as it determines a greater uniformity of the polymer network. The annealing temperature is generally just below the melting point of the hard domains and it reduces the amount of inter-phase material between the hard and soft domains[1]. Figure 2.5 shows an increase d_1 to d_2 in the size of the hard domain as a result of annealing.

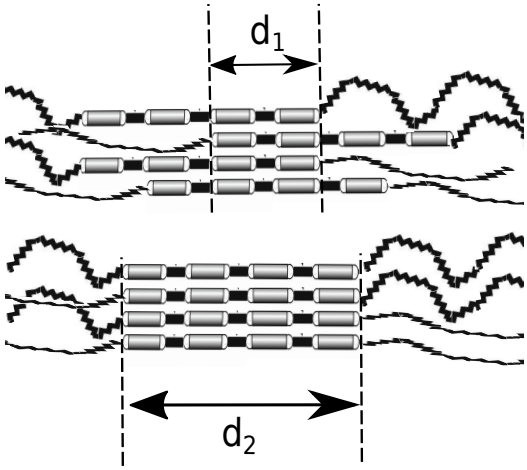

Figure 2.5: Schematic of hard domain before and after annealing [1].

2.2 The structure and morphology

Morphology studies determine the overall structure, the arrangement and micro scale ordering in space of materials. Understanding these important factors helps scientists efficiently process materials. Morphology also relates to physical properties like mechanical and thermal properties[6].

The morphology of TPUs is very complicated not only because of the two-phase system, but also because of other physical phenomena such as crystallization and hydrogen bonding in such systems[1,6]. The size of domains and crystallinity of phases, control the TPU morphology and macroscopic properties. Crystallization of the HS is an important effective parameter related to phase separation[1], it is dependent on the hydrogen bonding and other interactions between the HS to the hard domains [5]. The TPU morphology can be studied at different levels according to the separated domain sizes [8], which help us to obtain a clear understanding about the effect of some parameters on the properties of such polymers.

There are many morphological studies to clear the effect of HS variables on the TPU mechanical behavior. There are also some efforts to show the effect of nucleating agents on the thermal behavior of TPUs.

2.2.1 *Effect of hard segment content on mechanical behavior*

The overall mechanical properties depend on the relative weight fractions of soft and hard segments, and on the details of molecular packing in the phases, including the density of domains, which can be deeply studied in morphological studies.

For TPU structures with variable HS content, Li et al used various physical methods to study the morphology. They showed that the materials with HS content of 42%-67% consist of rod-like or lamella structure. At lower percentages, (<31wt %), the hard domains were dispersed in the SS matrix in the form of short cylinders or spheroids. At very high HS percentages, a morphology, with a dispersed SS phase was observed [2].

Abouzahr et al [21] studied the effect of the composition ratio of the HS. They observed that morphological changes occur as the HS fraction is increased. The texture changed from little HS content (15%) to the higher HS content (35% and 40%). Low hysteresis and high extension were obtained when isolated HS exist (25% HS). Thermal treatment of the samples leads to domain disruption and to HS-SS mixing.

Abouzahr and Wilkes also studied the effect of HS content on a series of MDI-based TPUs [21]. Depending on the HS content, the properties of the elastomers were divided into four regimes.

- At very low HS percentages, they found that the polymer was poorly phase separated and exhibited poor elastomeric properties.

- At slightly higher HS contents the polymer was more phase separated, but the HS were small and isolated. This lead to higher modulus, toughness and extensibility and consequently to low hysteresis.

- At percentages of 50% HS and higher, the phases inverted from hard domains in a soft matrix to soft domains in a HS matrix and the polymer became a brittle and high modulus plastic.

- At higher HS percentages, the hard domains grow and the material had a much higher modulus and hysteresis.

All studies evidenced, that at lower HS contents (22 wt%), the deformation mechanism involves the extension of the SS. The HS were randomly dispersed in a continuous soft domain without significant aggregation, which is why the alignment and break-up of the hard domain structures did not occur. The TPUs of a low HS composition (less than 30 wt%) were believed to have only discontinuous hard domains of a micellar nature in the SS solvent-like matrix. For TPU structures of a higher HS content (30 wt%), continuous hard domains could be clearly identified and traced in structural transitions. At higher HS content (33 wt%), the hard domains were observed to be still randomly dispersed in a continuous soft domain, which was reflected in higher inter-domain spacings. With increase of HS content, an interlocking HS morphology developed, leading to a decreasing average distance between the hard domains.

2.2.2 Effect of hard segment components on mechanical behavior

The mechanical behavior reflects the phase separation and density of hard domains. The phase separation is dependent on hydrogen bonding, that results from chemical variables of HS components[22]. There are many morphological studies to investigate the effects of the chemical compositions of HS and SS components on the behavior of TPUs.

Diisocyanate The first important parameter in diisocyanate chemical structure is the symmetrical and planarity structure. The diisocyanate symmetry has an influence on HS crystallinity. Materials showed good mechanical properties at room temperature [2].

Speckhard et.al[23], studied a series of H_{12}MDI based materials. Comparison of the properties of H_{12}MDI with the MDI based materials leads to several interesting conclusions. The H_{12}MDI materials, as expected, exhibited a much lower degree of hard segment ordering ascribed to the presence of hard segments which are formed from mixtures of the three isomeric forms of the diisocyanate. The H_{12}MDI based materials which contain smaller domains as measured by SAXS possessed better ultimate tensile properties than equivalent MDI based systems.

Ping et.al [24] studied the effect of different diisocyanates on material behavior. They focused on $2,4$-toluene diisocyanate (TDI), isophorone diisocyanate (IPDI),

hexamethylene diisocyanate (HDI), and MDI. The degree of phase separation or phase mixing are in the order of TDI (more mixed) < IPDI <MDI < HDI (more separated). The rigidity and strength of these frameworks are in the order of HDI > MDI > IPDI, but TDI-based HS can only form discrete domains dispersed in the continuous matrix. The first cycle of stretching and recovery does not show complete recovery ratio because of the damage in the hard domains caused by the stretching. After repeated stretching and recovery, no future damage of hard domains does occur, and therefore, the recovery ratio can reach 100%. Contracting stress measurements on stretched samples show that the maximum contracting stress is also HS dependent and is in the order of TDI < IPDI < MDI < HDI, indicating that the hard segment frameworks make a major contribution to the contracting stress by slowing down the stress relaxation.

Chain extender The study of the variation in TPU properties obtained by using different glycols with any given polymeric diol structure emphasized that increasing the distance between urethane groups (when using longer chain glycols) decreases the density and cohesive force between chains. This effect is coupled with the "odd-even" effect of chain fit. The "zigzag" pattern in tensile strengths and elongation is particularly evident in polyester based TPU [2]. The TPUs mechanical response varies with the length and type of the chain extender. The best mechanical behavior was observed in TPUs derived from diol chain extenders with even numbers of $-CH_2-$ groups. A TPU chain extended with "even" diols adopts the lowest energy fully extended conformation that allows hydrogen bonding and, therefore, a higher crystalline order, which explains why the materials based on 1,4-butanediol (BDO) and higher diols have better elastomeric properties. The HS based on these chain extenders crystallizes easier, therefore promoting phase separation[25].

Rausch [26], showed that the effect of the shorter chain extenders are less entangled and have less total force acting on them and slip more easily.

Song et al. studied the effect of diol chain extenders on tensile strength, they showed that BDO allows superior properties. they ranked the chain extenders according to their effect on strength in following order: 1,4-Butanediol >1,6-Hexanediol > 1,5-pentanediol> 1,3-propanediol> Ethylene glycol. However the differences are not very large [27].

2.2.3 Effect of nucleating agents on thermal behavior

Crystallization initiators and accelerators, so called nucleating agents, are used to achieve faster crystalisation and a higher degree of phase separation. The effect of the presence of nucleating agents on polymer crystallization has been partially studied [28] and several types of organic and inorganic compounds have been employed.

The interaction between the hard segments and the surface of the nucleating agent is essential in reducing the interfacial free energy barrier for spontaneous nucleating and growth, increasing phase separation rate and inducing it at a lower degree of supercooling, i.e. increasing the domain formation temperature [29].

Freitag et al [30] studied the effect of nucleating agent on the phase separation characteristics of TPUs. The results showed an increase in temperature and rate of phase separation of the studied TPUs and, consequently, reduced the formation time. Such effect was partly attributed to the formation of a larger number of domains in comparison to the neat TPU samples.

2.3 Methods for the study of the morphology

General methods In literature, there are abundant papers studying the polymer properties according their structure morphology relation. One can divide the methods into two groups according to the applied structure-analysis techniques:

- Direct observation of the structure in physical space
- Indirect observation by monitoring a structure related function

In the first method information about the morphology is directly obtained from the recorded data. The advantage of this method is its simplicity. However, in most cases it is not possible to record images simultaneously during the physical changes like mechanical or thermal tests. In the second method one has the possibility to perform in-situ measurements (e.g. scattering intensity) that can be related to the structure. The challenge of the indirect observation is the more complicated data-analysis compared to the direct methods. Therefore, one has to reduce the complexity of the morphology, in order to obtain simple models that

describe the dominant structure. This makes it possible to extract simple parameters that quantitatively describe the morphology.

X-ray scattering is the most versatile method for in-situ structure-characterization during deformation. This technique provides abundant information about structural variations from a molecular level up to several micrometers. Most of the above mentioned techniques provide complementary information to X-ray scattering data and are often applied in parallel with X-ray techniques. Next section briefly reviews application of X-rays for structure analysis of polymers. Due to the recent developments in powerful synchrotron sources, especially in the past decade, small-angle X-ray scattering (SAXS) techniques are becoming more favorable for researches to study the structural changes in polymers under deformation. Via the mentioned method, the domain destruction during deformation can be followed and investigated closely. On the other hand, the major downside of the scattering techniques, is its presentation of the information that is in reciprocal space. In other words, in order to have the information understandable to common human cognition, either a transformation of real space has to be carried out, or certain quantitative features have to be extracted directly from reciprocal space. Through the mentioned modifications, the results of SAXS can become comprehensible and its major drawback can be overcame.

2.4 TPUs structure studies by X-ray

In TPUs structure studies, SAXS is one of the important tools to make evidence of SS and HS phase separation. SAXS offers several important advantages and although interpretation is less direct than are the TEM or AFM techniques, the sample preparation for SAXS avoids the potential for staining artifacts that may arise with TEM[2]. X-rays are also less damaging to the samples than are the electron beams used in TEM, allowing measurements to be made continuously over many minutes. SAXS is used to characterize the domain structure in the size range of tens of nm. The scattering is related to morphology on the nanometer scale, but it originates from a relatively large volume (mm^3) of the material under investigation although micro beam techniques can sample smaller volumes. Therefore the results give a more statistically significant view of the morphology[31].

Numerous structural SAXS studies were done on TPUs. For example, ma-

terials achieved with MDI-diol based HS were studied by Bonart et al and by Wilkes and Yusek [32]. The X-ray patterns obtained by them showed a single Bragg reflection in the diffraction pattern of the poly(MDI-BD) hard segments at $d \approx 7.9\mathring{A}$, azimuthally inclined at 30^o to the meridian. In addition, an intense amorphous halo at $d \approx 4\mathring{A}$ was observed. Bonart assigned the Bragg reflection to planes inclined at 60^o to the fibre axis, and suggested that these planes arise from a staggering of adjacent chains so that intermolecular $C-O\cdots H-N$ hydrogen bonds are formed between the urethane groups. Koberstein and Stein [33] also studied the TPUs phase separation by using SAXS. The maximum in the small angle region was interpreted as the mean separation distance between the HS. The intensity profile contained information about the inter-facial thickness and about the purity of the domains.

By using wide-angle X-ray diffraction (WAXD) and SAXS, Bonart et al proposed a model according to which the HS were considered as extended chains. Later, on the basis of results from SAXS and thermal analysis, Koberstein and Stein[34]and Leung and Koberstein [35] proposed a model according to which the HS domain thickness was controlled by the shortest HS chain insoluble in the SS phase. They also observed that the HS mobility, and the strength of the HS interaction between themselves were influenced by the annealing temperature. For example, in materials derived from aromatic diisocyanates like MDI-BD based segmented TPUs, the HS mobility was low, and the HS interactions between them were strong, which resulted in slower phase separation after the melt was quenched to lower annealing temperatures. Koberstein et al [36] investigated a series of TPUs based on poly-ε-caprolactone SS and aromatic MDI:BD based HS. To assess the hard domain size on the TPUs morphology, Koberstein et al. used poly-ε-caprolactone SS because of its miscibility with the HS. Increasing the domain lengths, the position of the SAXS peak indicated phase separation, but only of short range order. This is consistent with a morphology with a short term order in the form of lamellar HS domains being dispersed in the SS continuous phase.

The main goal of this study is to achieve a clear understanding over the effects of strain field or thermal process on the structure of the hard domain in time. Theoretically, the hard domains are positioned in a certain distance from each other. With an increase in the strain, the hard domains will be aligned in the direction of the strain field or destruct. To investigate the aforementioned domains

during the uniaxial deformation, the SAXS patterns are evaluated by the chord distribution function (CDF). Later the evaluated SAXS patterns are investigated via the Interface distribution function (IDF) to show the changes in the sizes of the hard domains during deformation.

2.5 Theory of X-ray scattering

2.5.1 Nature and sources of X-rays

What are X-rays? X-radiation (composed of X-rays) are electromagnetic waves like visible light, but situated at the high energy/short wavelength end of the electromagnetic spectrum, between ultraviolet light and gamma rays. Their wavelength, at around a tenth of a nanometer, is comparable to inter atomic distances, which makes X-rays suitable for the study of atoms and bonds. X-rays were discovered by Röntgen in 1895. Today, they are used extensively in medical imaging because they have a high penetration depth through materials and are selectively absorbed by the parts of the body with the highest electron density such as bones. In Figure 2.6 the range of X-Ray and its application showed.

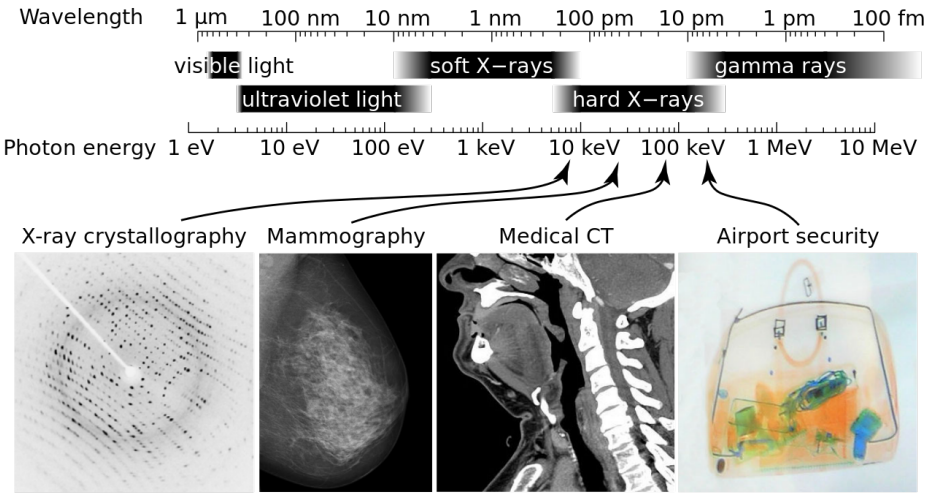

Figure 2.6: X-rays are part of the electromagnetic spectrum, with wavelengths shorter than visible light. Different applications use different parts of the X-ray spectrum[37].

Most X-rays have a wavelength ranging from 0.01 to 10 nanometers, a typical wavelength used for crystallography is $1\mathring{A}$ (0.1 nm), corresponding to frequencies in the range 30 petahertz to 30 exahertz ($3 \times 10^{16} Hz$ to $3 \times 10^{19} Hz$) and energies in the range 100 eV to 100 keV. X-rays with photon energies above 5–10 keV (below 0.2–0.1 nm wavelength) are called hard X-rays, while those with lower energy are called soft X-rays. Due to their penetrating ability, hard X-rays are widely used to image the inside of objects, e.g., in medical radiography and airport security. Since the wavelengths of hard X-rays are similar to the size of atoms they are also useful for determining crystal structures by X-ray crystallography. By contrast, soft X-rays are easily absorbed in air and the attenuation length of 600 eV ($2nm$) X-rays in water is less than 1 micrometer [38].

X-ray Sources The suitable wavelength range of X-rays for soft-matter studies are generated by two commonly used devices:

X-ray tubes, rotating anodes or metal-jet X-ray sources In-house or laboratory sources will produce X-rays using either an evacuated tube using a solid, a rotating anode, or even a liquid melted anode Figure 2.7, 2.8. The source emits X-rays from an anode target (typically copper), that is bombarded with electrons. The electrons are emitted from a cathode wire and accelerated by several tens of kVs across the vacuum towards the anode. Besides the Bremsstrahlung background, an X-ray tube emits radiation of a few wavelengths characteristic for the anode material, which result from electrons from distinct outer shells falling down into the vacancies in the inner shell caused by the electron bombardment (fluorescence). For instance, the most frequently used types of radiation in X-ray scattering, Cu Kα radiation, is caused by a transition of electrons from the L-shell to the K-Shell and has a wavelength of 0.154 *nm*.

When X-rays are produced by a rotating anode, the cathode and anode are housed under vacuum, in which the anode target rotates at high speed to efficiently distribute and dissipate heat. The wavelength of an in-house source such as a tube or rotating anode generator is fixed by the choice of anode target material and not tunable. The major disadvantage of the X-ray tube is the low efficiency, which is mainly due to the isotropic emission of X-rays from the target. Because a defined beam is required for scattering purposes, only a small portion of the radiation can

be used. The low photon flux leads to long exposure times to yield a sufficient signal to noise ratio. This renders time-resolved experiments and high-throughput measurements impossible. A more powerful alternative is the synchrotron light source.

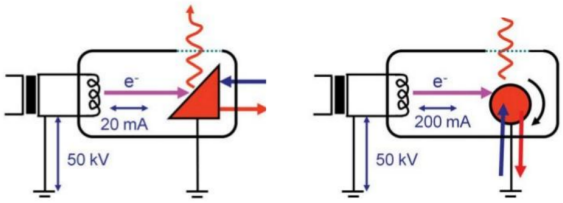

X-ray tube rotating anode

Figure 2.7: Common laboratory sources of X-rays

The Metal-jet x-ray tubes are conventional microfocus tubes with the solid-metal anode replaced by a liquid-metal jet Figure 2.8. That type of anode is continuously regenerated and already in the molten stage. Thereby, the classical power limit of an x-ray source, when the anode is permanently damaged by the electron beam, no longer applies. Especially in the microfocus x-ray spot size range, from about 5μm diameter to a few tens of μm, a source based on a liquid-metal-jet anode significantly outperform a classical solid anode x-ray source[39].

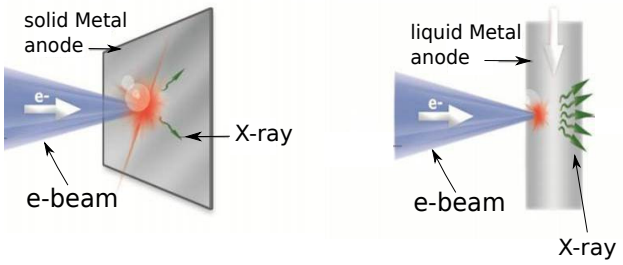

Figure 2.8: The Metal-jet x-ray sources[39].

Synchrotron In a synchrotron source, electrons or positrons are accelerated by a linear accelerator and booster and then fed into a storage ring, typically of a few hundred meters in diameter. The particles circulate in the storage ring at relativistic speeds. Being at energies around 5 to 8 GeV, $1 - \frac{v}{c} \approx 10^{-5}$ (with v being the particle speed and c being the speed of light) Figure 2.9.

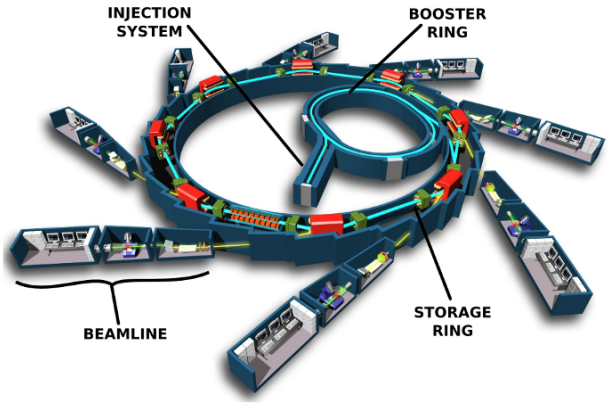

Figure 2.9: The four major components to any synchrotron facility. The injection system, the booster ring, the storage ring and the beamlines.

In the storage ring, bending magnets force the electrons to move in a circle. The deflection of charged particles causes radiation loss, which is emitted as X-rays. The loss of energy is compensated by acceleration cavities. Besides the bending magnets, other devices (wigglers and undulators) are purposefully inserted into the storage ring to generate more brilliant radiation. Wigglers can be regarded as periodic arrays of n bending magnets, such that the brilliance is $n2 \approx 100$ times higher than that of a bending magnet. Undulators, employed in 3^{rd} generation synchrotron, are designed similarly as wigglers, but take advantage of amplification effects by interferences between the emitted X-rays of individual magnets, such that their brilliance is again enhanced by two to three orders of magnitude. After the X-ray beam has left the storage ring in tangential direction, it passes through some optical devices, which focus the beam (by means of a Göbel mirror, slits or X-ray lenses) and confine the wavelength spread of the beam (only waves within a certain wavelength window fulfill the diffraction con-

ditions of the monochromator crystals) and finally arrive at the experimental hutch of the beamline. The difference in brilliance between a rotating anode lab source and the latest synchrotron sources is more than ten orders of magnitude. This high brilliance is especially useful for USAXS and SAXS. The exposure times at a synchrotron are reduced by a factor of 10^5 as compared to lab experiments, opening up new methods to study processes on previously inaccessible short time scales [40].

The intensity of X-rays generated by modern 3^{rd} generation synchrotron sources are so high that radiation damage to crystals has become a major concern, and this has given rise to the near-exclusive use of cryo-crystallographic techniques, in which crystals are kept at near-liquid nitrogen temperatures to minimize radiation damage. Synchrotron radiation has additional features that make it attractive for advanced applications. Because it is pulsed, it can be exploited for examining time-dependent phenomena, and because it is highly polarized, it can be used to examine polarization-dependent and angle-dependent effects [40].

The principal difference between synchrotron light and the X-rays used in hospital is the brilliance: a synchrotron source is ten thousand billion times brighter than a hospital X-ray source.

2.5.2 Scattering and diffraction

X-ray are used for identifying the atomic and molecular structure of a crystal, in which the crystalline atoms cause a beam of incident X-rays to diffract into many specific directions. By measuring the angles and intensities of these diffracted beams, a crystallographer can produce a three-dimensional picture of the density of electrons within the crystal. From this electron density, the mean positions of the atoms in the crystal can be determined, as well as their chemical bonds, their disorder and various other information.

X-ray crystallography is related to several other methods for determining atomic structures. Similar diffraction patterns can be produced by scattering electrons or neutrons, which are likewise interpreted by Fourier transformation. If single crystals of sufficient size cannot be obtained, various other X-ray methods can be applied to obtain less detailed information; such methods include fiber diffraction, powder diffraction and (even if the sample is not crystallized) small-angle X-ray

scattering (SAXS) [38].

In the usual synchrotron setup, sample and detector are placed in a line on the primary X-ray beam. The primary beam penetrates a relatively thin sample and the scattering pattern is recorded around the attenuated beam "in transmission". By means of a planar detector the scattering intensity $I(x,y)$ is recorded. The sample-detector distance, R, is the main parameter which controls the angular range in which the scattering is recorded. In fact, the area of X-ray scattering is subdivided into several sub-areas which are characterized by a typical range of scattering angles or distances R (Table 2.1) [41].

Table 2.1: Subareas of X-ray scattering as a function of the sample-detector distance R assuming a wavelength $\lambda \approx 0.15$ nm

Sub-areas	R[m]	Focus
WAXS	0.05 – 0.2	arrangement of chain segments
MAXS	0.2 – 1	liquid-crystalline structure
SAXS	1–3	nanostructure 3 nm – 50 nm
USAXS	6 – 15	nanostructure 15 nm – 2 μ m

The suitable sub-area for the study of the TPU domain morphology is SAXS. This is a consequence of the typical domain sizes and their distances from each other. Small-angle X-ray scattering (SAXS) is a small-angle scattering (SAS) technique using x-rays where the elastic scattering of X-rays (wavelength 0.1-0.2 nm) by a sample which has inhomogeneities in the nm-range, is recorded at very low angles (typically 0.1 - 10°). This angular range contains information about the shape and size of macromolecules in solution, characteristic distances of partially ordered materials and pore sizes.

SAXS is used for the determination of the microscale or nanoscale structure of particle systems in terms of such parameters as averaged particle sizes, shapes, distribution, and surface-to-volume ratio. Not only particles, but also the structure of ordered systems like lamella, and fractal-like materials can be studied. The method is accurate, non-destructive and usually requires only a minimum of sample preparation. Applications are very broad and include colloids of all types, metals, cement, oil, polymers, proteins, foods and pharmaceuticals and can be found in research as well as in quality control.

Geometry of Scattering Figure 2.10 presents schematically the normal transmission setup which is frequently used for in-situ X-ray scattering experiments [41].

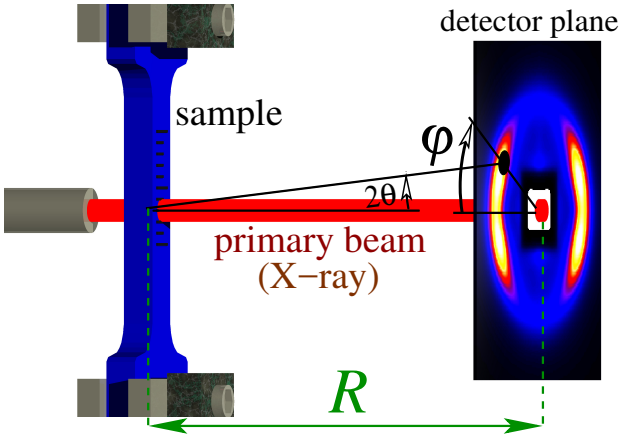

Figure 2.10: *Normal transmission setup* of an X-ray scattering experiment. The intensity at a chosen point (circular mark) on the planar detector, $I(2\theta,\varphi)$ is a function of the scattering angle 2θ and the azimuthal angle φ. R is the sample-detector distance [41]

Equation 2.1 shows the relation between the scattering-related coordinates, $(2\theta,\varphi)$, and the pixel coordinates (x,y) on the detector

$$\begin{aligned} \tan 2\theta &= \sqrt{x^2+y^2}/R \\ \tan\varphi &= y/x, \end{aligned} \tag{2.1}$$

with the scattering angle 2θ, and the azimuthal angle φ [41].

In an X-ray scattering experiment, we are interested in the relation of the measured scattering intensity to the structure inside the volume V that is irradiated by the X-ray beam. X-rays interact with the electrons of the materials, hence the structure is defined by the electron density $\rho(\mathbf{r})$ [41]. Here $\mathbf{r} = (r_1, r_2, r_3)$ is the vector in real space. X-rays are scattered when $\rho(\mathbf{r})$ varies inside the irradiated volume. Thus phases without electron-density-contrast cannot be distinguished by means of X-ray scattering.

As stated by the kinematic scattering theory the relation between the structure of matter and the scattered intensity can be best understood [41], if the latter is treated in the so-called reciprocal space $\mathbf{s} = (s_1, s_2, s_3)$, i.e.

$$I(2\theta,\varphi) \rightarrow I(\mathbf{s}) \tag{2.2}$$

Figure 2.11 shows the geometric relation between the sample coordinate system in real space, the reciprocal space and finally with the scattering intensity measured on the detector's plane. Analysis of Eq. 2.2 shows that it maps a plane into reciprocal space. The mapping is non-linear. The image of the infinite detector plane in reciprocal space is the surface (the vector $\mathbf{s}$ moves on the surface) of the sphere indicated in Figure 2.11.

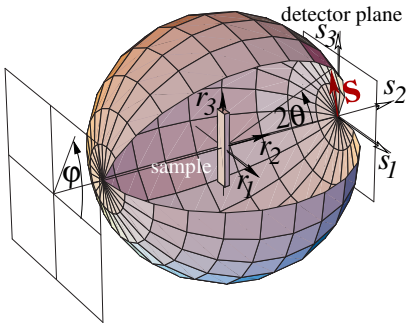

Figure 2.11: Experiment geometry, Ewald sphere, and reciprocal space. The sample is placed in the center of the sphere. Its structure is defined in the real-space coordinates, $\mathbf{r} = (r_1, r_2, r_3)$. The origin of reciprocal space, $\mathbf{s} = (s_1, s_2, s_3)$, is attached to the surface of the Ewald sphere. The orientation of its axes is strictly fixed to the orientation of the sample space $\mathbf{r}$. Each point on a plane detector (for clarity shifted to a position in front of the sphere) can be addressed by the two coordinates scattering angle, 2θ, and azimuthal angle, φ. The mapping of these two coordinates into reciprocal space is mediated by means of the surface of the Ewald sphere [41]

The sphere is known as the *Ewald sphere*. The sample in its real space coordinate system $\mathbf{r} = (r_1, r_2, r_3)$ is placed in the center of the Ewald sphere. The primary beam propagates from left to right. Assuming an infinitesimal irradiated volume V the scattering intensity $I(2\theta,\varphi)$ is observed. The origin of reciprocal space, $\mathbf{s} = (s_1, s_2, s_3)$, is attached to the point where the primary beam (after penetrating the sample) breaks through the Ewald sphere. The Cartesian axes of reciprocal space (s_1, s_2, s_3) are parallel to the axes (r_1, r_2, r_3) of the coordinate system of the real space. Thus by rotating the sample in the beam one can record the scattering intensity over a considerable fraction of reciprocal space, in which Ewald's sphere is the representation of the detector plane [41].

From the scattering pattern to the materials structure

The purpose of an in-situ X-ray measurement is to monitor the evolution of the materials structure in time. The main challenge of such experiments is the huge number of recorded patterns. Moreover, the scattering data is recorded in the reciprocal space. Thus direct analysis of the as-recorded patterns can be confusing or misleading. Therefore, a combination of theoretical tools– that transform the scattering data from the reciprocal space into the real space – and fast automated computer programs is required to be able analyze the structure evolution. In this section the theories will be discussed.

The magic square The fundamental relations between the electron density distribution inside the sample, $\rho(\mathbf{r})$, and the observed scattering intensity, $I(\mathbf{s})$ can be sketched [42] in a so called "magic square".

$$\begin{array}{ccccc} & & \rho(\mathbf{r}) & \overset{\mathscr{F}_3}{\Leftrightarrow} & A(\mathbf{s}) \\ & & \star 2 \Downarrow & & \Downarrow |\,|^2 \\ z(\mathbf{r}) & \underset{\Delta}{\Leftrightarrow} & P(\mathbf{r}) & \overset{\mathscr{F}_3}{\Leftrightarrow} & I(\mathbf{s}) \end{array} \tag{2.3}$$

According to the magic square, the real space electron density, $\rho(\mathbf{r})$, is converted into the scattering amplitude, $A(\mathbf{s})$, in reciprocal space by a 3D complex Fourier transform. The square of the absolute value of $A(\mathbf{s})$ gives the scattering intensity [42]:

$$I(\mathbf{s}) = |A(\mathbf{s})|^2 \tag{2.4}$$

The path from the scattering amplitude to the scattering intensity is a one-way path (depicted by a unidirectional downward arrow in Eq.). Thus the phase information of the structure is lost. This inhibits reconstruction of the absolute positions of individual domains (i.e. crystallites) in the material. Only relative distances among domains, i.e. their correlations can be determined [41, 42].

Going back to the real space is possible by performing an inverse Fourier trans-

form on the $I(\mathbf{s})$. The result of this operation is the so called *Patterson function*,

$$P(\mathbf{r}) = \mathscr{F}_3^{-1}(I(\mathbf{s})). \tag{2.5}$$

The physical meaning of the Patterson function can be understood by introduction and interpretation of the autocorrelation operation $\star 2$

$$P(\mathbf{r}) = \rho^{\star 2}(\mathbf{r}), \tag{2.6}$$

which turns the structure $\rho(\mathbf{r})$ directly into $P(\mathbf{r})$. The autocorrelation integral is defined in Eq. 2.7.

$$\rho^{\star 2}(\mathbf{r}) = \int \rho(\mathbf{y})\,\rho(\mathbf{r}+\mathbf{y})\,d^3y, \tag{2.7}$$

It is identified by the overlap integral between the structure, $\rho(\mathbf{y})$, and its displaced ghost. In Eq. 2.7 the vector $\mathbf{r}$ describes the amount and the direction of the displacement. In the field of SAXS it is common to normalize the Patterson function resulting in the so called *correlation function* (Debye (1949)[43], Porod (1951)[44]),

$$\gamma(\mathbf{r}) \quad = \rho^{\star 2}(\mathbf{r})/\rho^{\star 2}(0) \quad = P(\mathbf{r})/\rho^{\star 2}(0). \tag{2.8}$$

Thus $\gamma(0) = 1$ which means that the correlation between a domain and its ghost is perfect, if the displacement is zero [41].

Generally, the structure of polymers can be considered to be made from domains which can be discriminated easily from each other by a sufficient difference of their electron densities (contrast). Examples are copolymers consisting of soft and hard domains, semi-crystalline polymers (crystalline phase is denser than the amorphous regions) and porosity(voids) within a material. In this case it is advantageous [41,42] to perform an edge enhancement by applying the Laplacian operator

$$z(\mathbf{r}) = \Delta P(\mathbf{r}) \tag{2.9}$$

instead of directly studying the correlation function. This results in a 3D chord distribution function (CDF), $z(\mathbf{r})$, introduced by N. Stribeck in 2001[45,46]. The CDF is an extension of the one-dimensional chord distribution called interface distribution function (IDF), $g_1(r)$ originally proposed by Ruland[47–49] for the

study of lamellar systems. The basic idea of this technique goes back to 1965, when Méring and Tchoubar [50–53] introduced the (radial) chord length distribution (CLD), $g(r)$.

The CDF will be further explored in the next section.

Scattering Power One of the useful parameter for structure analysis is the well-known *scattering power*. It is the zero-dimensional projection of the scattered intensity [42] defined by

$$k = \{I\}_0 = \int I(\mathbf{s})\, d^3 s. \tag{2.10}$$

k is the total scattered intensity. After calibration to absolute units $I(\mathbf{s})$ turns into $I(\mathbf{s})/V$. Its scattering power is known as POROD's invariant:

$$Q = k/V \tag{2.11}$$

Q contains the non-topological structure parameters of the material's nanostructure. This means that Q depends only on the composition and contrast of the phases and not on their arrangement and shape. For multiphase systems this fact can be deduced by application of the Fourier-slice theorem and the considerations which lead to POROD's law [42]. In particular, by applying Fourier-slice theorem one obtains

$$Q = v(1-v)\left(\rho_1 - \rho_2\right)^2 + X \tag{2.12}$$

for a two-phase system. v is volume fraction of one of the phases, and $\rho_1 - \rho_2$ is the electron density contrast between the two phases. X is an unknown parameter arising from the scattering of voids, crazes, fillers or impurities within the material.

2.5.3 Interpretation of Scattering Patterns

After we have discussed the composition parameters of the SAXS of a multiphase material, we now start with the investigation of the topology. The most simple access to the arrangement of domains in the material is the discussion of long period peaks. The next level of analysis is visualization of topology.

To visualization of structure from SAXS Data, the 1D correlation function by means of a geometrical construction in several publication has been described. It is the drawback of all such methods that polydispersity and heterogeneity are not considered. if

$$\bar{L} = \bar{d}_1 + \bar{d}_2 \tag{2.13}$$

which $\bar{d}_1$ is the average layer thickness of the first of the two kinds[1] of lamellae, and $\bar{d}_2$ related to the second kind of layers, than $\bar{L}$ is called the average long period.

The easiest way to get some impression of the structure behind our scattering data without resorting to models is the computation and interpretation of a correlation function. We will mainly discuss the 1D correlation function, $\gamma_1(r_3)$, because any slice of an anisotropic correlation function is a one-dimensional correlation function. Moreover, $\gamma_1(r_3)$, is readily describing the topology of certain frequent structural entities (stacks made from layers and microfibrils). There is an advantage of the correlation function analysis as compared to "long period interpretation". The analysis of the correlation function permits to determine the average domain thicknesses (for example the thicknesses of crystalline and amorphous layers). The principal disadvantage of the correlation function is the fact that polydispersity is not properly reflected in the correlation function. This means that the statistics of domain thickness variation is very difficult to study from a correlation function. In particular, for the latter purpose it is more appropriate to carry out an analysis of the IDF or of the CDF. In complex domain topology is more clearly displayed in the CDF than in the IDF.

Chord Distribution Functions (CDFs) The multidimensional chord distribution function (CDF) is an advancement of the interface distribution function. CDF is adopted to the study of highly anisotropic materials. The advantage of the CDF is that the only required assumption is a multi-phase structure [41,42]. This assumption is correct for most of polymeric materials. Thus the structure of the material is revealed in real space without any adjusting parameters. The main prerequisites for computing the CDF are "fiber-symmetry" and completeness of the data.

[1] For instance the "amorphous", "hard", "crystalline", . . .

Step 1: Projection on the Representative Plane For the analysis of the structure we are interested in a multidimensional image in real space but not in a projection of the structural image [41,42]. In reciprocal space, however, we have to perform a projection on the representative plane (s_1, s_3) of the fiber pattern (cf. Figure 2.11), and compute

$$\{I\}_2(s_1, s_3) = \int I(s_{12}, s_3)\, ds_2. \tag{2.14}$$

This step has two main advantages [41,42]. First, it converts the related visualization of structure from a smeared (projected) to a clear one. Second, it reduces noise in the pattern. The latter is due to the averaging nature of the integral. Thus it makes it possible to decrease the exposure-time during experiment and increase the time resolution of an in-situ structure study.

Step 2: Laplacian and background correction The next step of a proposed solution[45] extracts the discrete scattering from the pattern which has already been subjected to the Laplacian in real space (cf. Eq.). For this purpose, first, an estimated density fluctuation background is subtracted. It is computed from the data points outside the inscribed circle of the image by the definition

$$I_{Fl}(s_{12}, s_3) = c_0 + c_{12}\, s_{12}^2 + c_3\, s_3^2. \tag{2.15}$$

This definition conforms to the rule that the density fluctuation background is expanded in even powers of the scattering vector [41,42]. After the subtraction, the discrete intensity is multiplied by $4\pi^2 s^2$. This multiplication is equivalent to the Laplacian[2] edge-enhancement operator, as is evidenced by double application of the derivative theorem.

Now a correction for the non-ideal character of the multiphase topology must be performed. In the classical analysis this is a manual evaluation step which results in the subtraction of a slowly varying background [42,54,55]. Here the background determination is replaced by the result of a low-pass filter, applied to the scattering image at the present state of evaluation [56].

[2] Here the negative sign is missing – but we are not interested to work with negative intensities and will take care for the sign later.

Step 3: Fourier transform After background subtraction, an interference function $G_2(s_1, s_3)$ is obtained. Its 2D Fourier transform,

$$z(r_1, r_3) = -\mathscr{F}_2\left(G_2(s_1, s_3)\right), \tag{2.16}$$

is the sought after multidimensional chord distribution function. Because of fiber symmetry, the plane (r_1, r_3) is representative for the 3D structure [41,42], hence it is permitted to identify $r_1 \to r_{12}$. Thus $z(r_{12}, r_3)$ has been computed.

Interface distribution functions (IDFs) For a layer-stack material or other semi-crystalline polymers the IDF presents clear hints on the shape of the layer thickness distributions, the range of order, and the complexity of the stacking topology. Based on these findings inappropriate models for the arrangement of the layers can be excluded. Finally the remaining suitable models can be formulated and tested by trying to fit the experimental data.

As pointed out by STRIBECK [57,58] $g_1(x)$ is, as well, suitable for the study of oriented microfibrillar structures and, generally, for the study of 1D slices in deliberately chosen directions of the correlation function. This follows from the Fourier- slice theorem and its impact on structure determination in anisotropic materials, as discussed in a fundamental paper by BONART[59].

In practical application to common isotropic polymer materials the IDF frequently exhibits very broad distributions of domain thicknesses. At the same time fits of the IDF curve to the well-known models for the arrangement of domains are not satisfactory, indicating that the existing nanostructure is more complex. In this case one may either fit a more complex model[3] on the expense of significance, or one may switch to the study of anisotropic materials and display their nanostructure in a multidimensional representation, the multidimensional CDF.

The interface distribution function

$$g_1(x) = -\left(\frac{d\rho_1(x)}{dx}\right)^{\star 2} = -k\gamma_1''(x) \tag{2.17}$$

is proportional to the 2*nd* derivative of the related 1D correlation function,

[3] A more complex model can be constructed from two components or a special sequence of (thick and thin) layers.

$\gamma_1(r)$. The $g_1(x)$ is computed from any 1D scattering intensity, e.g. $I_1(s_3)$

$$g_1(x) = -\mathscr{F}_1\left(4\pi s_3^2 I_1(s_3) - \lim_{s_3\to\infty} 4\pi s_3^2 I_1(s_3)\right) \tag{2.18}$$

$$= -\mathscr{F}_1(G_1(s_3)) \tag{2.19}$$

by 1D Fourier transform. It is permitted to replace $I_1(s_3)$ by any 1D projection $I_1(s_i)$ of a deliberate scattering pattern. The function which is subjected to the Fourier transform is identified as a 1D interference function, $G_1(s_3)$.

The $g_1(x)$ is a series of thickness distributions, $h_i(x)$. Thus, in the special case of a layer stack morphology, $g_1(x)$ is a series of thickness distributions (cf. Fig.2.12). The series starts from the thickness distributions of "amorphous" and

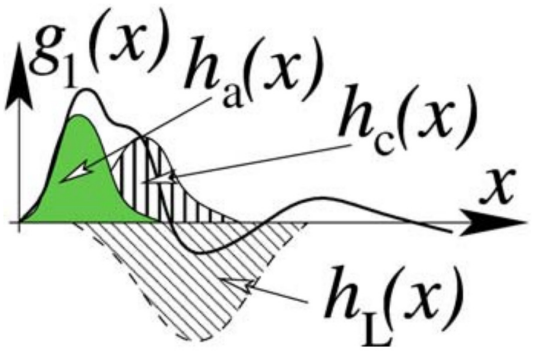

Figure 2.12: The features of a primitive interface distribution function, $g_1(x)$. The IDF is built from domain thickness distributions, $h_a(x)$ and $h_c(x)$, followed by the distribution of long periods, $h_L(x)$, and higher multi-thickness distributions[42]

"crystalline" layers, $h_a(x)$ and $h_c(x)$, respectively. It is continued by the distributions of aggregates of adjacent layers, the first being an aggregate of one amorphous and one crystalline layer. The corresponding di-thickness distribution, $h_L(x) = h_{ac}(x) + h_{ca}(x) = 2h_{ac}(x)$ shows up with negative sign and represents the long periods. Thereafter we have the tri-thickness distributions $h_{aca}(x)$,$h_{cac}(x)$ and the following multi-thickness distributions.

In an anisotropic material we select the fiber axis, r_3 , project the intensity on this direction and compute an IDF. Then the meaning of the thickness distributions is

quite similar as in the aforementioned example. Let us identify the first thickness distribution, $h_h(r_3)$, by a distribution of hard-domain thicknesses. Then the next thickness distribution, $h_s(r_3)$, is the thickness distribution of the soft material in between, and the long period distribution is $h_L(r3) = h_{hs}(r_3) + h_{sr}(r_3) = 2h_{hs}(r_3)$.

From the transformed experimental data we can determine, whether the principal thickness distributions are symmetrical or asymmetrical, whether they should be modeled by Gaussian, gamma distributions, truncated exponentials, or other analytical functions. Finally only a model that describes the arrangement of domains is missing i.e., how the higher thickness distributions are computed from two principal thickness distributions. Experimental data are fitted by means of such models. Unsuitable models are sorted out by insufficient quality of the fit.

Relation between a CDF and IDFs Every radial, 1D slice through the center of a CDF

$$\lceil z \rceil_1 \left(r_{\psi,\varphi} \right) \quad = \quad g_1 \left(r_{\psi,\varphi} \right) \tag{2.20}$$

is an IDF [42]. In the above equation, the slicing direction is indicated by a polar and an azimuthal angle, ψ and φ, respectively. Of especial practical interest for the study of materials with fiber symmetry is the cut of the CDF along the meridian (fiber axis),

$$\lceil z \rceil_1 (r_3) = z(0, r_3) = g_1 (r_3) . \tag{2.21}$$

$z(0, r_3)$ describes the longitudinal structure of the material. In analogy the transverse structure is described by the slice

$$\lceil z \rceil_2 (r_{12}) = z(0, r_{12}) = g_2 (r_{12}) \tag{2.22}$$

of the CDF[60].

Chapter III

Experimental

In order to investigate the influence of TPU hard segments on physical properties, three groups of TPUs are monitored by small-angle X-ray scattering (SAXS).

Group1: Effect of hard segment content on morphological transition during uniaxial deformation.

Group2: Effect of hard segment components on morphological transition during uniaxial deformation.

Group3: Effect of nucleating agents on thermal behavior.

3.1 Materials and samples

In all groups, the raw materials have been produced by BASF and all TPUs have been produced by BASF Polyurethanes Ltd in Lemförde, Germany using a band casting process[61]. In this continuous one-shot process the raw materials are fed through a mixing head on a conveyor belt, where the material reacts and solidifies. The casts have been ground to chips and subsequently injection molded to obtain uniform sheets (thickness: $2mm$) for testing. Prior to measurement the sheets have been annealed at $100°C$ for $20h$. For all samples the chemical topology of the chains is based on the well-known polyaddition process of polyurethanes. The result is a random copolymer.

The material characteristics is discussed in the following.

3.1.1 Group1: Varying hard segment content

6 different thermoplastic polyurethanes (TPU) with different hard segment content have been prepared.

All samples are made from the same basic components 4,4'-methylene diphenyl diisocyanate (MDI), 1,4-butane diol (BD) and polytetrahydrofuran (PTHF). The materials characteristics are presented in Table 3.1.

Table 3.1: The first group of materials characterization.

Material label	HSC [wt.-%]	hardness [shore D]	special feature
B56	56	65	-
B43	43	49	-
B30	30	39	-
B30a	30	40	without additives
P30A	30	40	more allophanate
P32O	32	38	produced opaque

Material B30a contains no additives; all other materials contain anti-oxidation and anti-UV degradation stabilizers in a ppm concentration range. P30A has an increased content of allophanates. For P32O the reaction has been carried out at reduced temperature which results in the formation of on optically opaque material. As usual, the hard segment content HSC = MDI+BD is calculated from the contents of 4,4'-methylene diphenyl diisocyanate (MDI) and 1,4-butanediol (BD) according to

$$\mathrm{HSC} = \frac{\mathrm{n}_{chain\,extender}\left(\mathrm{M}_{chain\,extender} + \mathrm{M}_{diisocyanate}\right)}{\mathrm{m}_{total}} \tag{3.1}$$

whilst neglecting the second terminal diisocyanate. Four TPUs have been produced at a hard segment content of nominally 30 wt.-%.

Most TPUs have been made with a slight molar excess of hydroxyl groups, but P30A has been produced with a slight molar excess of isocyanate. Doing so results in the formation of a higher amount of allophanate bonds. These allophanates, in terms, introduce a low amount of branching of the otherwise linear polymer chains.

We have carried out wide-angle X-ray scattering (WAXS) scans of the isotropic materials. Crystallites cannot be detected. All samples show only a broad amorphous halo with a maximum at $2\theta \approx 20°$.

3.1.2 *Group2: Varying hard segment components*

In this group of materials, we study 5 thermoplastic polyurethanes (TPUs). All materials contain the same macrodiol as the soft segment (polytetrahydrofuran PTHF, a trade mark of BASF). Different are the components which form the hard segments, namely the diisocyanates (DIs) and the diols which act as chain-extenders (CEs). Composition and hardness are presented in Table 3.2.

Table 3.2: The second group of materials characterization.

Material label	diisocyanate (DI)	chain extender (CE)	HSC [wt.-%]	hardness [shore D]
M3	methylene diphenyl diisocyanate (MDI)	1,3-propanediol (PDO)	43	51
M6	methylene diphenyl diisocyanate (MDI)	1,6-hexanediol (HDO)	43	49
M4	methylene diphenyl diisocyanate (MDI)	1,4-butanediol (BD)	43	49
HM4	4,4'-diisocyanato dicyclohexylmethane (HMDI)	1,4-butanediol (BD)	50	56
H4	hexamethylene diisocyanate (HDI)	1,4-butanediol (BD)	46	48

The hard segment content is, again, calculated according to equation 3.1. Antioxidant and UV stabilizers (1 ppm) are added into the raw materials to protect the chemical stability. After molding plates of 2 mm thickness, the primary sheets have been annealed at $100°C$ for $20h$. The hardness has been measured thereafter.

Wide-angle X-ray scattering (WAXS) has been carried out in order to check the crystallinity of the polyurethanes. Figure 3.1 shows the results. Only sample H4 shows strong crystalline reflections. In the materials H4 and M6 weak crystalline reflections appear to be indicated.

3.1.3 *Group3: Varying nucleating agents*

In this group of materials the effect of nucleating agent is discussed. For this purpose we study two different types of thermoplastic polyurethanes (TPUs). The materials have different soft segments. The soft segment of the first mate-

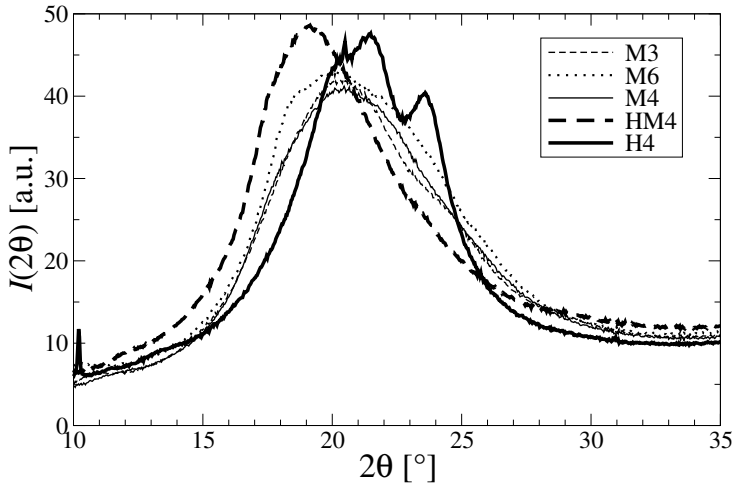

Figure 3.1: Wide-angle X-ray scattering of the isotropic original TPU materials

rial is made from a polyether (“ET”). The soft segment of the second material is made from a polyester (“ES”). The components which form the hard segments are identical. The diisocyanate is methylene diphenyl diisocyanate (MDI), the chain extender is 1,4-butanediol (BD). Each type is studied in three variant materials, namely the original (blank) material and two materials doped with two different nucleating agents (N1, N2). The sample designations are presented in Table 3.3. They are derived from the acronym of the soft segment and a number indicative

Table 3.3: Sample designations of 6 TPU materials as a function of the soft segment (ether or ester) and the presence of nucleating agents (agent 1 or 2).

	ether	ester
Blank	ET	ES
N1	ET1	ES1
N2	ET2	ES2

of a nucleating agent. All samples have been annealed before the measurements at 100°C for 20 h.

3.2 Sample geometry

To determine the tensile properties a dumbbell "Dog-Bone" test bar is cut from a test sheet. The geometry of the tensile bars is according to DIN 53504using the S_3. This standard is used for tensile tests on rubber and elastomer samples in very small size. The geometry of the tensile bars is shown in fig 3.2.

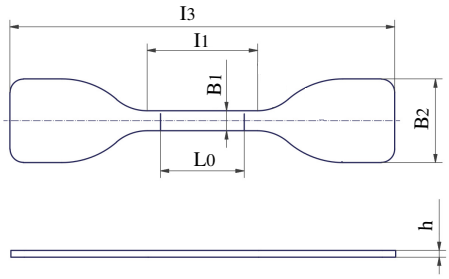

I3 (overall length) = 35 mm
I1 (length of narrow paralle) = 12±0.5 mm
B1 (width of narrow portion) = 2±0.05 mm
L0 (gauge length) = 10 mm
B2 (width at ends) = 6±0.5 mm
h (thickness) = 2±0.2 mm

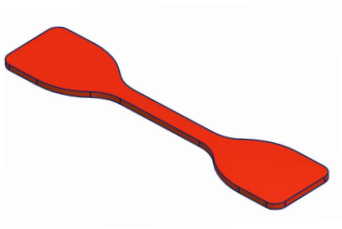

Figure 3.2: specimen dimensions for tensile test bar for rubbers and elastomer samples in very small size.

3.3 Tensile testing

Tests are run in a self-made[62] machine. A grid of fiducial marks is printed[63] on the bars. The clamping distance is 21 mm. Signals from the transducer are recorded during the experiment. The sample is monitored by a TV-camera. Video frames are grabbed every 60 s and are stored together with the experimental data. The machine is operated at a cross-head speed of 1 mm/min. Using the fiducial marks, the local macroscopic strain $\varepsilon = (\ell - \ell_0)/\ell_0$ at the position of X-radiation is computed from the initial distance, ℓ_0, of two fiducial marks and the respective actual distance, ℓ. Processing all the video frames yields the curve $\varepsilon(t)$ as a function of the elapsed time. It is very well approximated by a quadratic polynomial. The local strain rate $\dot{\varepsilon} \approx 1.3 \times 10^{-3}\,\mathrm{s}^{-1}$ is kept low in order to be able to monitor the straining process by the slow detector.

3.4 Thermal treatment

In this expriment the samples have been loaded into the custom-built furnace available at the beamline and heated up to 240 °C under electronic control. Thereafter they have been cooled by air without control ("ballistic cooling"). The air flow has been adjusted so that there was a cooling rate of about 20 K/min in the critical temperature range. Figure 3.3 displays the temperature program which has been identical for all experiments.

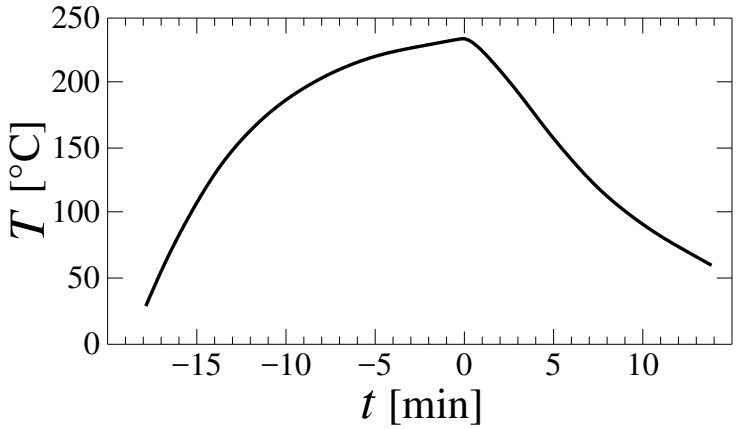

Figure 3.3: Temperature profile $T(t)$ measured in the melting/solidification experiments of TPU materials with different nucleating agents

3.5 Synchrotron experiments

Beam line setup Small-angle X-ray scattering (SAXS) is carried out in the synchrotron beamline 7T-MPW-SAXS at BESSY II, Berlin operated in top-up mode with a ring current of 300 mA. Then the 7-Tesla multipole-wiggler delivers a photon flux of $6\times10^{12}\mathrm{s}^{-1}$. The downstream optics is optimized for setups with a sample-detector distance in the typical SAXS range of 3 m. The chosen primary-beam cross-section is 1 mm × 0.4 mm (width × height), the sample-detector distance is 2854 mm as determined by calibration with Ag-Behenate (long period $d_{001} = 5.8380$ nm) and the photon energy of 8310 eV, equivalent to the wavelength $\lambda = 0.1492$ nm. A filter package in the primary beam is engaged in order to limit the count rate in the detector. The intensity ratios of different filter set-

tings are measured for later compensation. The detector is a 2D gas detector (multi-wire proportional counter) built by JJ X-ray, Kgs. Lyngby, Denmark. It has 1024 × 1024 pixels of 207 µm × 207 µm. Scattering patterns are recorded every 240 s with an exposure of 140 s. The patterns $I(\mathbf{s}) = I(s_{12}, s_3)$ cover the region $-0.24\,\mathrm{nm}^{-1} \leq s_{12}, s_3 \leq 0.24\,\mathrm{nm}^{-1}$. $\mathbf{s} = (s_{12}, s_3)$ is the scattering vector with its modulus defined by $|\mathbf{s}| = s = (2/\lambda)\sin\theta$. 2θ is the scattering angle. The smallest s-values recorded close to the central beam stop is $s_{min} = 0.0125$ nm^{-1}. The remnant small blind area in the center is filled by extrapolation. Before any processing the patterns are corrected for the uneven detector sensitivity which has been measured using a radioactive Ni-target. The scattering patterns are normalized and background corrected[42]. This means intensity normalization for constant primary beam flux, zero absorption, zero filter, and constant irradiated volume V_0. Because the flat samples are wider than the primary beam, the correction is done assuming $V(t)/V_0 = (1+\varepsilon(t))^{-0.5}$ with t being the elapsed time. The equation assumes constant sample volume and constant beam-footprint on the sample. Absorption factors $\exp(-\mu t_{s0})$ of the unstrained samples are determined by measuring the primary beam flux in front of the detector with and without sample, respectively. From the result the linear absorption factor, μ, is computed using the known sample thickness. Finally the actual absorption factor $\exp(-\mu t_s(t))$ is assessed using $t_s(t) = t_{s0}(1+\varepsilon(t))^{-0.5}$. The strain which is associated to each scattering pattern is related to the time $t + t_e/2$ with t being the elapsed time at the start of the exposure, and t_e the total exposure of the pattern. After these steps the resulting scattering patterns are still not in absolute units, but their intensities can be compared relatively to each other.

SSRL Synchrotron In third study the mall-angle X-ray scattering (SAXS) is carried out at the Stanford Synchrotron Radiation Lightsource (SSRL), beamline B1-5 and using a MAR detector (new brand: Rayonix-165) with 2048x2048 pixels. The cycle time was 30 s (exposure: 10 s). The sample-detector distance (2711 mm) has been determined by an Ag-Behenate standard. The X-ray wavelength has been $\lambda = 0.15$ nm. During the heating patterns have been recorded in the temperature range between 170 – 240°C. During the ballistic cooling patterns have been taken down to a temperature of 50°C. Here the cycle time determines the temperature resolution of ca. 10 K.

3.5.1 Evaluation of Scattering data

Firstly, it is important to highlight that PV-WAVE is a comprehensive software environment that integrates state-of-the-art graphical and numerical analysis techniques into a system that is easy to use, easy to extend, easy to apply and easy to learn. PV-WAVE provides the tools we need to find solutions to build applications for complex technical problems[64]. It is software which provides many kinds of visual data analyses through 2D and 3D plotting.

PV-WAVE provides routines for plotting data in a variety of ways. These routines allow general X versus Y plots, contouring, mesh surface plots, perspective plotting and data clipping in an extremely flexible matter without requiring complicated programs. Such plotting allows the easier visualization of data during the analysis. PV-WAVE was the programming language used, in order to characterize the SAXS patterns.

Evaluation of the SAXS patterns consists of three main stages. Stage I includes pre-evaluation of raw data. In stage II the fiber diagrams, CDFs and scattering power are computed. Stage III includes peak-analysis of the CDFs (or SAXS patterns) and extracting the desired nanostructural parameters.

Pre-evaluation of SAXS data All steps of data-evaluation are discussed in a text book [42]. Here the main concepts are briefly reviewed.

Normalization Scattering patterns and the background are divided by the actual incident flux measured by the first ionization chamber, and also by the actual exposure time. The former is necessary due to the decay of the incident beam flux after each injection at a synchrotron source.

Valid Area Masking. The area on the detector, in which valid data have been recorded is determined. Then all invalid points are removed. In a 2D scattering pattern the invalid points includes the beam stop, its holder, the edge of the vacuum tube, and the edge of the detector. The result is a mask image that can be used for the processing of all data recorded with the same beamline alignment. Every scattering pattern is multiplied by the mask. The results are images in which all invalid pixels are set to zero intensity.

A mask is usually a combination of several masks each removing some of the invalid points. For instance, for SAXS patterns recorded at the beam-line one needs to encircle the area of valid points (mask1), take out the beam stop (mask2) and the holder of the beam stop (mask3). The final mask is the multiplication of these three masks. The steps are depicted in Figure 3.4[60].

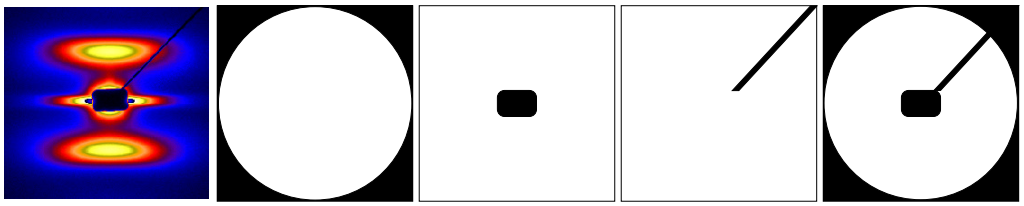

Figure 3.4: steps of making the mask. The final mask is a pattern of 0 and 1 values. Zeros and ones define the invalid and valid points, respectively[60]

Absorption and Background Correction. The amount of matter irradiated by the X-ray varies during an in-situ SAXS measurement. Moreover, the matter causes both scattering and absorption of the X-ray. Therefore, it is necessary to correct the absorption effects. In practice absorption correction is done based on two flux measurements by means of ionization chambers, one placed before (I_1), and the other behind (I_2) the sample. If $I_{1,0}$ is the reading of the first ionization chamber during a measurement of parasitic background and $I_{1,s}$ is the reading during sample measurement with the analogous nomenclature for the reading of the second ionization chamber then

$$\exp(-\mu t) \approx \frac{I_{2,s} I_{1,0}}{I_{2,0} I_{1,s}} \tag{3.2}$$

is approximately valid. μ is linear absorption coefficient and t is sample thickness. The measurement of the incident flux I_1 is only necessary due to the variation of the flux of the synchrotron radiation sources.

Alignment The center of gravity of the primary beam is moved into the center of the image matrix. In addition, in the case of anisotropic scattering patterns,

the meridian is aligned in vertical direction. Thus the parameter set of the operation is made from the position of the true center, (x_c, y_c), on the raw image measured in raw pixel coordinates and from an angle of image rotation, φ . If these parameters are known and the sample does not rotate during the experiment, all frames of the experiment can be centered and aligned using the same set. This is usually true during a tensile test.

Harmony If there is uniaxial symmetry and the fiber axis is in the detector plane, the scattering pattern can be divided into four quadrants. Each quadrant carries identical information. This means that there is some harmony in the scattering pattern. Thus the missing data of one quadrant (e.g. the shadow of the beam-stop holder) can be reconstructed using the data of other quadrants. The remaining central blind hole is filled applying a stiff parabolic extrapolation[65]. In this step a series of patterns are aligned and corrected by:

```
wave> allraw2harm, 'series_name'
```

The result is a series of harmonized fiber-diagrams.

Computing CDFs The harmonized fiber-diagram pattern is projected on the representative fiber-plane (s_1, s_3). In PV-WAVE® it is done by calling *allharm2cdf.pro*:

```
wave> allharm2cdf, 'series_name'
```

Multiplication by s^2 applies the real-space Laplacian. Here s is the modulus of the scattering vector, $\mathbf{s} = (s_{12}, s_3)$, defined by $s = |\mathbf{s}| = (2/\lambda)\sin\theta$. The density fluctuation background determined by low-pass filtering is eliminated by subtraction. The resulting interference function, $G(s_{12}, s_3)$, describes the ideal multiphase system. Its 2D Fourier transform is the chord distribution function (CDF) [45], $z(r_{12}, r_3)$.

The main steps from the recorded pattern toward the CDFs are schematically depicted in Figure 3.5.

It shows a representative recorded SAXS pattern, the corrected fiber diagram $I(s_{12}, s_3)$, absolute values of the CDF $|z(r_{12}, r_3)|$ and a slice of the CDF along the meridian, $z(0, r_3)$. Plotting the $z(0, r_3)$ curve is the easiest way of analyzing the structure along the principal axis of the material (straining direction). The

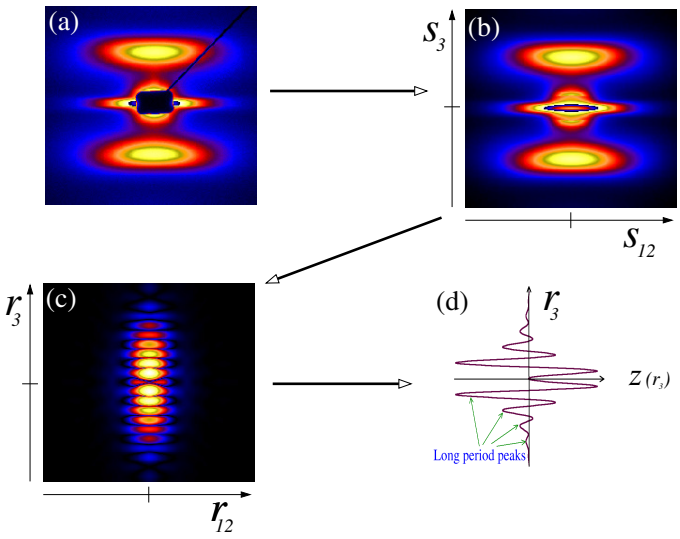

Figure 3.5: Representative X-ray scattering data of oriented polymers (e.g. MFC precursors): (**a**) the recorded SAXS pattern. The blind area arises from the shadow of the primary beam-stop (**b**) the corrected fiber diagram $I(s_{12}, s_3)$, (**c**) absolute value of the CDF $|z(r_{12}, r_3)|$, and (d) a one-dimensional slice of the CDF along the meridian $z(0, r_3)$ showing the negative long-period peaks and the positive peaks (above the r_3-axis). Image intensities on logarithmic scale. Displayed regions: $-0.1\,\mathrm{nm}^{-1} < s_{12}, s_3 < 0.1\,\mathrm{nm}^{-1}$, $-100\,\mathrm{nm} < r_{12}, r_3 < 100\,\mathrm{nm}$. The s_3- and r_3-axes match the stretching direction of the sample[60].

negative peaks arise from the correlation between domain surfaces that define the long-period and multiples thereof. The peaks on the positive side measure thicknesses of domains in r_3-direction.

Computing the scattering power From $G(s_{12}, s_3)$ the scattering intensity $I_{id}(s_{12}, s_3)$ of the ideal multiphase system can be reconstructed. From this pattern the scattering power is computed. Q is already normalized with respect to the irradiated volume, because of the respective normalization of the measured intensity. The predominant contribution [42, 66–69] to the invariant

$$Q = v(1-v)(\rho_1 - \rho_2)^2 + X \tag{3.3}$$

originates from the two-phase nanostructure of the studied semi-crystalline polymers with v being the volume crystallinity, and $\rho_1 - \rho_2$ the contrast between the

electron densities of the two phase. An additional quantity X may originate from big embedded particles, e.g. voids or crazes.

In PV-WAVE® it is done by calling *sf_anscatpower.pro*:

```
wave> sf_anascatpower, 'series_name'
```

Computing IDFs Bonart's longitudinal scattering[59] is obtained by not integrating over the whole reciprocal space, but only over planes normal to the fiber axis yielding the curve

$$\{I\}_1(s_3)/V = 2\pi \int_0^\infty s_{12} I(s_{12}, s_3)/V \, ds_{12}, \tag{3.4}$$

which is a function of the straining direction s_3 . This is a projection onto a 1D subspace as indicated by subscripting to the pair of braces.

From such projections interface distribution functions[42,47,57] (IDF) $g_1(r_3)$ are computed for further analysis. By fitting the IDF to an appropriate one-dimensional two-phase model morphological parameters are determined.

Technically, we subtract a constant fluctuation background[54,70,71] I_{Fl} from the measured curve and multiply by $4\pi^2 s_3^2$ to apply the second derivative in reciprocal space. The result is an intermediate interference function

$$G_{1,i}(s_3) = (\{I\}_1(s_3)/V - I_{Fl})\, 4\pi^2 s_3^2.$$

We apply a guessed I_{Fl} (the same for all patterns and materials) that is refined afterwards, when the final background is constructed by application of a narrow low-pass frequency filter to $G_{1,i}(s_3)$, as is described elsewhere[42,45]. Thus the interference function $G_1(s_3)$ is obtained. Its one-dimensional Fourier transform is the longitudinal IDF $g_1(r_3)$.

The $g_1(r)$ curves show a very strong domain peak and faint short-range correlations. Thus a model should work that represents these two components, namely first uncorrelated hard domains and, second, hard domains which are correlated to one neighbor.

In this study the IDF is evaluated from harmonized SAXS patterns. In the first step the "vertical projection" (VP) according to Eq.(3.4) is extracted and saved. Our PV-WAVE®procedures are invoked by :

```
wave>a=sf_xdread ('file name')
```

```
wave>curve=sf_vp (a)
wave>sf_cwrite, curve , 'file name.dat'
```

In second step to evaluate the IDF data, the extracted projection data are processed by a PASCAL program, TOPAS written by Stribeck. TOPAS is a computer program for the data evaluation of small– angle X–ray scattering (SAXS) curves. It runs under MS–DOS. This program evaluates CURVES. The curves come from a SOURCE. They may be put into a DESTINATION. To hold the curves during evaluation, the program offers two OPERAND ARRAYS (OP1, OP2). Common sources / destinations are binary curve files, which can contain many curves in one file (.KUR files). But ASCII files which contain one single curve can be read/written as well for convenience. This is a rather complex program which needs a few resources, in order to fulfill all its tasks.

The steps are as follows:

```
#get ;the scattering curve
#mul,1,1,2 ;multiply by Porod-Power (here: 2)
#stretch ;prepare for spatial frequency filtering
#fil. ;extract interference function by filtering
#low.,25 ;smooth it by low pass filter
#ops,< ;accept smooth curve
#phys.,300,1 ;compute IDF running from 0 to 300 with step size 1.
#mul,1E5,2 ;"normalize" the IDF
#put„2 ;save the IDF in destination file
#pasc.,out,2 ;save the IDF in the file out.dat in ASCII code.
```

In the present work curves like IDFs or projections are presented by the 2D plotting program XMGRACE.

Chapter IV

Results

4.1 Effect of hard segment content on morphological transition during uniaxial deformation

In the first group of materials machine-cast TPUs are strained and monitored by SAXS. They are prepared from 4,4'-methylene diphenyl diisocyanate (MDI), 1,4-butane-diol (BD) and polytetrahydrofuran (PTHF). Upon stretching hard domains are destroyed. Most stable are the domains of materials with a hard-domain content (HSC) of 30%. Domain stability decreases with increasing HSC and crosslinking. Most materials show stability up to a strain 0.6. At higher strain the apparent long period decreases for the materials with HSC=30%. Correlated hard domains, the "strain probes" relax as others are destroyed. The fraction of relaxing probes and their ultimate relaxation decrease with increasing HSC.

Chord distribution functions (CDF) computed from the SAXS exhibit the same sequence of static long-period bands. The band positions form a Fibonacci series, related to the underlying polyaddition process. This indicates a nearly quasicrystalline arrangement of stringed hard domains, identified as the strain probes of the discrete SAXS. At strains < 0.6 the probes experience half of the macroscopic strain, which reflects hard-domain rigidity.

4.1.1 Obvious features of SAXS patterns and CDFs

Figure 4.1 presents recorded scattering patterns $I(s_{12}, s_3)$ and CDFs $z(r_{12}, r_3)$ computed thereof. In fact, only central cutouts are displayed and only the long-period face $-z(r_{12}, r_3) > 0$ of the CDFs is shown. CDFs visualize the local structure in the neighborhood of a domain: Each peak shows, in which direction and distance neighbor domains are found. The integral of a peak is a measure of the population density. It appears worth to repeat that scattering cannot detect the

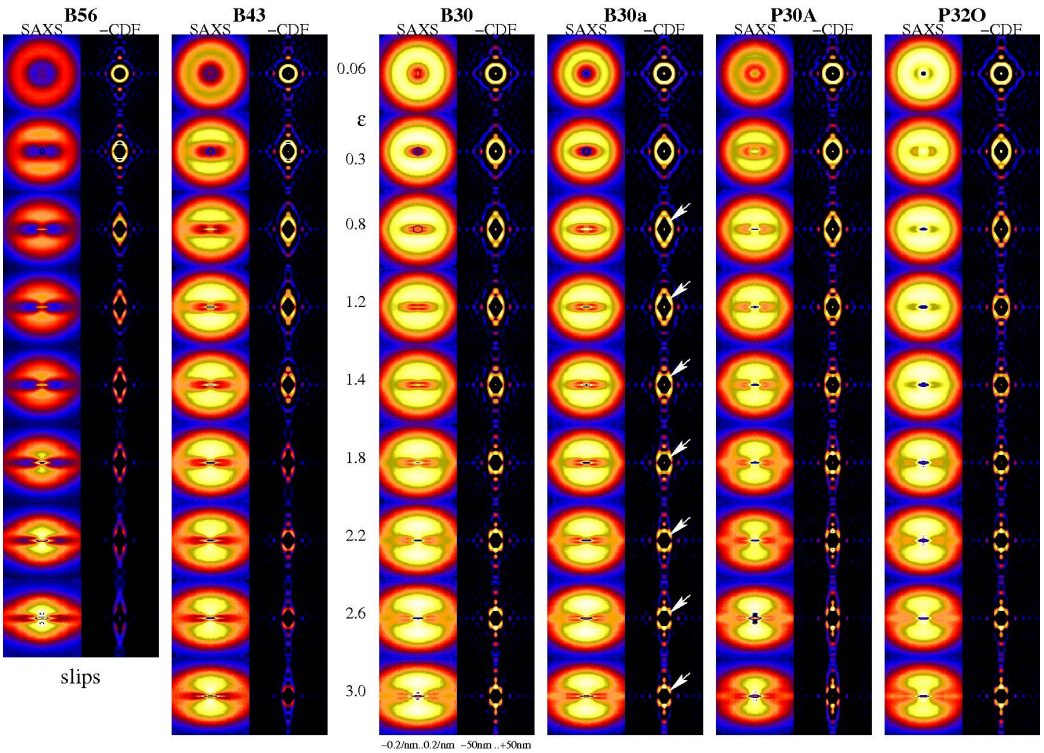

Figure 4.1: Selected SAXS data of the materials collected during continuous straining experiments. The strain ε is labeled in the text column. In each block on the left the central part of the scattering intensity ("SAXS") is presented. This is $I(s_{12},s_3)$, $-0.2\,\mathrm{nm}^{-1} \leq s_{12},s_3 \leq 0.2\,\mathrm{nm}^{-1}$. The right pattern in each block presents the long-period peaks in the chord distribution function ("-CDF"), $-z(r_{12},r_3)$, $-50\,\mathrm{nm} \leq r_{12},r_3 \leq 50$ nm. The logarithmic pseudo-color intensity scales are identical within each material. The straining direction (s_3, r_3 resp.) is vertical

presence of a poorly arranged co-continuous morphology. This is a consequence of the mathematical relation (notably: an autocorrelation) between structure and scattering pattern. Thus, domains that bend away from the normal plane to the straining direction appear cut-off in lateral direction in the SAXS data.

For each experiment a block of images is presented. The upper patterns in a block show the data of the unstrained isotropic materials. They are followed below by selected patterns from the tensile test. A central text column indicates the strain ε. To the left of the text column are placed the materials with higher HSC.

To the right all materials have a HSC $\approx 30\,\mathrm{wt.\text{-}\%}$. They differ by process-

ing conditions and additive. Figure 4.1 shows that here the courses of scattering patterns and CDFs as a function of strain are very similar. Even the intensities of B30, B30a and P30A are similar and the same logarithmic intensity scale has been chosen. Omitting of additives (B30a) or a higher fraction of allophanates (P30A) does not cause fundamental changes.

A significant morphological difference shows up in the CDFs of P30A. Left and right from the central vertical line (meridian) the strongest off-meridional peaks (arrows in Figure 4.1) of all materials are found. They exhibit considerable 3D correlation among hard domains that may be related to chemical crosslinking by the high amount of allophanate present in this material.

As a function of HSC (cf. data left of the text column in Figure 4.1) the nanostructure and its evolution varies considerably. With increasing ε and HSC the SAXS peaks clearly move closer to the center. The features of the CDFs are different, as well. The corresponding discussion is devoted to a separate subsection.

4.1.2 SAXS pattern analysis

Unstrained Materials For the virgin samples a common method of long-period determination has been employed. The values reported in Table 4.1 are deter-

Table 4.1: Morphology of neat materials. Long periods L and scattering power Q as determined from the SAXS patterns

sample	L [nm]	Q [a.u.]
B56	7.3	0.78
B43	8.0	2.48
B30	9.1	2.50
B30a	9.6	2.50
P30A	9.4	3.14
P32O	9.4	0.65

mined from the position $s_L = 1/L$ of the peak maximum in the curve $s^2 I(s)$. The peaks are very wide, and thus the determined values may be far from the number-average long period. The scattering power Q is low for two of the materials. The low Q of B56 may be explained by a poor phase separation or by inhomogeneity of the material. There may also be regions of almost homogeneous electron den-

sity that are too big to cause scattering in the **s**-range of the setup. For P32O the last explanation is rather probable, because the sample scatters light and is opaque. The other "B"-materials share very similar Q, and P30A is even somewhat higher.

In the tensile test: Peak position and invariant During straining the SAXS pattern turns from an isotropic pattern into a fiber pattern and the SAXS peak moves. As a function of ε simply tracking the position $s_{3,L}$ for which $I(0, s_{3,L})$ is the maximum yields rather noisy data for $\varepsilon > 0.8$. For $\varepsilon < 0.6$ most of the samples (except P32O) exhibit affine peak movement for the apparent nanoscopic strain $\varepsilon_{na}(\varepsilon) \approx \varepsilon$. $\varepsilon_{na}(\varepsilon) = L_a(\varepsilon)/L_a(0) - 1$ has been determined from the apparent SAXS long period $L_a = 1/s_{3,L}$. Because of the complex superposition of orientation and different contributions to the long period L_a we do not draw conclusions from the found relation.

The relative changes of the scattering power $Q(\varepsilon)$ are displayed in Figure 4.2. With all materials a decrease is observed. This decrease indicates destruction of

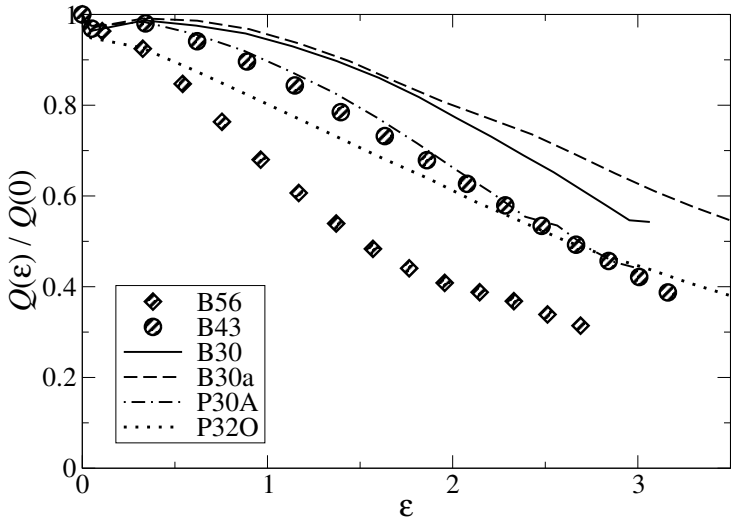

Figure 4.2: Relative variation of the invariant Q during the tensile test as a function of ε

hard domains during the test. The most stable material is B30a, the material without additives, but the corresponding material with additives, B30, is very similar. The material with high amount of allophanates (P30A) is as stable as the material with slightly increased HSC (B43). Increased chemical crosslinking and

increased physical crosslinking appear to result in a similar destabilizing effect on the morphology.

The already discussed materials exhibit a stability plateau for small ε. This is different with the slowly synthesized material P32O and the material with high HSC (B56). Both show a linear decrease for $0 < \varepsilon < 1.5$.

Assuming that the soft-domain density is not decreasing in the test, $v_h(\varepsilon)$ can be determined essentially from the curves in Figure 4.2. If, moreover, $v_h < 0.3$ then already $Q(\varepsilon)/Q(0) \approx v_h(\varepsilon)/v_h(0) = v_{hr}$ approximates the fraction of remnant hard domains quite well. The lowest v_{hr} encountered in our tensile tests is found with B56. With $v_{hr} = 0.31$ it has lost 70% of its hard domains without failing macroscopically. Even higher losses without macroscopic failure have been found in a parallel study[72].

SAXS longitudinal structure The 1D longitudinal projection $\{I\}_1(s_3)/V$ is a curve that contains information on the nanostructure in straining direction[42,57]. Bonart[59] has called this 1D scattering curve the "longitudinal structure". It describes the sequence of chord lengths (thicknesses) of hard domains and soft-phase gaps in the direction of strain. Moreover, the area below the curve, $\int \{I\}_1(s_3)/V\, ds_3 = Q$, is the invariant that has already been discussed.

Figure 4.3 presents the 4 different types of evolutions that have been found. Figure 4.3a displays the evolution for B56, the material with the highest HSC. With increasing strain the peak maximum is moving left (prograde movement) indicating a continuous increase of the average long period. Significant numbers of a respective nanoscopic strain cannot be given. The reason is the unspecific maximum position in the projected intensities for $\varepsilon = 0$. It would be required as the reference. The decay of the area under the curves has already been discussed.

For B43 (Figure 4.3b) there is also the normal prograde movement of the peak. With B30 (Figure 4.3c) an increase of the long period is only observed for low ε as long as the curve integral is stable (no hard-domain destruction). When the destruction has set in ($\varepsilon = 1$), the peak has already started to move right. Thus relaxation of the strain probes goes along with hard domain destruction. This direct observation supports the sacrifice-and-relief mechanism that our group has suggested recently[72,73]. The materials B30a and P30A exhibit a nanostructure evolution that is almost identical to that of B30. Figure 4.3d presents the longitu-

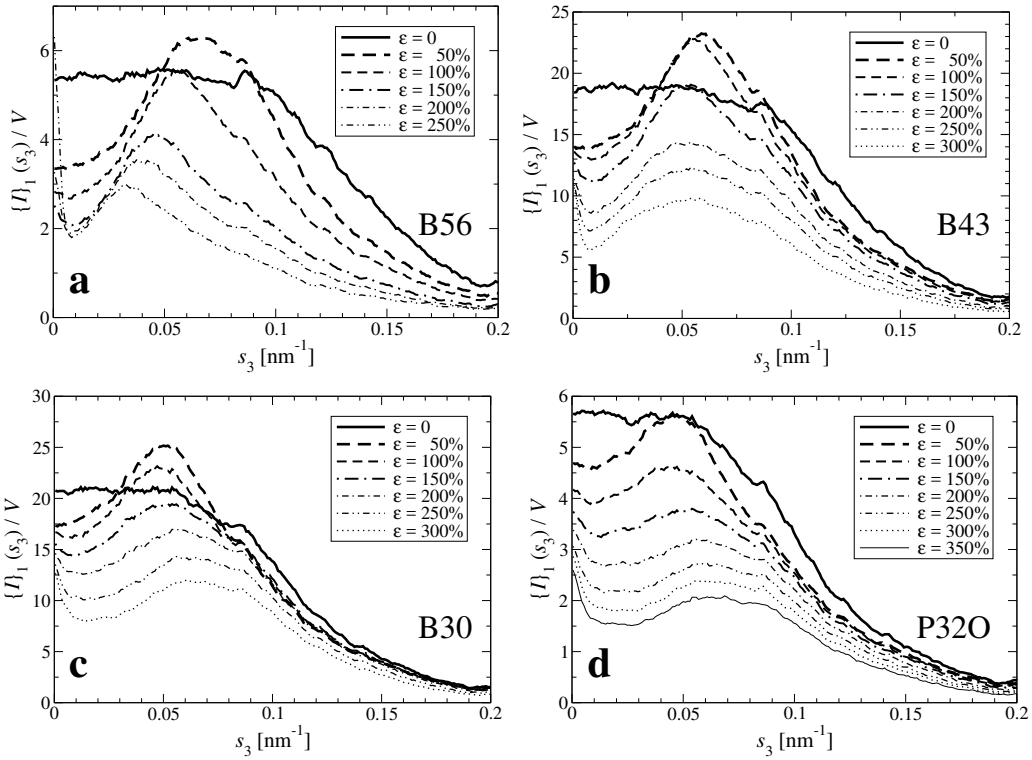

Figure 4.3: Variation of the longitudinal structure $\{I\}_1(s_3)$ in the tensile test as a function of the macroscopic strain ε. **a**) B56, **b**) B43, **c**) B30, and **d**) P32O

dinal projections for P32O, the slowly processed material that looks opaque. Here the long period position turns retrograde already above $\varepsilon > 0.5$. For this material, a pronounced hard-domain destruction starts early (Figure 4.2).

4.1.3 CDF analysis: Long periods and quasi-periodicity

In the CDFs the high intensity peaks of all materials are found in a narrow strip along the vertical line (meridian) of the pattern. This shows that the domain structure appears microfibrillar[74,75], in principle. Thus putting these strips on a wallpaper the features of the nanostructure evolution are readily demonstrated. Figure 4.4 shows data from a TPU that has been hand-cast. Here it is presented for comparison only. The reference material has HSC = 0.3 and is, as well, synthesized from MDI, BD and PTHF ($M_n = 945$ g/mol, $M_w/M_n = 2.3$). Because of the hand-casting, components are less perfectly mixed than in the machine-processed material. The corresponding chain sequence is probably different (more long hard

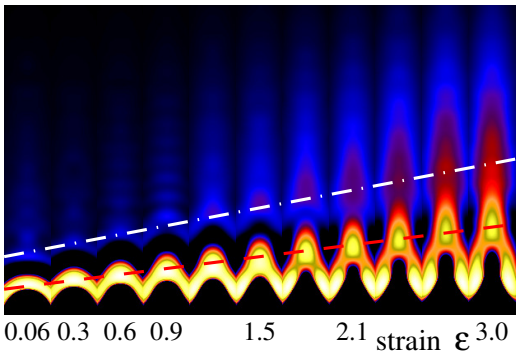

Figure 4.4: Nanostructure evolution viewed in the CDFs for a comparable hand-cast TPU material as a function of strain ε. Meridional long-period regions cut from the CDFs. $-z(r_{12,}r_3)$ $0 \leq r_3 \leq 50\,\text{nm}$, $|r_{12}| \leq 8$ nm is presented on a varying $\log(\log(-z))$ intensity scale

blocks, more single hard-module blocks) than in the machine-processed materials. The evolutions of the long-period peaks are indicated by lines. We observe an almost linear increase of the average distance to the next hard domain (dashed line). Such a proportional increase with strain for TPUs with a broad hard-block distribution has been reported in the literature[76]. The dashed-dotted line marks the linear increase of the distance from any hard domain to its second neighbor as a function of strain. In summary, we observe correlation between a hard domain and its next neighbor, and a hard domain and its second neighbor only. The average distances between them are increasing proportionally to the applied macroscopic strain.

This is completely different with the machine-processed materials. Figure 4.5 demonstrates the peculiar features of their nanostructure and its evolution. The data of the different samples are placed in blocks one below each other. Individual scaling compensates for the continuous decrease of the peak intensities with increasing ε. Logarithmic scales ensure that even weak peaks in the image stand out clearly. Obviously, the long periods accumulate in the same discrete and static bands with all materials. Results of a quantitative analysis of the peak positions are presented in Table 4.2. The bands L_n are found at the same height for all samples. We propose to explain this finding by the fact that all the different materials have been prepared from a well-mixed blend of raw materials that has led to identical conditions for the polyaddition synthesis everywhere in the mixture. Thus, all the

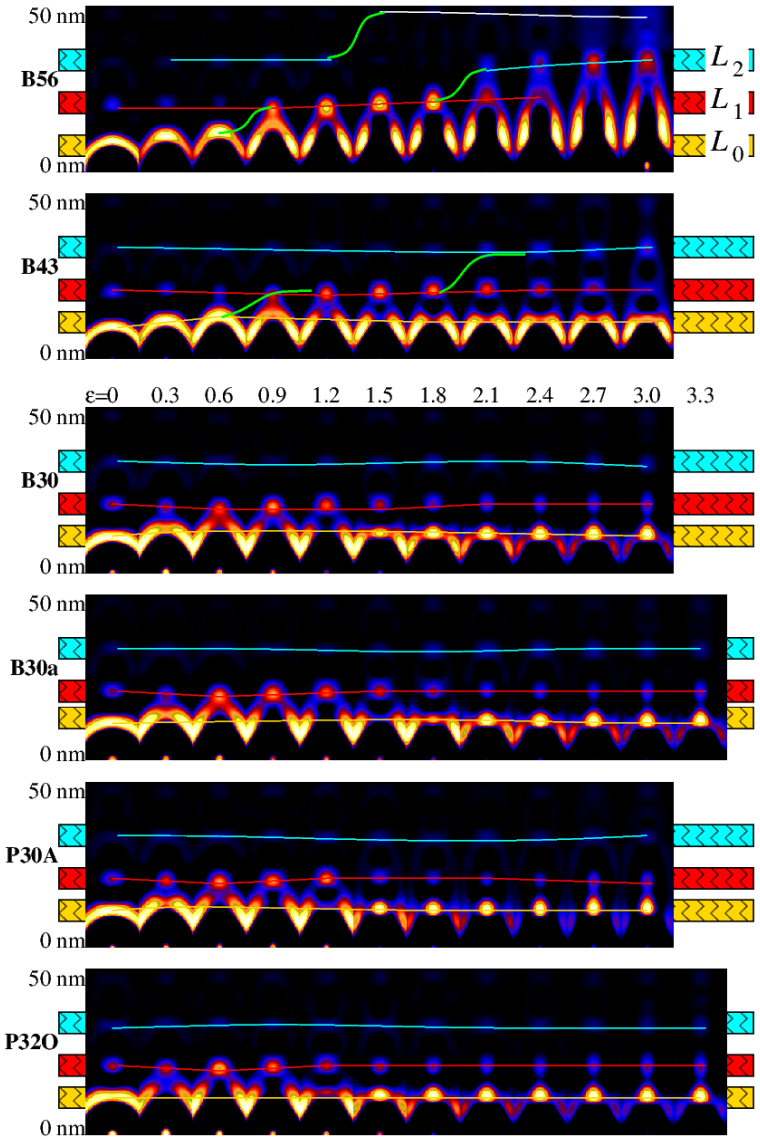

Figure 4.5: Nanostructure evolution viewed in the CDFs for all materials (top to bottom) as a function of ε (left to right). Meridional long-period regions cut from the CDFs. $-z(r_{12,}r_3)$ $0 \leq r_3 \leq 50\,\text{nm}$, $|r_{12}| \leq 8$ nm is presented on a varying $\log(\log(-z))$ intensity scale. Long-period bands are underlaid as horizontal colored strips. With material B56 (top) at the right the indexing of the band scheme is indicated (L_0, L_1, L_2)

grown chains carry the same nearly ideal distributions of hard-module sequences based on the related step lengths of the modules.

Table 4.2: Positions L_0, L_1, L_2 of long period bands determined from the CDFs at $\varepsilon \approx 2.5$

sample	L_0 [nm]	L_1 [nm]	L_2 [nm]
B56	11	21	33
B43	12	21	33
B30	12	20	32
B30a	12	20	33
P30A	12	20	33
P32O	11	20	32

Quasi-Periodicity and the SAXS data An analogy of the observed band structure to the quantum mechanical band model of solids is obvious. Thus it is suggestive to search for an algebraic construction-relation for the sequence of the L-band positions. Obviously, the positions L_n, $n = 0, 1, 2, \ldots$ are closely related to the Fibonacci sequence f_n by

$$L_n = b\, f_{n+4}. \tag{4.1}$$

Here b is a fundamental building-block length and

$$f_n = f_{n-1} + f_{n-2} \tag{4.2}$$

with $f_1 = f_2 = 1$ is the Fibonacci sequence. Comparison with Table 4.2 yields $b \approx 4\,\text{nm}$. Although for the distance distributions in the CDF the determined peak-position ratio is 3:5:8, these numbers appear to be rather close to the ratio 3:6:9 that would be expected for an arrangement of the hard domains following a one-dimensional paracrystalline stack. Thus, the interpretation as Fibonacci sequence requires additional considerations that we find by inspection of Figure 4.5 (the band positions do not appear to be equidistantly spaced), in the unusual response to the macroscopic strain, and in the synthesis path of the studied polyadducts. The corresponding relationships have been discussed in a spin-off manuscript[77]. The main points shall be briefly sketched here.

(1) The relation to the Fibonacci sequence confirms the polyaddition process (Figure 1 in [78]), in which the scattering sequences are generated by the coupling of already existing sequences.

(2) Long periods that are not integer multiples of a basic period but arranged

according to the Fibonacci sequence show that the discrete peak in the SAXS is generated from a quasicrystalline[79] arrangement of modules that form domains.

(3) The fact that the L_n-peaks do not move significantly indicates a rigidity of the hard-domain arrangement that supports its identification as a quasi-periodic structure.

(4) Because the long period begins with $f_4 = 3$, it is represented by already a sequence of 3 modules: 2 hard modules and 1 soft module (sequence: HHS). Other link options are ruled out because either the chemistry does not permit them or because for the SAXS the corresponding sequence is not a long period.

(5) Eq. (4.2) states that every new generation f_n is made from exactly one element of the previous generation, f_{n-1}, and an element of the generation f_{n-2}. This means that the (quasi-periodic) octamer ($f_6 = 8$) only is formed by the combination of a pentamer ($f_5 = 5$, sequence: HHSHS) and a trimer ($f_4 = 3$, sequence: HHS). The result is a sequence HHSHS-HHS that generates the long-period distance distribution at 32 nm in the CDF. Sequences formed more randomly do not contribute to the long-period peak in the scattering pattern, because they are not at least quasi-periodic. Nevertheless, we do not exclude their existence.

4.1.4 CDF analysis: Straining mechanisms

Each peak in the CDFs (Figure 4.5) which is bound to a Fibonacci band describes the response of a discrete L_n-group of quasi-periodic sequences to the macroscopic strain. The peak becomes discernible when there are enough similar sequences in the material. With increasing strain, we observe that some of such peaks migrate towards the upper edge of the band. Simultaneously fractions of the group frequently split, relax, and accumulate at the bottom of the band. The limited mobility is attributed to some extensibility of the soft domains, and the relaxation visualizes the relief encountered by the related sequences of the group when other hard domains fail (sacrifice). This relaxation is considerable for the materials with HSC ≈ 0.3. Here many strain probes relax and stay in the L_0-band where they provide for a small SAXS long-period. Upon arrival at the upper band edge the peak intensity often decreases. This shows that hard domains are destroyed. A further stretching is impossible. Nevertheless, some members of the group succeed to jump into the overlying band. Their domains are not completely

destroyed, but only fragmented[73]. Successful jumps are more common in the materials with high HSC, and in their scattering patterns (Figure 4.3a,b) no retrograde movement of the long period is found. In Figure 4.5 with the samples B56 and B43 s-shaped lines indicate successful jump processes.

In summary, the CDF analysis exhibits different nanoscale processes that change the population densities of strain probes in the Fibonacci bands. They ultimately cause the prograde and retrograde motions of the SAXS long-period peak.

Nanoscopic straining in the L_0-band Above we have already described the movement of the apparent SAXS long period L_a as a function of strain. In the CDF the corresponding morphological information is expanded into discrete bands. Thus we can separately study the response of only the strain probes that belong to the L_0-band. Figure 4.6 presents the result. For all materials and for $\varepsilon < 0.6$ the

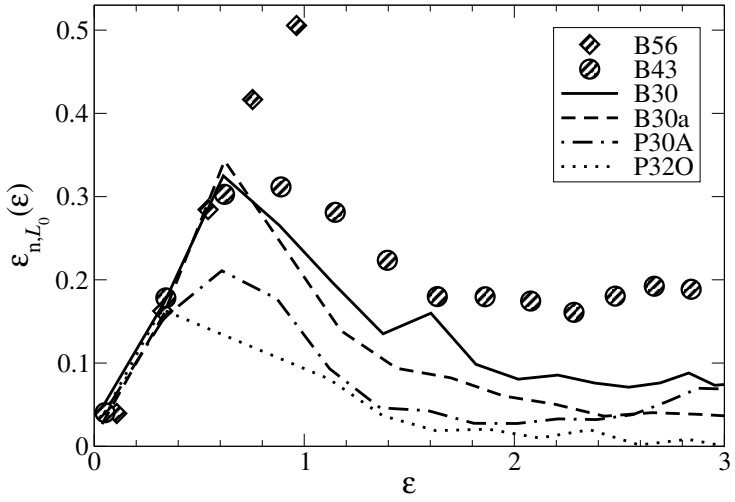

Figure 4.6: Nanoscopic strain $\varepsilon_{n,L_0}(\varepsilon)$ computed from the position of the long period maximum in the L_0-band of the CDF as a function of the macroscopic local strain ε

L_0-group entities "HHS" exhibit the same linear relation

$$\varepsilon_{n,L_0}(\varepsilon) \approx 0.5\,\varepsilon.$$

They experience only half the macroscopic strain. This means that to a first approximation intact hard domains can be considered as semi-rigid fillers. Vice

versa, the global soft matrix in the material appears to be homogeneously strained.

For $\varepsilon > 0.6$ the materials behave different. With B56 (high HSC) the L_0-group entities do not split at all. They move together to the upper band edge and jump at $\varepsilon \approx 1$ into the overlying L_1-band, with losses. For the other materials at $\varepsilon \approx 0.6$ a major sub-group is stripped off and starts to relax. This peak is traced in Figure 4.6. At $\varepsilon \approx 2$ the relaxation equilibrium appears to be almost reached. It is interesting that the residual nanoscopic strain $\varepsilon_{n,L_0}(\varepsilon = 2)$ is dependent on the material. It is highest for B43 (20%) and lower than 10% for the materials with HSC ≈ 0.3. Almost complete relaxation is exhibited with the slowly processed material P32O.

4.2 Effect of hard segment components on morphological transition during uniaxial deformation

Five machine-cast thermoplastic polyurethanes (TPU) of hard segment content $\approx 45\%$, soft segments from PTHF® 1000 and varying diisocyanates (DI) and diols (chain extenders, CE) are strained. In the process they are monitored by small-angle X-ray scattering (SAXS). Model-free data inspection shows that the nanoscopic straining mechanisms are different. Based on the inspection a compromise morphological model is constructed to analyze the morphology quantitatively. Hydrogenation of an aromatic DI completely changes the nanoscopic straining mechanism. Replacing the aromatic DI by an aliphatic one boosts the strain-induced hard-domain formation on the nanoscopic scale. On the macroscopic scale it leads to strain-induced hardening.

Starting point is a TPU with hard segments from methylene diphenyl diisocyanate (MDI) and 1,4-butanediol (BD). Additional DIs are the hydrogenated MDI (HMDI) and the aliphatic hexamethylene diisocyanate (HDI). Additional CEs are the short 1,3-propanediol (PDO) and the long 1,6-hexanediol (HDO).

The SAXS is governed by particle scattering from uncorrelated hard domains. The ensembles from arranged hard-domains are studied in real space by inspection of the CDFs. They cluster in several groups with distinct long periods (fingerprint of machine-cast TPUs). Model free screening exhibits that both the arrangement of the groups and the straining mechanisms vary. Long-ranging correlations among domains are rare. From these results a one-dimensional morphological model for the analysis of the longitudinal SAXS is built. Its components are particle scattering and the two strongest scattering entities made of 2 hard domains with some soft phase in between (soft domain). Thus the model comprises 1 “solo” and 2 “duos”.

Straining of HDI+BD increases the hard-domain volume by 35%. The long diol in MDI+HD makes a higher long period. Materials with BD and diisocyanates with rings have the most instable hard domains. For all materials the average hard domains are about 6 nm high, and the domain heights vary by 38% to 48%. With the MDI-materials the average height of the soft domains varies only in a narrow band and relaxes back to 4 nm at high strain. On the other hand, the soft domains of HDI- and HMDI-materials exhibit a smooth and flattening

increase starting from 4 nm reaching a saturation level of 15 nm. The variation of the soft domain heights with the MDI-materials is 50%, 30% with HDI+BD and even only 25% with the hydrogenated HMDI+BD.

The fit results of the MDI-materials with the less common diols show noisy oscillations of structure parameters, which stimulate speculations concerning the effect of incomplete phase separation on ensembles of small hard domains. Because every soft segment in a small hard domain reduces the stability considerably, the stability of ensembles from small hard domains should be quantizised. In the straining experiment domains containing 2 soft segments would fail before domains containing 1 soft segment. Such a mechanism would explain the indicated oscillations.

4.2.1 SAXS data evaluation

CDF analysis After preprocessing of the raw data the SAXS patterns $I(\mathbf{s}) = I(s_{12}, s_3)$ cover the cylinder $-0.29\,\mathrm{nm}^{-1} \leq s_{12}, s_3 \leq 0.29\,\mathrm{nm}^{-1}$ in reciprocal space. The patterns are transformed into $z(\mathbf{r})$, a representation of the nanostructure in real space. $z(\mathbf{r})$ is the multidimensional chord distribution function (CDF)[45]. In the historical context the CDF is an extension of Ruland's interface distribution function (IDF)[47] to the multidimensional case or, in a different view, the Laplacian of Vonk's multidimensional correlation function[80]. The CDF is an "edge-enhanced autocorrelation function"[43,44,69,70] – i.e. the autocorrelation of the gradient field, $\nabla\rho(\mathbf{r})$. $\rho(\mathbf{r})$ is the electron density inside the sample that is constant within a domain (hard domain, soft domain). Thus as a function of ghost displacement $\mathbf{r}$, the multidimensional CDF $z(\mathbf{r})$ shows peaks wherever there are surface contacts between domains in $\rho(\mathbf{r}')$ and in its displaced ghost $\rho(\mathbf{r}' - \mathbf{r})$. Such peaks $h_i(r_{12}, r_3)$ are called[47] distance distributions. Distance $\mathbf{r} = (r_{12}, r_3)$ is the ghost displacement.

Fitting of the longitudinal IDFs The IDF is fitted[57,81,82] by a one-dimensional model that describes the arrangement of alternating hard-domain heights and soft-domain heights along the straining direction. An adapted model is constructed under consideration of information which is collected by visual inspection of the projected intensities $\{I\}_1(s_3)$, the CDFs $z(\mathbf{r})$, and the IDFs $g_1(r_3)$ themselves.

Anticipating the information content of the CDFs (Figure 4.10) it is clear that the mid-range correlations among hard domains are governed by entities that do not continuously lengthen in the straining experiment. These entities cannot be described by the well-known short-range correlated entities which are based on convolution polynomials (paracrystal, stacking model, ...)[83].

Fortunately the scattering effect of the higher entities is low. Thus we neglect it to the first approximation by modeling only next-neighbor correlations. Therefore one of the model components describes entities which comprise two hard-domains with a single soft-domain in between ("duos"[84,85]). The hard domains themselves are described by a hard-domain height-distribution, and the soft domains in between by a soft-domain height-distribution. Because a considerable fraction of the curves $\{I\}_1(s_3)$ shows 2 long-period peaks (cf. Figure 4.11) which appear not to be different orders of a well-arranged system, the model has to provide a second duo component. Moreover, the dominant scattering effect of uncorrelated hard domains ("solos"[42,73,84,86]) must be considered. It is clearly detected from the shape of the IDFs $g_1(r_3)$ (Figure 4.7), which show a very dominant particle peak accompanied by only faint oscillations about the r_3-axis. The related scattering effect is pure, diffuse particle scattering which originates from those hard domains which are randomly placed in the material. In earlier work[73,87] we have called the corresponding regions in the material ("poorly arranged regions" (PAR)). Correspondingly, the duos represent the former "well arranged entities" (WAE)[73,87].

Thus our solo-duo-duo model comprises 3 components, namely solos and two different duos. This is similar as in earlier work[85]. Here we couple solos and duos by assuming that the height-distributions of isolated and correlated hard domains are identical. This assumption appears to be reasonable, because in polyurethane materials the correlation among the hard domains is extremely low, and thus a disproportionation of the hard-domain height-distributions appears improbable. Moreover, we have tested this assumption by designing a model with individual hard domains for all 3 model components and have found that it converges towards a parameter set in which all hard-domain parameters are similar and cross-correlated. The quality of the fits is demonstrated in Figure 4.7. The estimated errors of the fits (EEF)[88,89] vary in the range $0.003 \leq \text{EEF} \leq 0.012$. The average quality is EEF = 0.012. There is only one data set with a low fit quality

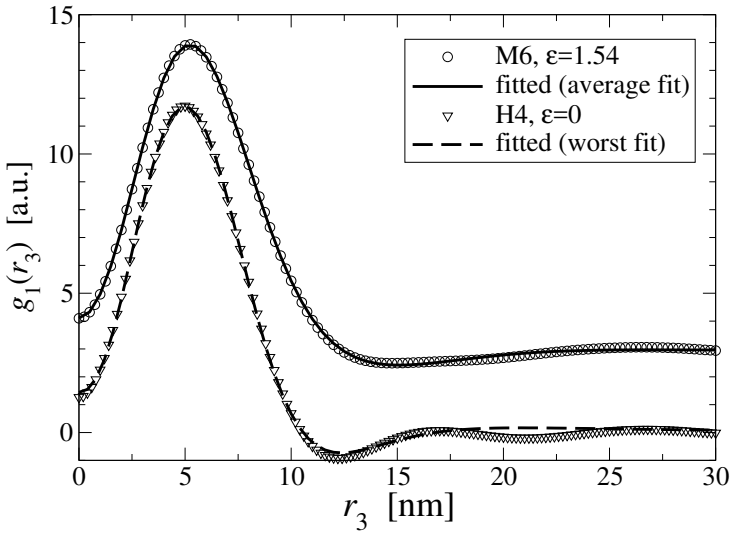

Figure 4.7: Model fits of the interface distribution function (IDF), $g_1(r_3)$. The upper pair of curves is shifted for clarity and presents the average fit quality. The lower pair of curves presents poor fit quality found only with this curve

EEF = 0.061, (sample H4 at $\varepsilon = 0$). This fit is shown in Figure 4.7, as well. There the unfitted oscillations exhibit that the material morphology comprises farther-reaching correlations among its hard domains, which are not considered in our best-compromise model.

It appears worth to mention that we have tested several other two- and three-component models as well which assume longer ranging correlations (paracrystal, stacking models, ...). For these models, we received only good fits if we adapted the ranges of the data intervals in r_3 individually. Individually means here that the intervals had to be chosen to be different not just from sample to sample but also for low and high strains. The ultimate model used here is the only model which fits all curves $g_1(r_3)$ well in the same range $0\,\text{nm} \leq r_3 \leq 30\,\text{nm}$. It separates the morphological parameters quite well, although the error bars are much wider than in a previous study[85] where it had been sufficient to consider a model with two components only.

Let us present the model parameters. The parameters of the duo components are a weight ($W_{duo,1}$ and $W_{duo,2}$ for the first and second duo, resp.), a universal average hard-domain height $\overline{H}_h$, an average soft-domain height which discriminates two duo components from each other ($\overline{H}_{s,1}$ and $\overline{H}_{s,2}$, resp.), and the relative stan-

dard deviations $\sigma_h/\overline{H}_h$, $\sigma_{s,1}/\overline{H}_{s,1}$ and $\sigma_{s,2}/\overline{H}_{s,2}$. A further standard deviation σ_H permits skewed height distributions[81,90]. As a parameter of physical meaning we compute the effective relative width[81,90] of the hard ($k = h$) or soft ($k = s,1$) domain distribution $\sigma_{k,eff}/\overline{H}_k$ from

$$\left(\sigma_{k,eff}/\overline{H}_k\right)^2 + 1 = \left(\left(\sigma_k/\overline{H}_k\right)^2 + 1\right)\left(\sigma_H^2 + 1\right) \tag{4.3}$$

using the model parameters $\sigma_k/\overline{H}_k$ and σ_H. $\sigma_{k,eff}/\overline{H}_k$ is the relative standard deviation of the skewed domain-height distribution. The second duo component ($k = s,2$) is too weak to be discussed quantitatively.

Addition of the solo component adds only one further parameter, W_{solo}. The solo borrows $\overline{H}_h$, $\sigma_h/\overline{H}_h$ and σ_H from the duos.

Let us discuss the morphological meaning of the model parameters. $W_{solo}\overline{H}_h$, $W_{duo,1}\overline{H}_h$ and $W_{duo,2}\overline{H}_h$ are proportional to the volume fraction of the respective component[85]. Summed up

$$\left(W_{solo} + W_{duo,1} + W_{duo,2}\right)\overline{H}_h = c\, v_{h,tot} \tag{4.4}$$

we compute a quantity which is proportional to the total volume fraction of hard domains, $v_{h,tot}$. Unfortunately, the morphology of our TPUs is a diluted one, i.e. the parameters $W_{duo,i}\overline{H}_{s,i}$, $i \in [1,2]$ do not catch all soft chords[52]. Only in a concentrated system $\sum_i W_{duo,i}\overline{H}_{s,i} = c\, v_s$ would be valid. Then it would be possible to eliminate c. Nevertheless, we can report $c\, v_{h,tot}$. Fortunately, proper normalization guarantees that c is the same for all the recorded SAXS patterns, and by normalization to the initial value we can study the relative variation of the hard-domain volume, $v_{h,tot}(\varepsilon)/v_{h,tot}(\varepsilon = 0)$, as a function of strain ε. The meaning of $\overline{H}_h$ and $\overline{H}_s$ is obvious. In order to discuss the volume fractions of the hard domains residing in morphologically correlated entities, we compute two more composite morphological parameters which are reasonably normalized to $v_{h,tot}(\varepsilon = 0)$ as well,

$$\left(W_{duo,1} + W_{duo,2}\right)\overline{H}_h = c\, v_{h,corr} \tag{4.5}$$

and

$$W_{duo,2}\overline{H}_h = c\, v_{h,corr2}. \tag{4.6}$$

The latter describes the volume of hard domains which are collected in the second duo component only and turns out to be of very low significance.

For each model parameter the nonlinear fitting procedure returns both the best parameter value and the estimated interval of confidence[42,88]. From these error bars the propagated error for the composite parameters (Equations (3)-(6)) is computed.

4.2.2 Mechanical performance

Figure 4.8 presents the stress-strain curves of the five materials as determined

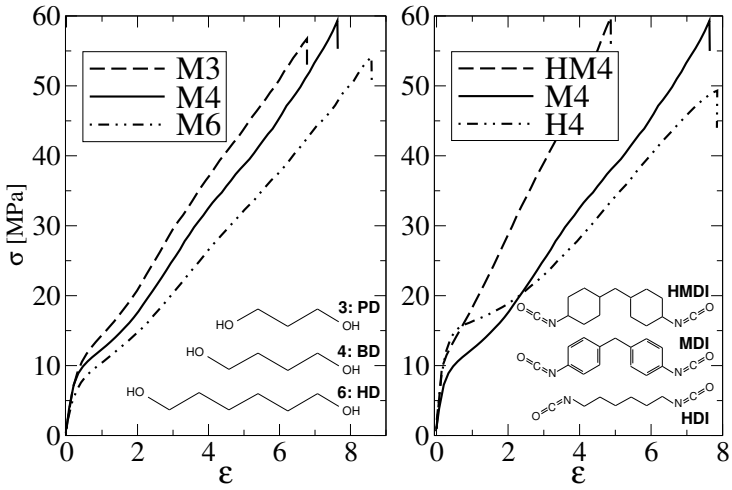

Figure 4.8: Stress-strain curves of the TPU materials. Left: Variation of the chain extender (CE). Right: Variation of the diisocyanate (DI). Chemical formulae of CEs and DIs are indicated. Here σ is the engineering stress, and ε is the engineering strain

in engineering units using a commercial tensile tester (Zwicki Z1.0/TH1S, Zwick GmbH, Ulm, Germany). The left graph shows the group of materials which contain the same diisocyanate MDI, the right graph shows the materials containing the same chain extender BD. In the left graph the modulus at high ε decreases with increasing length of the chain extender. In the right graph the material HM4 which contains hydrogenated MDI has the highest Young's modulus at $\varepsilon = 3$, and using the diisocyanate HDI instead of the standard MDI decreases the modulus at high ε with respect to the standard. Remarkable is the curve shape of material

H4, which contains the aliphatic diisocyanate. It shows the highest initial modulus ($\varepsilon = 0$), but weakens considerably for $\varepsilon > 0.8$. Its peculiar morphological evolution will be revealed by the SAXS analysis.

4.2.3 Screening the SAXS data recorded during strain-monitoring experiments

Figure 4.9 presents the central regions of the recorded scattering patterns

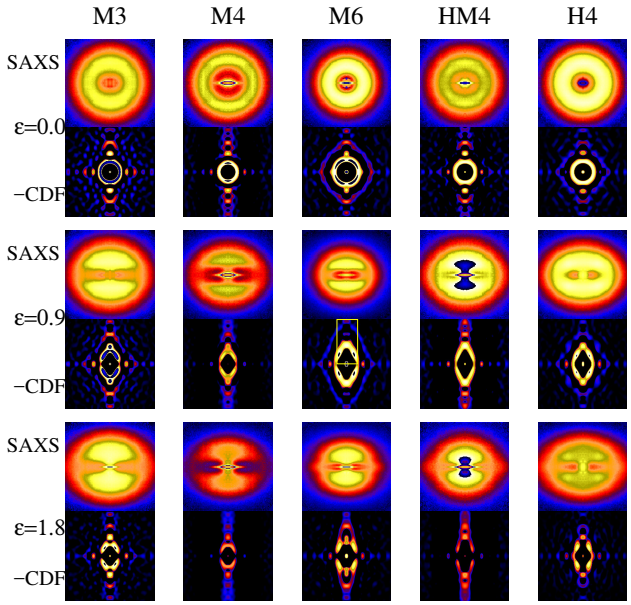

Figure 4.9: Selected SAXS data of the materials collected during continuous straining experiments. The strain ε is labeled in the text column. The top pattern in each block shows the scattering intensity ("SAXS"). This is $I(s_{12}, s_3)$, $-0.2\,\mathrm{nm}^{-1} \leq s_{12}, s_3 \leq 0.2\,\mathrm{nm}^{-1}$. The bottom pattern in each block presents the long-period peaks in the chord distribution function ("-CDF"), $-z(r_{12}, r_3)$, $-50\,\mathrm{nm} \leq r_{12}, r_3 \leq 50$ nm. The pseudo-color intensity scales are identical within each material. The straining direction (s_3, r_3 resp.) is vertical. A rectangle in the central pattern indicates the regions which are displayed in Figure 4.10

$I(s_{12}, s_3)$ and CDFs $z(r_{12}, r_3)$ computed thereof.

In fact, only the long-period face $-z(r_{12}, r_3) > 0$ of the CDFs is shown. CDFs visualize the local structure in the neighborhood of a domain: Each peak shows, in which direction and distance neighbor domains are found. It is worth to mention that a logarithmic intensity scale is chosen for the CDFs in order to visualize even

faint peaks which may be relevant for a qualitative screening and detection of straining mechanisms.

For each material a column of images is presented. The upper patterns in each column show the data of the unstrained isotropic materials. They are followed below by selected patterns from the tensile test. A text column indicates the strain ε. With increasing strain the SAXS patterns develop from isotropic patterns into layer-line patterns with fiber symmetry. The layer-shaped reflections indicate the average distance among those hard domains which appear arranged with respect to their neighbors. Under the SAXS patterns the CDFs are displayed on a logarithmic intensity scale. Qualitatively the patterns exhibit many pointed distance-distribution peaks. With some materials they even do not move much with strain. These patterns appear similar to those found in previous studies[72,91] on polyurethane materials which had been machine-cast, as well. The morphology of the strained materials is microfibrillar[74,75], in general. Thus it is dominated by sequences of hard domains arranged in the straining direction. In Figure 4.9 a rectangle in one of the CDFs indicates the region that holds the essential morphology information for a microfibrillar material. Corresponding strips have been cut out from the recorded patterns and are presented in Figure 4.10 in order to visualize the evolution of the nanoscopic morphology during the tensile tests.
In some of the materials no peak moves with increasing strain, but the population density for the higher peaks increases. This mechanism is obvious for material M4 and to some extent for the materials M3 and H4. With these materials – similar to TPUs from previous studies[91] – the fixed peak positions appear to be arranged in a Fibonacci series or close to such a series.

M6 can hardly be described by the mechanism from the previous studies, and HM4 exhibits peak movement (i.e. lengthening of the distances between hard-domains) like in hand-cast materials[92], but similar to the other materials from the present study there are several narrow peaks. The differences in the observed morphological mechanisms complicate the collective quantitative analysis of the materials studied. Nevertheless, there appears to be a chance, if we neglect far-reaching (but fortunately weak) correlations between the hard domains and restrict ourselves to the correlations between close neighbors.

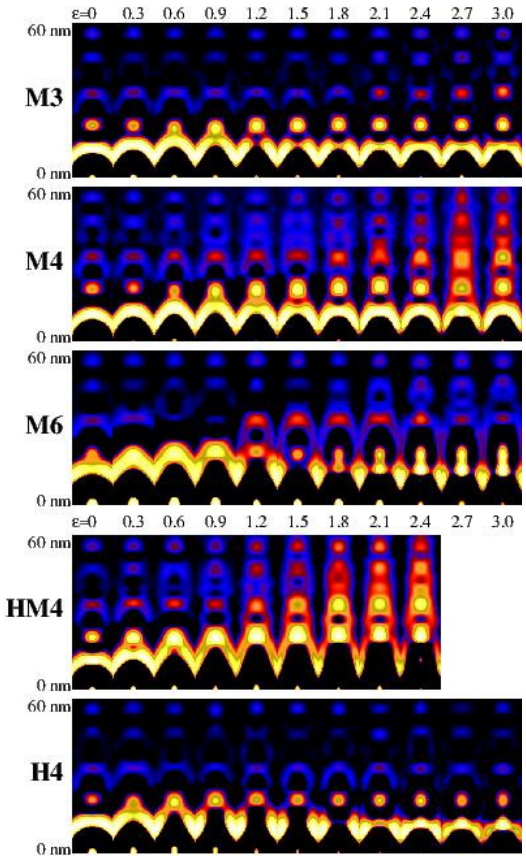

Figure 4.10: Cuts from CDFs for 5 TPU materials as a function of strain ε (left to right). CDFs $-z(r_{12,}r_3)$ $0 \leq r_3 \leq 560\,\text{nm}$, $|r_{12}| \leq 8$ nm are presented on a varying $\log(-z)$ scale. The peaks in the strips indicate correlations among hard domains in the straining direction r_3

4.2.4 Quantitative analysis of the scattering data

Bonart's longitudinal scattering Figure 4.11 shows the projections $\{I\}_1(s_3)$ of the intensity $I(s_{12}, s_3)$ on to the straining direction s_3 as a function of both the material composition and the strain ε. In almost all materials there are several curves with 2 maxima of the long-period peak. During the straining the movement of these peaks is not coupled. Therefore the model for fitting these data requires 2 independent components which consider these differently arranged hard domains. Curves and trends look similar, except for material M6 which has the long chain extender. Compared to the other materials, in M6 the SAXS peak is narrower and found at a lower s_3. Thus the average long period of the material with the longest

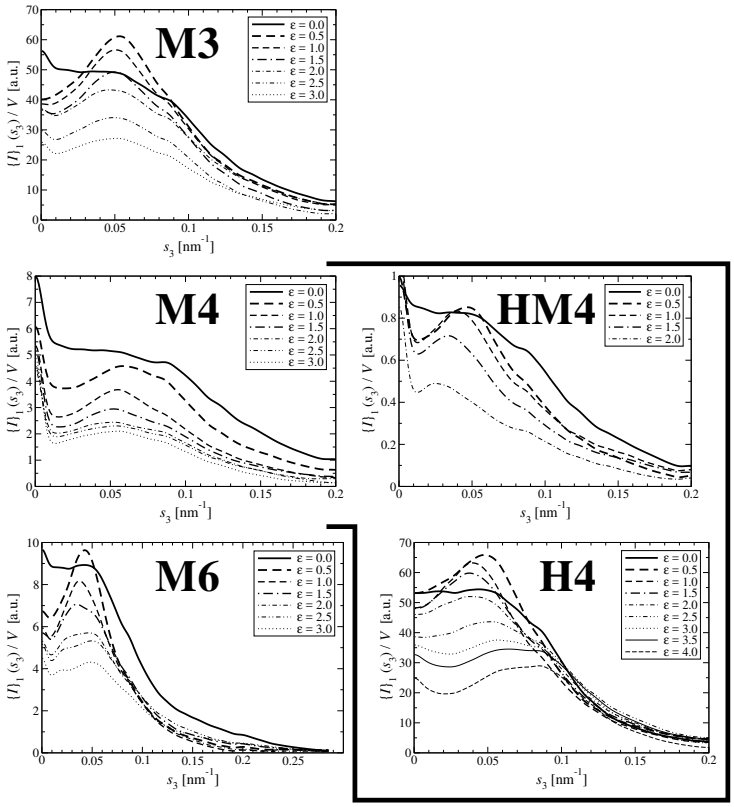

Figure 4.11: Variation of the longitudinal projected scattering $\{I\}_1(s_3)$ in the tensile tests of TPU materials as a function of composition and strain ε. Intensities are normalized for the beam flux and the irradiated volume

diol is higher and the distribution of long periods is more uniform than with the other materials.

The area under the curves $\{I\}_1(s_3)$ is the scattering power Q. In most of the materials the value is almost constant at low ε and decreases as the strain is further increasing. An exception is the material H4. It contains the only diisocyanate with an aliphatic central part, and exhibits a considerable increase of Q at low strain. This may either indicate the formation of many new hard domains or an increase of the contrast between the densities of the hard and the soft phase. A decision can be made based on the results of the following fitting by the morphological model.

Results of the IDF analysis $\{I\}_1(s_3)/V$ is a one-dimensional intensity which can be transformed into an IDF $g_1(r_3)$. It collects information on the sequences of

the finite chords which run in the straining direction r_3. The quantities which are discussed here are determined by fitting the IDFs (cf. Figure 4.7) to the presented solo-duo-duo model.

Figure 4.12 shows the variation of the quantity $v_{h,tot}(\varepsilon)/v_{h,tot}(0)$ (cf. Eq. (4.4)),

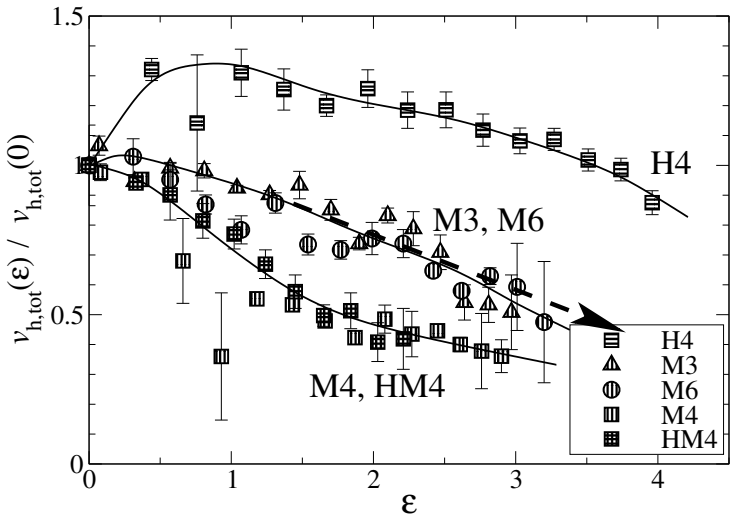

Figure 4.12: Variation of the total volume fraction of hard-domains, $v_{h,tot}(\varepsilon)$ in the straining experiments of TPUs with different compositions of the diisocyanate (letters in the designation) and different lengths of the chain extenders (digits). Error bars indicate intervals of confidence[88,89] as estimated by the regression program. A dashed line with arrow head indicates the extrapolation discussed in the text

which is the relative variation of the hard-domain volume in the straining experiment. The materials can be classified in 3 groups.

The only member of the first group is material H4. It is characterized by the only aliphatic diisocyanate. Low strain up to $\varepsilon \approx 0.5$ increases the $v_{h,tot}$ by 35%. This is a process similar to the well-known stress- or strain-induced crystallization[93–95] of polymers. Such a nanoscopic mechanism which increases the filler phase of a filled elastomer is frequently accompanied by the macroscopic mechanism of strain-induced hardening[95], and the corresponding effect is clearly visible in the stress-strain curve of H4 (Figure 4.8). At low strain the elastic modulus of H4 is higher than the modulus of all the other materials, but after the domain formation has ended at $\varepsilon = 0.8$, the mechanical performance of H4 falls off.

In the second group we find M3 and M6, the materials with the less common

chain extenders. At very low strain they exhibit a slight linear increase of the hard-domain volume followed by a linear decay. We had found this behavior in a previous study[92] with other TPU materials and had been able to relate it to the strain at break ε_b. Here, as a consequence of the required complex morphological model, the error bars of the fitted parameters are rather wide. Nevertheless, if we extrapolate (Figure 4.12, dashed line with arrow head) the upper part of the nearly linear relation to $v_{h,tot}\left(\varepsilon_{b,est}\right) = 0$, we obtain as an estimate for the strain at break $\varepsilon_{b,est} \approx 6$, which is close to the measured ε_b of the two materials (cf. Figure 4.8).

In the third group we have M4 and HM4. These materials have cyclic diisocyanates and the very common chain extender BD. Here we observe the fastest decrease of $v_{h,tot}(\varepsilon)$ as a function of ε, but above $\varepsilon \approx 2$ the decrease levels off. Thus in our TPUs the bulky DIs with the chain extender BD make hard domains which are easily unzipped under strain. This may be a consequence of poorer phase segregation that is reported[96,97] with polyurethanes from cyclic diisocyanates and BD and may be a reason for their higher ductility[97].

Using Equation (4.5) we have computed the volume fraction $v_{h,corr}(\varepsilon)$ of hard domains which belong to correlated entities (i.e. both duo components). Because the scattering effect of these entities is low, the significance of the curves becomes low, as well. Figure 4.13 shows regression curves which have been drawn through

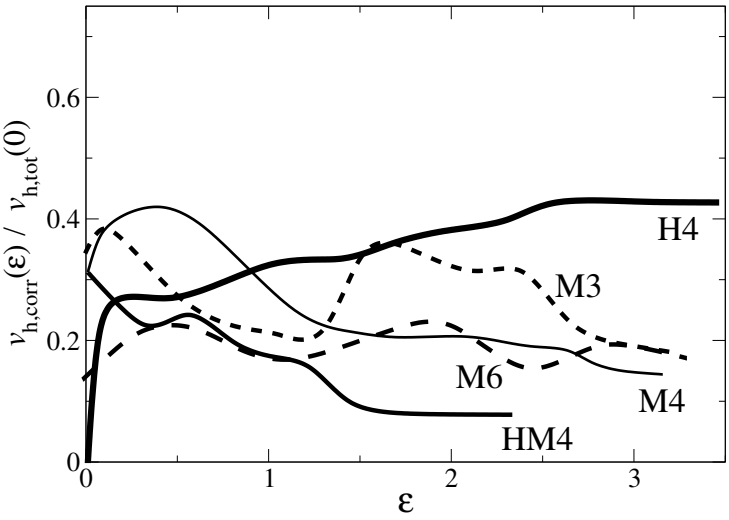

Figure 4.13: Variation of the volume fraction of hard-domains in correlated entities, $v_{h,corr}(\varepsilon)$ in the straining experiments of TPUs with different compositions. In the plot the noisy original data are suppressed for clarity

each of the sets of noisy data with wide error bars. The only result with high significance concerns the material H4. In the unstrained material the model considers all hard domains to be placed at random, although there are correlated entities which would be fittable by a (longer-ranging) stacking statistics (cf. Figure 4.7). Fortunately already for $\varepsilon > 0.12$ the short-range model appears appropriate and recognizes 25% of all hard domains as being correlated. Even for $\varepsilon > 2$ the fraction of hard-domains in correlated entities is increasing up to 40% of the initial hard-domain volume, whereas the total volume of hard-domains is decreasing considerably (cf. Figure 4.12). This indicates that in H4 under strain continuously correlated entities of hard domains are formed, even while at high strain more and more "soloistic" hard domains are destroyed. We speculate that the correlated entities may have grown from row nuclei.

In Figure 4.13 the dashed curves describe the materials with the less-common chain extenders (M3 and M6 from the second group in Figure 4.12). We are not going to comment the apparent fluctuations because of the low significance. Such fluctuations seem less pronounced in the materials which contain the chain extender BD.

The average heights $\overline{H}_h(\varepsilon)$ of the hard domains are presented in Figure 4.14. For all materials $\overline{H}_h(\varepsilon)$ is very much the same. It only varies between 5.5 nm

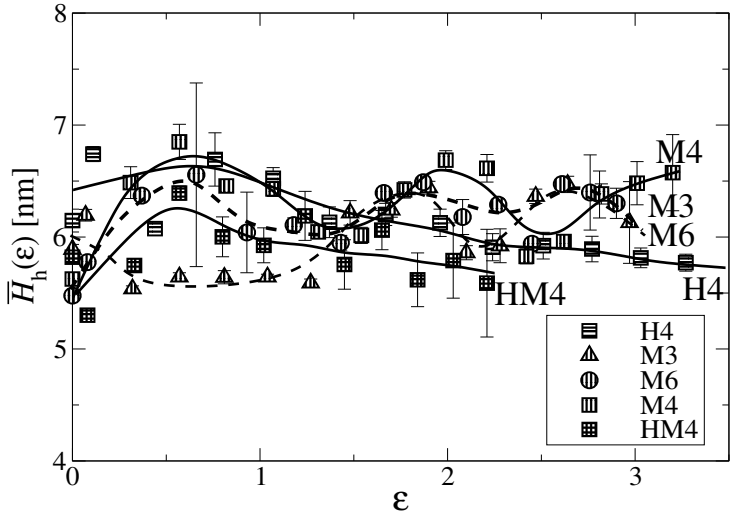

Figure 4.14: Average hard-domain height $\overline{H}_h$ measured in straining direction r_3 as a function of strain ε. Error bars indicate intervals of confidence[88,89] as estimated by the regression program

and 6.5 nm. The M-materials which are built around the diisocyanate MDI exhibit clear oscillations, whereas H4 and HM4 show simple variations of $\overline{H}_h(\varepsilon)$. If we let ourselves become inspired to a speculation by these oscillations, a possible explanation could be derived from the limited lateral extension of the hard domains. The domains are built from only a small number of hard blocks, and some of them should even have soft blocks incorporated (incomplete phase separation). Then the number of soft blocks which can be incorporated in a small hard domain must be a small integer number (e.g. 0, 1, 2). Above a certain but small limit the domain must become instable. Exposed to stress, a hard domain with 2 soft blocks would have to be considered less stable than a domain with 1 soft block. This would lead to a quantization of the strain-stability. So first the low domains with 2 soft blocks would fail, and this would increase the $\overline{H}_h(\varepsilon)$. Higher domains with still 2 soft blocks would fail later, and $\overline{H}_h(\varepsilon)$ would decrease, again. Thereafter the hard-domains with one bad chain would follow and propagate to the last element in the sequence of distortion-integers, the undistorted hard domain. Such a mechanism would cause oscillations of $\overline{H}_h(\varepsilon)$. Significant oscillations of average size parameters could thus be indications of a quantized stability in ensembles of small distorted hard domains.

If this explanation is considered appropriate, the more simple curves $\overline{H}_h(\varepsilon)$ for the materials H4 and HM4 can be explained by a more perfect phase separation with predominantly perfect hard domains. Then the observed increase of $\overline{H}_h(\varepsilon)$ up to $\varepsilon \approx 0.5$ would indicate also a height growth of hard domains which is induced by stress, in addition to the distinct stress-induced hard domain formation.

Figure 4.15 shows $\overline{H}_{s1}(\varepsilon)$, the average soft-domain heights from the 1st and strong component of correlated hard domains. HM4 and H4 show the natural behavior of elastic materials: Initially the soft material responds almost linearly to the applied strain. Finally a saturation level is reached $\overline{H}_{s1}(\varepsilon > 2) \approx 15$ nm. This is different for the M-materials. M6 shows a constant $\overline{H}_{s1}(\varepsilon) \approx 4$ nm. The strong oscillations of $\overline{H}_{s1}(\varepsilon)$ with M4 are accompanied by counter-movements of the other soft component $\overline{H}(\varepsilon)$, which indicates that the two components cannot be separated sufficiently well by the applied model. So we can only state that for M4 $\overline{H}_{s1}(\varepsilon)$ is in the same order of magnitude. M3 exhibits a certain elasticity at low strain. At higher strain the soft-domain height relaxes towards the initial level of 4 nm. For the M-materials this behavior verifies a straining mechanism [77,91].

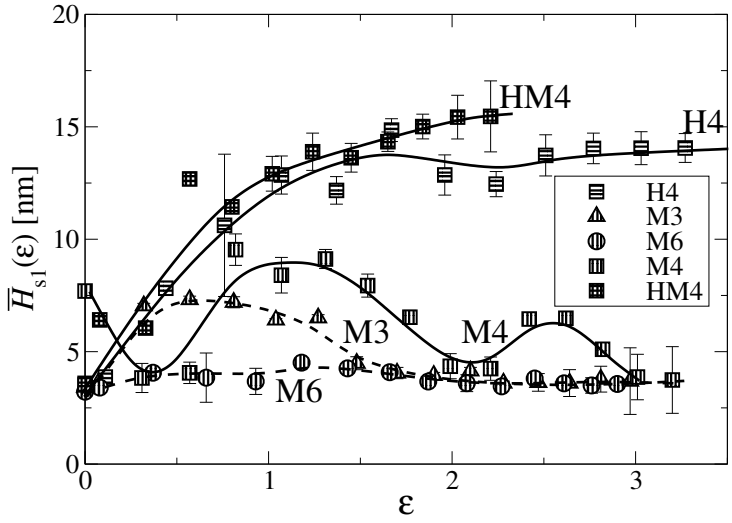

Figure 4.15: Average soft-domain height $\overline{H}_{s1}(\varepsilon)$ of the stronger measured in straining direction r_3. Error bars indicate intervals of confidence[88,89] as estimated by the regression program

This mechanism is effective, if the straining of the bulk material is predominantly accomplished by failure of hard domains from entities of limited extensibility. The dominant destruction process with the M-materials supports the speculative argument on the poorer phase-separation of the M-materials which has been derived from the noisy oscillations of their hard-domain heights.

$\overline{H}_{s2}(\varepsilon)$ shows a quite simple behavior. For the M-materials (averaged for M4) $\overline{H}_{s2}(\varepsilon) = 15$ nm is valid. Thus the second duo component catches the second kind of arranged entities[77,91] and verifies that they cannot extend upon strain, but only fail. For material M4 this statement is valid only if we average over the mentioned oscillations, which are coupled to the first duo-component. For the H-materials the curves start at $\overline{H}_{s2}(0) = 15$ nm, decrease to $\overline{H}_{s2}(0.7) = 4$ nm and stay there for higher strain. Thus for the H-materials this second duo-component collects at high strain the arranged entities which have relaxed, because they have lost connection to the physically cross-linked network. They are detectable, because the hard domains at their ends are still intact. This is a further argument for the proposition that at least some of the hard domains inside the H-materials are more stable than most of the hard domains from the M-materials.

The widths of the hard-domain height distributions are characterized by their

effective relative standard deviations, $\sigma_{h,eff}(\varepsilon)/\overline{H}_h(\varepsilon)$. For all materials the values are similar $0.38 < \sigma_{h,eff}(\varepsilon)/\overline{H}_h(\varepsilon) < 0.48$. Within this interval M4 shows the most uniform hard-domain height distributions and H4 shows the broadest.

Figure 4.16 presents the relative widths of the soft-domain height distributions.

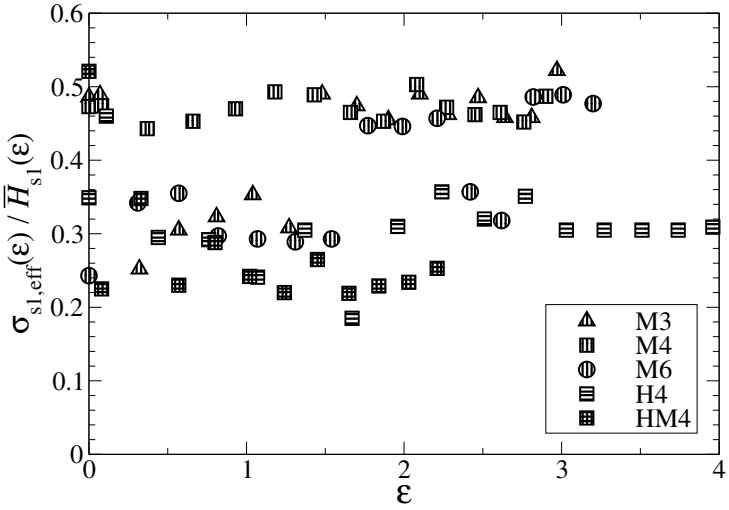

Figure 4.16: Relative widths of the soft-domain height distributions, $\sigma_{s1,eff}(\varepsilon)/\overline{H}_{s1}(\varepsilon)$ as a function of the strain ε

With the M-materials the soft-domain heights vary in the material by 50%. Here the fits have shown that the soft-domain heights are limited to variation within a band (cf. Figure 4.15). Both the other materials showed a normal nanoscopic straining mechanism starting from a linear increase of the soft-domain heights and ending in saturation. Here the variation of the soft-domain heights are considerably lower than with the materials exhibiting band-limited straining mechanisms. With H4 it is 30%, with the cycloaliphatic HM4 even only 25%.

Thus the hydrogenation of the diisocyanate (M4 $\rightarrow$ HM4) leads far away from a material with a band limited morphology whose macroscopic straining is governed mainly by the unzipping of hard domains. In addition to hard domains which are destructed, the hydrogenated material also shows stable ensembles of hard domains that extend affinely up to medium strain. From one ensemble to another, the "length of the spring" between the hard domains varies only by 25%. This may simplify the modeling of such material, because it may be allowed to assume that all springs have the same length.

4.3 Effect of nucleating agents on thermal behavior (feasibility study)

In this part of study we just monitoring the structure evolution during melting and solidification of TPUs with different nucleating agent. The samples are made by the same hard segment structure but with two different soft segments based on polyester and polyether, respectively. The nucleating agents used in the materials are introduced by BASF Polyurethanes GmbH in Lemförde, Germany.

Data Evaluation Programs have been written to extract the SSRL environmental data for automated normalization of the patterns with respect to flux and sample thickness. Machine background has been subtracted. Blind areas have been determined and masked. Aprons have been extrapolated into the blind areas. The 2D-patterns have been projected on a line for the reason to obtain a scattering curve that represents the isotropic microstructure, and at the end the IDF curves has been plotted and fitted to describe the arrangement of alternating hard-domain heights and soft-domain heights along the straining direction. An adapted model is constructed under consideration of information which is collected by visual inspection of the projected intensities $\{I\}_1(s)/V$ and the IDFs $g_1(r)$ themselves.

The $g_1(r)$ curves show only a very strong domain peak and faint short-range correlations. Thus a model should work that represents these two components, namely first uncorrelated hard domains and, second, hard domains which are correlated to a neighbor. After browsing the fits from all solidification series it turned out that this model is only good for the description of the morphology of rather cool samples. At high temperature the correlated component returns negative amounts. So we have tried the basic one-component paracrystalline stacking model[83] and have found that this model is able to fit all data from the solidification experiments with high accuracy.

The quality of the fits is demonstrated in Figure 4.17. The chosen model has the capability to smoothly transit from a correlated stack to uncorrelated hard domains. This is done automatically by the regression program setting the soft-domain parameters to values which guarantee that they do not affect the fitted curve at all.

As can be seen in Figure 4.17 we have never considered the region $r < 2.4$ nm in the fits. This has been done in order to guarantee that all data could be processed

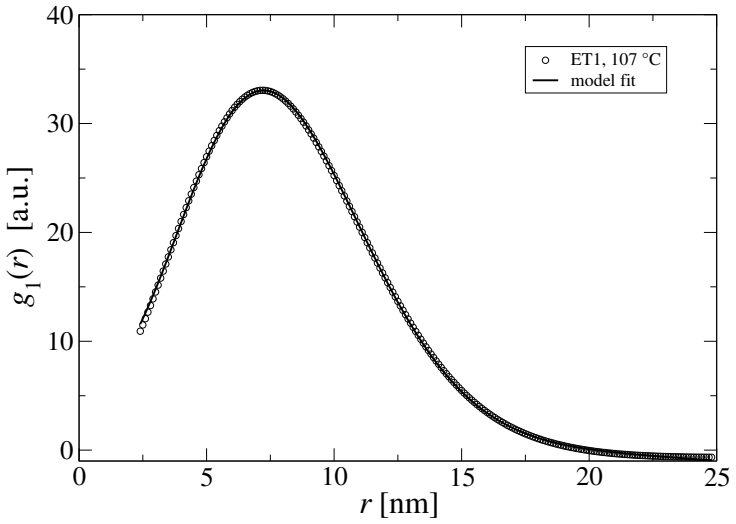

Figure 4.17: Model fit of the interface distribution function (IDF), $g_1(r_3)$ from a cooling run. The fit quality is very similar for all solidification experiments.

automatically without manual intervention. The reason is, that SAXS data from thermal-loading experiments show varying density fluctuation background which can only be subtracted correctly by manual processing of each individual data set.

4.3.1 Melting of the domain structure

Figure 4.18 presents the isotropic small-angle X-ray scattering curves taken during the heating of the materials as a function of temperature. The vanishing of the long-period peak indicates the melting of the domain structure.

Table 4.3 presents the temperatures T_{mD} of the samples at which the long-period peak and thus the domain structure just has vanished. We observe that T_{mD} of the ether-based TPU is considerably lower than T_{mD} of the ester-based TPU.

Table 4.3: Melting temperature T_{mD} of the latest-melting domains. Acronyms in parantheses indicate the parts of the sample designations

	ether (ET)	ester (ES)
blank	199 °C	212 °C
N1 (1)	190 °C	213 °C
N2 (2)	225 °C	219 °C

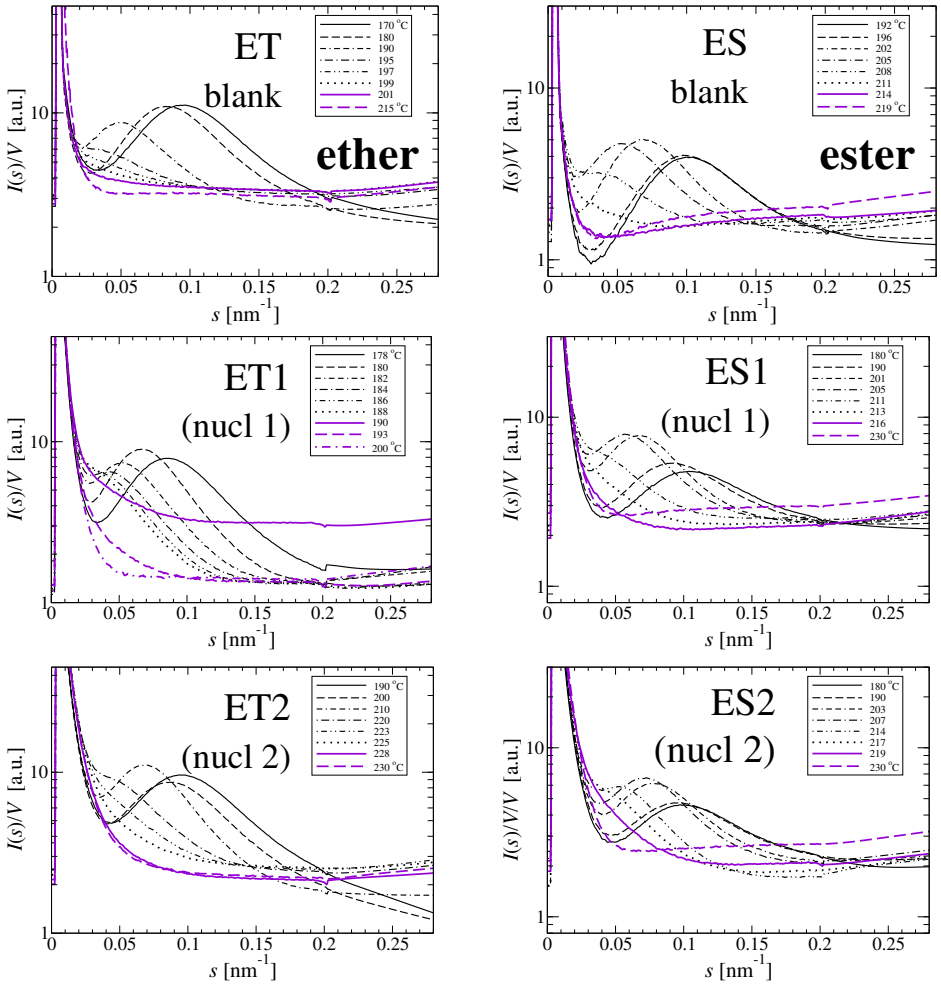

Figure 4.18: Heating (melting) of 6 TPU materials. Isotropic SAXS intensity $I(s)/V$ (logarithmic scale) as a function of temperature

Moreover, the nucleating agents change T_{mD}, and this effect is much stronger for the ether-based TPU.

Returning to the SAXS curves themselves we see that even the shapes and integrals of the long-period peaks are affected. With the ether-based TPUs samples ES and ES2 show similar curve shapes as a function of temperature: As the peak moves inward, the tail of the curve ("density fluctuation background") moves up and this indicates that during the melting a grainy paste is formed, before it becomes a homogeneous melt. The grains may be fragments of domains. For ES1 this effect is different in a spectacular way. With increasing temperature the do-

mains melt from the surface, without releasing grains into their environment. At 190 °C we observe a diffuse curve at a very high level. There the last domains have suddenly disintegrated into grains. Already at 193 °C these grains have vanished and the melt is very smooth.

With the ET-samples the effect of both nucleating agents on the domain arrangement (i.e. shape and height of the long-period peaks) appears to be similar. Moreover, all ET-materials show an increase of the tail of the SAXS curves at high melt temperature. This indicates that the melt becomes more grainy. This may be related to degradation of the polymer or to a natural effect: the increase of density fluctuations in a liquid due to increased temperature.

4.3.2 Cooling and formation of domain structure

Figure 4.19 shows the isotropic small-angle X-ray scattering curves taken during the cooling of the materials as a function of temperature. The emerging long-period peak indicates the formation of the domain structure.

It must be noted that in the solidification experiments the cooling rate was rather high (approx. 20 K/min) compared to the melting. Therefore each curve is an average taken during a time in which the temperature dropped by approx. 4 K, storage of the image takes another 6 K, and the temperature resolution is much lower than in the melting experiments. Therefore the onset of domain formation upon cooling, T_{cD}, cannot be determined with an accuracy sufficient for the characterization of different nucleating agents. Nevertheless, approximate values are presented in Table 4.4. Obviously, an effect of the nucleating agents on the ET-

Table 4.4: Approximate domain-formation temperatures upon cooling, T_{cD}, of 6 thermoplastic polyurethanes

	ET	ES
blank	140 °C	130 °C
N1	140 °C	150 °C
N2	135 °C	155 °C

samples cannot be detected. For the ES-samples, on the other hand, a clear effect of the nucleating agents on T_{cD} is observed. In particular the blank sample ES

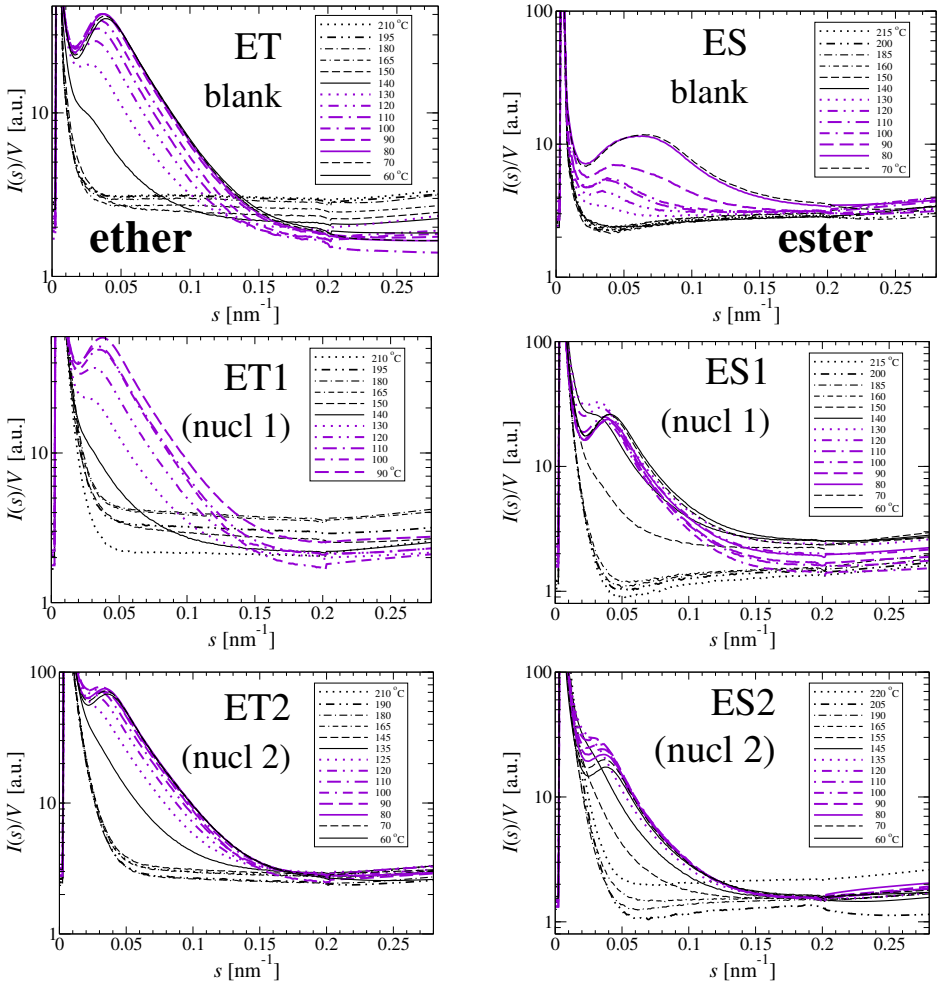

Figure 4.19: Solidification of 6 TPU materials from the homogeneous melt. Isotropic SAXS intensity $I(s)/V$ (logarithmic scale) as a function of temperature

shows a very poor discrete scattering for $T > 90$ °C. For lower temperatures the peak is unusually wide. This peculiarity is removed by addition of a nucleating agent.

Let us consider the tail intensities (fluctuation backgrounds) of the individual curves of the ET-materials (Figure 4.19, left column).

The tail intensity of sample ET decreases continuously with decreasing temperature until $T \approx 110$ °C. This decrease is stronger than expected by the thermal effect. So the phases (hard domains, soft phase) only grow smoother (by phase separation) as long as the temperature has not dropped below 110 °C. Below

110 °C the phases become more grainy, again. The low-temperature value which is finally reached is very close to the value found before the heating experiment (cf. Figure 4.18). This means that the annealing before the heating experiment (see Experimental Section) had little effect on the graininess.

The sample ET1 has shown a peculiar mechanism in the heating experiment, and now in the solidification experiment it shows a corresponding behavior. Without any domain formation the graininess of the fluid strongly increases until the temperature has dropped to 180 °C, then the graininess decreases back to the initial level when the domain formation starts at approx. 140 °C.

Sample ET2 shows an unspectacular behavior. There is a slight decrease of the "graininess" while the temperature drops to 180 °C, which can easily be explained by the temperature dependence of the fluctuation background[98–100] for a fluid. The slight increase thereafter indicates a corresponding decrease of phase homogeneity during solidification.

The ES-samples (Figure 4.19, right column) show a very peculiar shape of the diffuse scattering before domain formation (i.e. at high T). The convex bending of the curves and the different levels at high s and medium s indicate that the size distribution of the grains is not statistical, as is normal for density fluctuations. Instead, small grains with diameters of $1/s_g < 5$ nm are more frequent than big ones ($1/s_g > 20$ nm). More precisely: If we move a sphere of diameter 5 nm across the melt, the number of grains in this sphere changes considerably. If the diameter of the sphere is 20 nm, the relative variation of the number of grains in the sphere varies much less in space and time.

Sample ES shows only little variation of the tail of the SAXS curve. This means that the melt has similar homogeneity throughout the process of solidification. Sample ES1 starts from a very low tail intensity, and this indicates that the melt is very well blended (homogeneous). With decreasing temperature it exhibits a clear increase of the tail of the SAXS, indicating that the solidification goes along with a clear increase of graininess inside the phases ending at the level of sample ES. Thus the nucleating agent "nucl I" makes a smooth melt, but not a well-separated domain structure. This is different with sample ES2. Here the high-temperature melt appears grainy, becomes considerably smoother at 205 °C with a slightly preferred grain size of 6 nm. Then the SAXS tail, again, raises a bit but finally stays on a rather low graininess as compared to ES and ES1.

4.3.3 *Discussion of long-period determination*

In the analysis of the SAXS from polymers it is very common to quantitatively discuss long-period values $L = 1/s_L$ determined from the positions s_L of the highest intensity $I(s)/V$ in the peak. We refrain from doing so for several reasons. First, the width of the long-period distribution is varying considerably in the experiments. Second, the varying background intensity would have to be subtracted. Third, the domains are no lamellae, so the application of a "Lorentz correction" would not be appropriate. Nevertheless, the reader may estimate long-period values from Figure 4.18 and Figure 4.19.

The longitudinal scattering $\{I\}_1(s)/V$

Figure 4.20 presents the longitudinal scattering curves $\{I\}_1(s)/V$ taken during the melting of the TPU samples.

Figure 4.21 shows $\{I\}_1(s)/V$ taken during the cooling of the TPU materials from the melt. Here the tails of the SAXS curves are governed by the 1D fluctuations of the electron density along lines which cut through the material and can be chosen deliberately. In contrast to the isotropic SAXS curves $I(s)/V$ in Figure 4.18 and Figure 4.19 here the curves are displayed on a linear intensity scale because they show less features than the isotropic SAXS curves. Moreover, most of the curves from the molten state are omitted because of their low information content.

The curves from ES are very peculiar. In $\{I\}_1(s)/V$ the first extra scattering above the level of the diffuse scattering is observed very late at 90 °C. This peculiarity has already been addressed in the discussion of the respective intensity curves $I(s)/V$.

4.3.4 *Morphology evolution from IDFs*

The morphological evolution during the melting of the TPU materials is visualized in the IDFs $g_1(r)$ presented in Figure 4.22. The IDFs are dominated by a very big peak at small r followed by some faint oscillations which describe the weak correlations between some of the domains in the material. Only these few correlations make the SAXS long-period peak. Neglecting the faint contribution of correlated domains, the strong IDF peak represents the chord length distribution

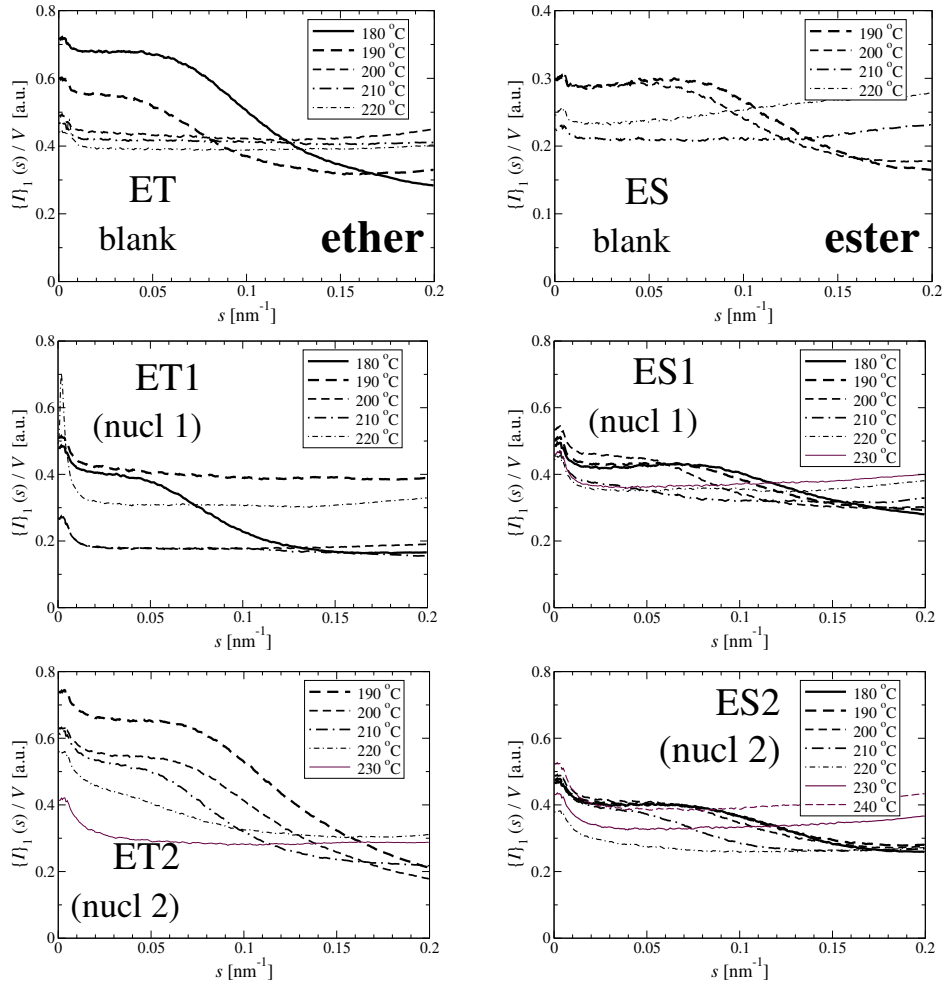

Figure 4.20: Heating (melting) of 6 TPU materials. 1D longitudinal SAXS intensity $\{I\}_1(s)/V$ as a function of temperature

of the uncorrelated hard domains.

The integral of the peak is controlled by two parameters. These are the phase segregation, (i.e. the contrast between hard-domain density) and the population density of hard domains in the volume. With increasing temperature the integral decreases, as more and more of the hard domains melt away.

Comparing materials that are differently doped, the ether-based materials exhibit a clear effect of the nucleating agent on the peak integral. By nucleating agent 1 the peak integral is halved. Thus the material either contains hard domains which are less pure, or there are less hard domains in the volume left-over

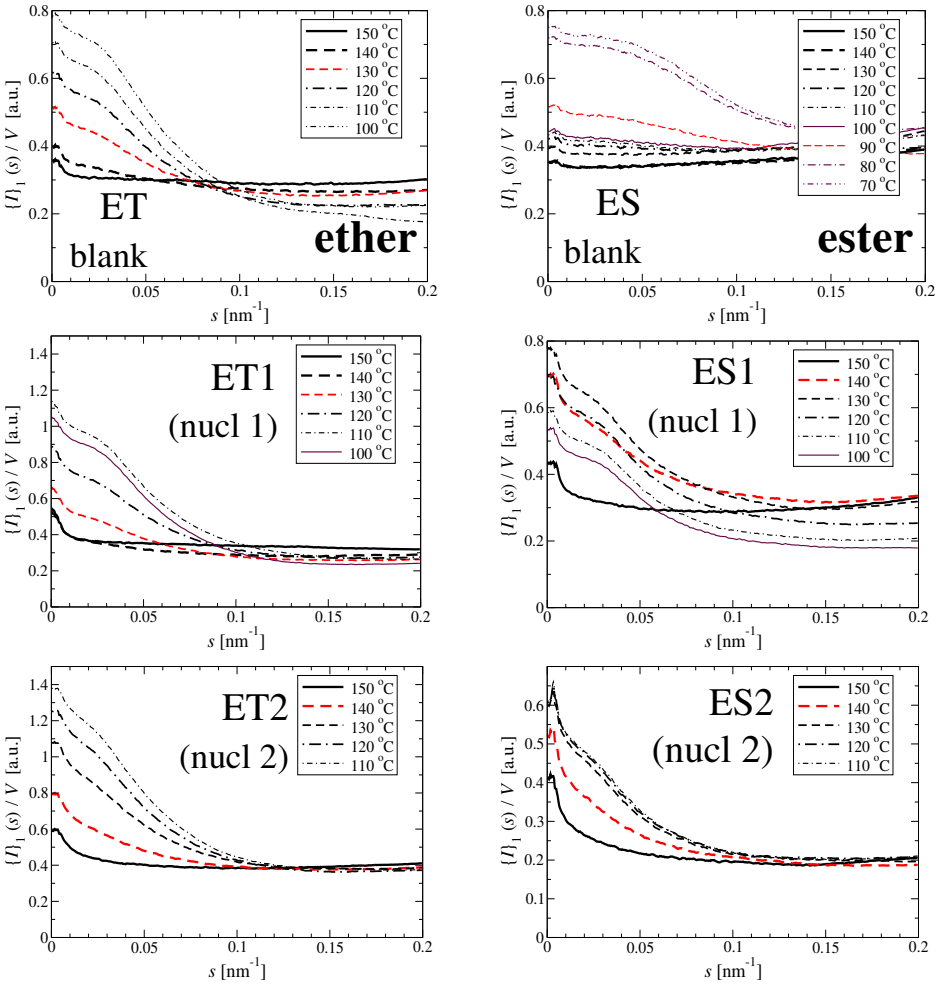

Figure 4.21: Cooling (solidification) of 6 TPU materials from the isotropic melt. 1D longitudinal SAXS intensity $\{I\}_1(s)/V$ as a function of temperature

at 180 °C in the heating process. Addition of nucleating agent 2 increases the peak integral somewhat with respect to the undoped material. So this agent appears to be more suitable for applications that rely on a high fraction of stable hard domains.

On the other hand, the ester-based materials show no effect of the nucleating agent on the peak integral. This means that there is probably little effect on phase segregation or population density in the annealed material during heating.

Let us now discuss the peak shape. With ET and ET1 both the positions and the widths of the peaks are very similar compared to each other. Moreover, the peak

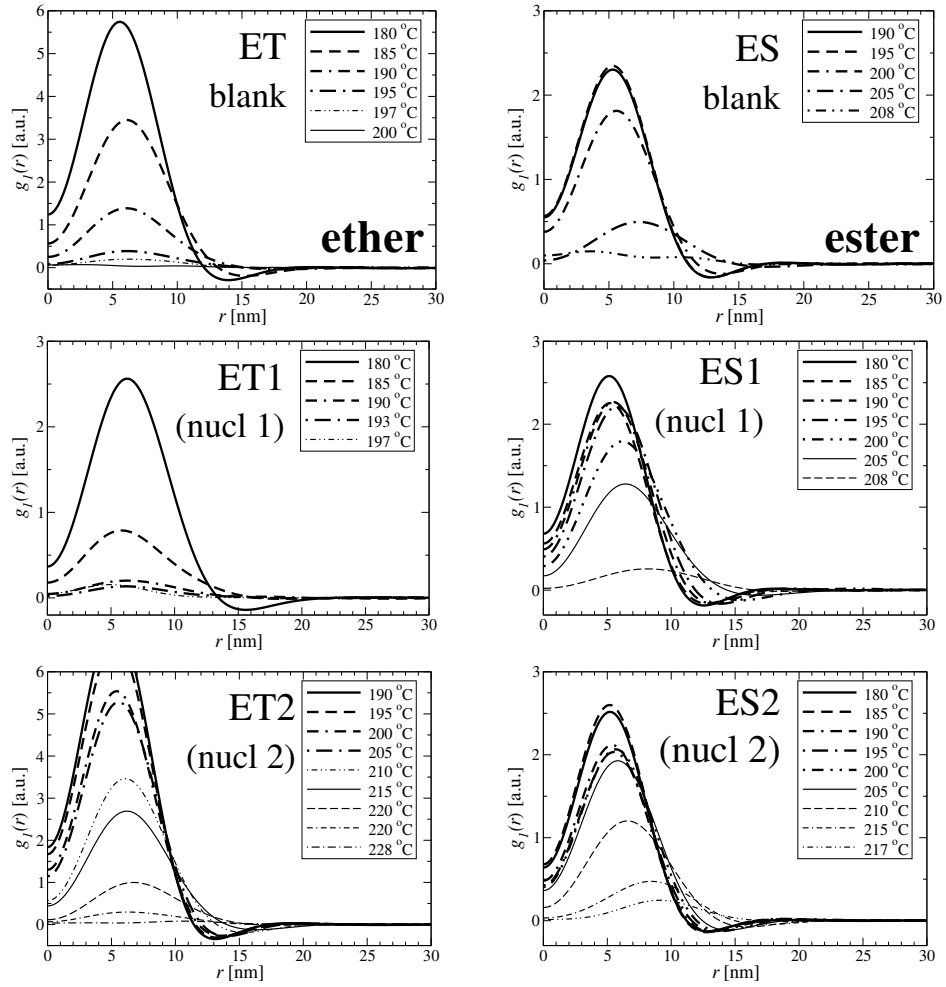

Figure 4.22: Heating (melting) of 6 TPU materials. IDFs $g_1(r)$ as a function of temperature. The curves are computed from the 1D longitudinal SAXS intensity $\{I\}_1(s)/V$

shape does not change during the melting process. With ET2 the peaks are placed at lower r indicating that the nucleating agent makes the hard domains smaller. Here, as well, the peak shape does not change during the heating. Thus the ET-mechanism of morphology destruction during heating resembles an indiscriminate annihilation of hard domains, regardless of their size. Big hard domains in ET-materials are not more stable than small ones.

With the ES-materials this is different. Here with increasing temperature the peak moves to higher r, indicating that the bigger hard domains melt later than

the smaller ones. Thus only the material ES confirms the common notion of the melting of a polymer.

The corresponding solidification process data are presented in Figure 4.23 .

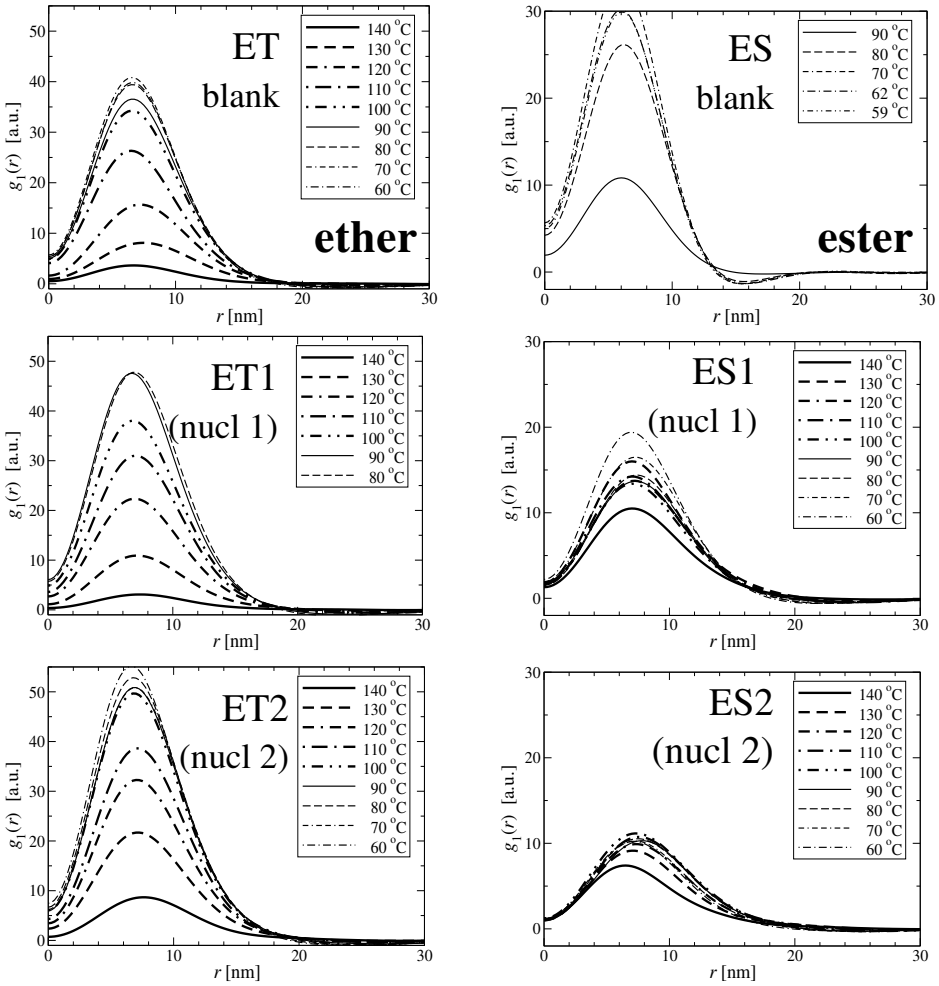

Figure 4.23: Cooling (solidification) of 6 TPU materials from the isotropic melt. IDFs $g_1(r)$ as a function of temperature. The curves are computed from the 1D longitudinal SAXS intensity $\{I\}_1(s)/V$

Considering the peak intensities of the ET-materials there are, astonishingly, no big differences for the doped materials. Both materials slightly increase the peak integral and thus increase hard-domain number or perfection. The difference concerning the heating of ET1 indicates that many of the hard-domains in ET1 melt below 180 °C where the SAXS monitoring has been switched on.

With the ES-materials we now observe considerable differences. Both nucleating agents reduce the peak integral, and the effect is strongest with ES2. We should test all the morphologies after annealing at 100 °C for 20 h.

Concerning the peak shapes, all the ET-materials show peaks which are rather similar. Neglecting the data at 140 °C directly after the onset of morphology formation, the peak slightly moves to lower r, indicating that smaller hard domains are formed at lower temperatures. Below 100 °C the peaks do neither change shape nor integral any more. With the ES-materials we observe different changes of the peak shape. With ES we have no IDFs from temperatures above 90 °C, because above 90 °C there is only diffuse scattering of an increasingly grainy melt. Where IDFs can be computed, the shape of the main peak does not change, but we observe a clear negative peak emerging between 90 °C and 80 °C at $r = 15$ nm. This indicates the formation of domain correlations, probably by inserting the last new hard-domains into suitable gaps (car-parking mechanism)[84]. With ES1 and ES2 no formation of correlation is observed at low temperature. ES2 shows peaks of constant shape, but with ES2 the peaks move to higher r with decreasing temperature. This unusual behavior may be explained by a hard-domain growth (maturation) during the solidification process.

IDF fits

All the IDFs from the solidification experiments have been fitted by the stacking model, as described in the section "Data evaluation". The poorly structured curves $g_1(r)$ suggest that only some of the structural parameters can be determined with good accuracy. This is confirmed by the output of fitting program. The intervals of confidence of only the average hard-domain chord length, $\overline{d}_h$, and of the overall weight parameter, W, return narrow error bars. From the combination of both parameters, $c\,\widetilde{v}_h = W\,\overline{d}_h$, we compute a quantity which were proportional to the volume fraction[85] v_h of the hard domains, if only the contrast between hard and soft phase would not change during the solidification experiment. c is the unknown proportionality factor. The contrast is the density difference between the hard phase and the soft phase, and these densities increase independently with decreasing temperature during the solidification process. The unknown net effect is determined by the ratio of the expansion coefficients. Therefore we call $\widetilde{v}_h$ a pseudo volume fraction. Nevertheless, its variation as a function of temperature

indicates a trend which visualizes the rate of colonization of the volume by hard domains. Different trends can help to characterize the different effects of nucleating agents on the colonization rate.

Figure 4.24 presents the results of the hard-domain colonization data. Here

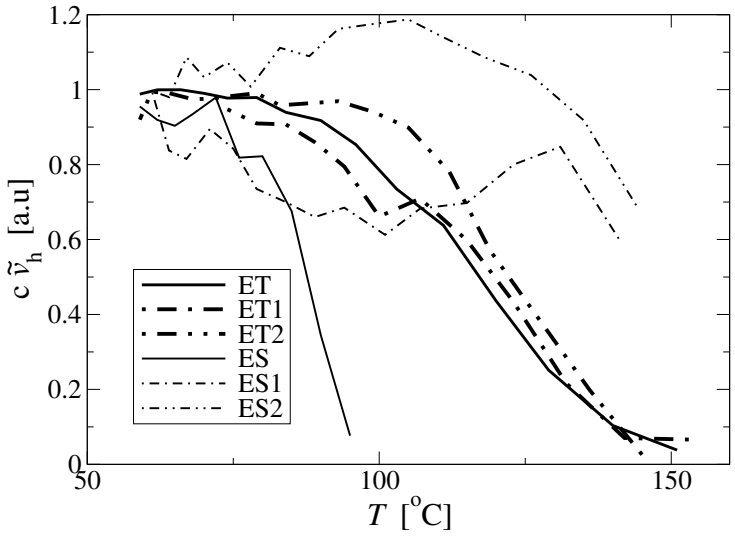

Figure 4.24: Differences in the colonization rate by hard-domain volume for different TPU materials in relative units. $\widetilde{v}_h$ is only a pseudo volume fraction of hard domains, because the phase densities change during cooling

the estimated error bars are omitted, because they are very narrow. We observe that for the ET-materials the hard-domain colonization is not changed by the nucleation agents, but there is a considerable effect on the ES-materials. For the pure ES and above 100 °C there is no preferrential grain size which would allow to define a hard domain. Such a grainy morphology is not observed when one of the two nucleating agents is present, and hard domains can be identified right from the beginning of phase segregation. In fact, both nucleating agents make that the volume is occupied by hard domains instanteneously when the phase segregation starts, and there is only little extra volume that is filled during the cooling. The depression in the curve of ES1 looks somwhat strange, but the course of the ES2-curve can be explained by the contrast change which has been impossible to consider.

Figure 4.25 displays the variation of the average chord length $\overline{d}_h$ of the hard domains, which is a measure of the hard-domain size. In material ES the hard do-

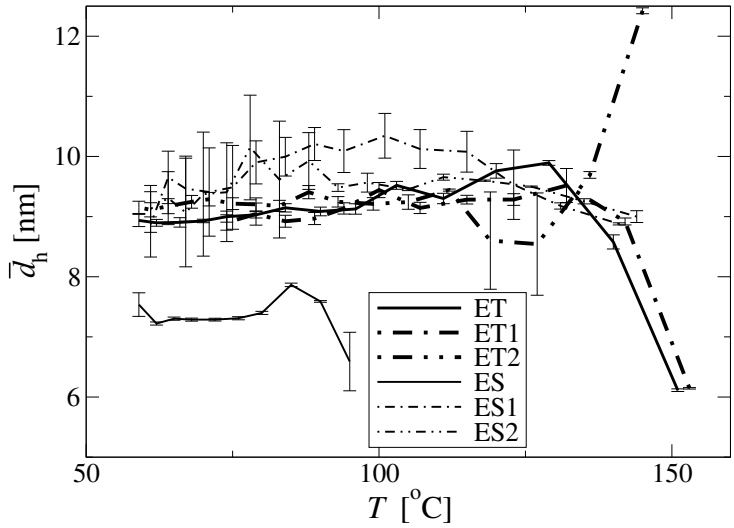

Figure 4.25: Differences in the colonization rate by hard-domain volume for different TPU materials in relative units. $\widetilde{v}_h$ is only a pseudo volume fraction of hard domains, because the phase densities change during cooling

mains are much smaller than in the other materials. This finding can be explained by the fact that in this material the formation of hard domains with a measurable size starts from a grainy precursor structure but not from a relatively smooth melt in which the domain growth is not hindered by pre-existing grains. For all the other materials the final average size of the hard domains is already reached at 130 °C. Only for ET2 we observe that the decrease of temperature generates smaller hard domains. In this material a growth mechanism of hard domains is of secondary importance.

Conclusions The experiments have shown that there is an effect of the nucleating agents on the morphology evolution. Nevertheless, the data look "smeared" because of the long exposure (slow detector) and possibly a temperature gradient inside the samples. Moreover, a possibility should be sought to heat and cool the samples with a constant role for direct comparison with other methods (e.g. DSC)

Chapter V

Conclusion and Outlook

Owing to the combination of novel experimental methods and data processing routines, new insight was gained into the structure reports of various TPUs under load. The employment of third generation synchrotron radiation opened the possibility to carry out in situ expriments.

In a well-controlled machine process polyurethane block copolymer can be generated, in which the sequence statistics is closer to the ideal of polyaddition than in hand casting. The sequence statistics appears to be narrower. We have generated more order by process control, whereas Blundell et al. [76] have achieved similar by changing the synthesis. They, too, report that in the tensile test, the strain probes are no longer elongated proportional to the macroscopic strain. Since they derive their results only from the response of the SAXS peaks, they cannot describe the mechanism in more detail. By a CDF analysis we manage to find rudimentary quasi-periodic sequences from hard and soft modules which are reflected in the arrangement of the hard domains of our polyadducts. A natural property of quasi-periodic strain probes appears to be a low elasticity limit. Together with the sacrification of hard domains and the relaxation of strain probes this leads to the retrograde movement of the SAXS long-period peak in the tensile test.

Bonart[101, 102] has raised the question why discrete scattering is observed with strained TPUs “although no vertical periodicity is found at any point of the structure” and has proposed an explanation that requires some arrangement in the direction perpendicular to the straining direction. The materials of the present study indicate a more detailed explanation that is based on short one-dimensional quasi-periodic sequences of hard domains. These sequences are identified as the strain-probes that lead to the observed discrete (peak-generating) SAXS of the polyadducts.

Generally, the discrete SAXS of polyurethanes appears weak compared to the scattering of polyolefins or of triblock copolymers. This finding can now be related to the finding that predominantly few one-dimensional quasicrystals cause the discrete SAXS of the studied TPUs. Such strain probes have probably been produced with only statistical probability because we assume that many of the resulting sequences in the polyaddition are not generated according to the strict scheme of generations that rules the Fibonacci sequence. Such off-scheme sequences do not contribute to the discrete SAXS because their domains are not correlated. Thus, in a TPU there are probably comparatively few sequences from hard and soft domains (strain probes) that contribute to the long-period peak.

The discrete SAXS monitors only the vicinity of the strain probes in the TPUs. Are these regions representative? An indication of a positive answer is found in Figure 4.6. There the beginning of all curves shows the same low slope compared to the macroscopic strain. This indicates that at least at low strain the correlated hard domains can be considered as rigid fillers in a homogeneous, affinely strained soft phase.

An interesting result concerns the occurrence of relaxing HHS sequences when stretching. The systematic variation of sample parameters has led to clear indications herein. Correspondingly, more domains are sacrificed and less experience relief when the HSC is rising from 30% to 43%. Finally relaxation is absent in the material with HSC = 56wt.-%. Moreover, the amount of relaxation (Figure 4.6) appears as a function of processing, additives and chemical crosslinking. These relationships may become important for the modeling of TPU materials.

Beyond the scope of this study is an in-depth analysis of the longitudinal projections. These one-dimensional scattering curves may be treated by the well-known analytical apparatus[42] of one-dimensional scattering that has been developed for morphologies of stacked lamellae. The detected quasicrystalline character of the probes indicates how to construct structural models for an analysis.

The first study showed that the chemical composition (hard and soft segment content), the chain topology (linear versus branched) and polymer processing of TPUs have an important impact on the polymer morphology and its nanoscopic evolution during straining. This has become clearly evident from the relative variation of the invariant Q (Figure 4.2) and the dependency of the nanoscopic strain as a function of the macroscopic local strain (Figure 4.6). As far as we know,

such an analysis has not been carried out before. It results in a deeper insight into the relationship between structure and properties of this class of materials. A fundamental knowledge of the correlation of the above mentioned system variables, the nanoscopic behavior and the ultimate macroscopic properties allows rational design of TPU for a whole range of applications.

In the second study for the first time we have measured the mechanical hard-domain stability of various conventional polyurethanes simultaneously in strain tests. For this purpose we have exploited our new method[85, 92] for determining the variation of the hard-domain volume from SAXS data recorded during the tests.

As also reported in other papers, incomplete phase separation[96, 97] and stress-induced hard-domain formation[95, 103] appear to be far more important for the mechanical performance of our polymers than the hydrogen bonds[104, 105] which are often discussed in the context of thermal stability.

The third study indicated that homogeneity and graininess of the melt appear to vary as a function of nucleating agents before the domains are formed doing solidification. This aspect should be given attention in following experiments. The entire cycle should be monitored, not only the solidification branch of the process.

In conclusion, the application of a series of novel and sophisticated experimental techniques gave new insight into structure-property relationships of Thermoplastic polyurethane under physical deformation. This hopefully contributes to a more fundamental understanding of the relation between morphology and physical properties of TPUs of varying composition.

Suggestions for future work:

1. Investigation of nanoscopic structure evolution in the load-cycling test as a function of varying hard segment content and components.

2. Combined heating-stretching cycles to study shape-memory behavior of TPU materials.

3. Investigation of the effect of polyester- and polyether-soft segments on morphological transition during uniaxial deformation.

Bibliography

[1] P. Mackey, in *The Polyurethanes Book*, ed. by D. Randall, S. Lee (John Wiley, New York, 2003), chap. 19, pp. 285–294

[2] C. Prisacariu, *Polyurethane Elastomers* (Springer Vienna, Vienna, 2011). DOI 10.1007/978-3-7091-0514-6. URL http://link.springer.com/10.1007/978-3-7091-0514-6

[3] C. Buckley, C. Prisacariu, a. Caraculacu, Polymer **48**(5), 1388 (2007). DOI 10.1016/j.polymer.2006.12.051. URL http://linkinghub.elsevier.com/retrieve/pii/S0032386107000134

[4] C. Prisacariu, I. Agherghinei, Journal of Macromolecular Science, Part A **37**(7), 785 (2000). DOI 10.1081/MA-100101123. URL http://www.tandfonline.com/doi/abs/10.1081/MA-100101123

[5] C. Prisacariu, *Polyurethane Elastomers. From Morphology to Mechanical Aspects* (Springer, Wien, New York, 2011)

[6] Q. Guo, *Polymer Morphology: Principles, Characterization, and Processing* (John Wiley & Sons, 2016)

[7] C. Prisacariu, E. Scortanu, International Journal of Polymer Analysis and Characterization **15**(5), 277 (2010)

[8] A.A. Beltrán, L.A. Boyacá, Latin American applied research **41**(1), 75 (2011)

[9] Z.S. Petrović, J. Ferguson, Progress in Polymer Science **16**(5), 695 (1991)

[10] URL http://http://www.intermediates.basf.com/chemicals/topstory/polythf/

[11] H. Chao, N. Tian, Cray Valley USA, LLC Exton, Pennsylvania USA, PA **19341** (1998)

[12] J.G. Drobny, *Handbook of thermoplastic elastomers* (Elsevier, 2014)

[13] D. Martin, A. Osman, Y. Andriani, G. Edwards, Advances in polymer nanocomposites: types and applications, 1st edn. Woodhead Publishing, Cambridge pp. 321–350 (2012)

[14] G. Oertel, L. Abele, *Polyurethane handbook: chemistry, raw materials, processing, application, properties* (Hanser Publishers. Distributed in USA by Scientific and Technical Books, Macmillan, 1985)

[15] S.B. Clough, N.S. Schneider, A.O. King, Journal of Macromolecular Science, Part B: Physics **2**(4), 641 (1968)

[16] C.P. Buckley, C. Prisacariu, C. Martin, Polymer **51**(14), 3213 (2010)

[17] D.S. Trifan, J.F. Terenzi, Journal of Polymer Science **28**(117), 443 (1958)

[18] Y.M. Boyarchuk, L.Y. Rappoport, V.N. Nikitin, N.P. Apukhtina, Polymer Science USSR **7**(5), 859 (1965)

[19] R.L. McKiernan, S.P. Gido, J. Penelle, Polymer **43**(10), 3007 (2002)

[20] R.L. McKiernan, A.M. Heintz, S.L. Hsu, E.D.T. Atkins, J. Penelle, S.P. Gido, Macromolecules **35**(18), 6970 (2002)

[21] S. Abouzahr, G.L. Wilkes, Z. Ophir, Polymer **23**(7), 1077 (1982)

[22] C. Prisacariu, E. Scortanu, Encyclopedia of Analytical Chemistry (2006)

[23] T. Speckhard, K. Hwang, S. Cooper, V. Chang, J. Kennedy, Polymer **26**, 70 (1985). DOI 10.1016/0032-3861(85)90058-8

[24] Y. Huang, D.R. Paul, Journal of Polymer Science Part B: Polymer physics **45**, 1390 (2007). DOI 10.1002/polb. URL http://arxiv.org/abs/cond-mat/0406218

[25] E.F.T. White, British Polymer Journal **18**(6), 403 (1986)

[26] K.W. Rausch Jr, A.A.R. Sayigh, Ind. Eng. Chem. Prod. Res. Development, **4**(2), 92 (1965)

[27] M. Song, H. Chen, C. Jiang, B. Zhao, X. Li, Macromolecular theory and simulations **11**(8), 845 (2002)

[28] J. Tang, Y. Wang, H. Liu, L.A. Belfiore, Polymer **45**(7), 2081 (2004)

[29] J. Mercier, Polymer Engineering & Science **30**(5), 270 (1990)

[30] C. Freitag, I. Riegel, S. Pezzin, M. Costa, S. Amico, Polymer Engineering & Science **51**(5), 931 (2011)

[31] P.R. Laity, J.E. Taylor, S.S. Wong, P. Khunkamchoo, M. Cable, G.T. Andrews, A.F. Johnson, R.E. Cameron, Macromolecular Materials and Engineering **291**(4), 301 (2006)

[32] C.E. Wilkes, C.S. Yusek, Journal of Macromolecular Science, Part B: Physics **7**(1), 157 (1973)

[33] J.T. Koberstein, R.S. Stein, Journal of Polymer Science: Polymer Physics Edition **21**(8), 1439 (1983)

[34] J.T. Koberstein, R.S. Stein, J. Polym. Sci., Polym. Phys. **21**(8), 1439 (1983)

[35] L.M. Leung, J.T. Koberstein, Journal of Polymer Science: Polymer Physics Edition **23**(9), 1883 (1985)

[36] J. Koberstein, A. Galambos, L. Leung, Macromolecules **25**(23), 6195 (1992)

[37] D. Attwood, *Soft x-rays and extreme ultraviolet radiation: principles and applications* (Cambridge university press, 1999)

[38] X-ray. https://en.wikipedia.org/wiki/X-ray/ (2013). [Online; accessed 11-July-2013]

[39] MetalJet X-Ray Tube Technology. http://www.excillum.com/technology/metal-jet-technology.html/. [Online; accessed 12-Feb-2017]

[40] K. Brüning, In-situ Structure Characterization of Elastomers during Deformation and Fracture. Ph.D. thesis, Technischen Universität Dresden (2014)

[41] N. Stribeck, in *Applications of Synchrotron Light to Scattering and Diffraction in Materials and Life Sciences*, *Lect. Notes Phys.*, vol. 776, ed. by T.A. Ezquerra, M. Garciá Gutiérrez, A. Nogales, M. Gómez (Springer, Berlin Heidelberg, 2009), chap. 2, pp. 25–62

[42] N. Stribeck, *X-Ray Scattering of Soft Matter* (Springer, Heidelberg, New York, 2007)

[43] P. Debye, A.M. Bueche, J. Appl. Phys. **20**(6), 518 (1949)

[44] G. Porod, Colloid Polym. Sci. **124**(2), 83 (1951)

[45] N. Stribeck, J. Appl. Cryst. **34**(4), 496 (2001)

[46] N. Stribeck, S. Fakirov, Macromolecules **34**(22), 7758 (2001)

[47] W. Ruland, Colloid Polym. Sci. **255**(5), 417 (1977)

[48] W. Ruland, Colloid Polym. Sci. **256**, 932 (1978)

[49] N. Stribeck, W. Ruland, J. Appl. Cryst. **11**(5), 535 (1978)

[50] J. Méring, D. Tchoubar-Vallat, C. R. Acad. Sc. Paris **261**, 3096 (1965)

[51] J. Méring, D. Tchoubar-Vallat, C. R. Acad. Sc. Paris **262**, 1703 (1966)

[52] J. Méring, D. Tchoubar, J. Appl. Cryst. **1**, 153 (1968)

[53] D. Tchoubar, J. Méring, J. Appl. Cryst. **2**, 128 (1969)

[54] W. Ruland, J. Appl. Cryst. **4**(1), 70 (1971)

[55] J.T. Koberstein, B. Morra, R.S. Stein, J. Appl. Cryst. **13**, 34 (1980)

[56] N. Stribeck, Anal. Bioanal. Chem. **376**(5), 608 (2003)

[57] N. Stribeck, ACS Symp. Ser. **739**, 41 (2000)

[58] N. Stribeck, Colloid Polym. Sci. **270**(1), 9 (1992)

[59] R. Bonart, Kolloid Z. u. Z. Polymere **211**, 14 (1966)

[60] A. Zeinolebadi, *In-situ Small-Angle X-ray Scattering Investigation of Transient Nanostructure of Multi-phase Polymer Materials Under Mechanical Deformation* (Springer Science & Business Media, 2013)

[61] D. Randall, S. Lee (eds.), *The Polyurethanes Book* (John Wiley {&} Sons, New York, 2003)

[62] N. Stribeck, U. Nöchel, S.S. Funari, T. Schubert, J. Polym. Sci. Polym. Phys. **46**(7), 721 (2008)

[63] N. Stribeck, in *Nano- and Micromechanics of Polymer Blends and Composites*, vol. 1, ed. by J. Karger-Kocsis, S. Fakirov (Hanser Publisher, Munich, 2009), chap. 8, pp. 269–300

[64] VNI. PV-WAVE manuals. V 7.5, Houston, TX, USA (2007)

[65] N. Stribeck, U. Nöchel, J. Appl. Cryst. **41**(4), 715 (2008)

[66] S. Ran, X. Zong, D. Fang, B.S. Hsiao, B. Chu, R.A. Phillips, Macromolecules **34**(8), 2569 (2001)

[67] A. Jánosi, Monatsh. f. Chemie **114**(4), 377 (1983)

[68] O. Glatter, O. Kratky (eds.), *Small Angle X-ray Scattering* (Academic Press, London, 1982)

[69] F.J. Baltá Calleja, C.G. Vonk, *X-Ray Scattering of Synthetic Polymers* (Elsevier, Amsterdam, 1989)

[70] C.G. Vonk, J. Appl. Cryst. **6**(2), 81 (1973)

[71] J. Rathje, W. Ruland, Colloid Polym. Sci. **254**, 358 (1976)

[72] N. Stribeck, X. Li, I. Kogut, H.U. Moritz, B. Eling, G.J. Goerigk, A. Hoell, Macromol. Mater. Eng. **300**(7), 699 (2015)

[73] N. Stribeck, A. Zeinolebadi, F. Harpen, G.A. Luinstra, B. Eling, S. Botta, Macromolecules **46**(10), 4041 (2013)

[74] A. Peterlin, J. Mater. Sci. **6**, 490 (1971)

[75] G. Porod, Fortschr. Hochpolym.-Forsch. **2**, 363 (1961)

[76] D.J. Blundell, G. Eeckhaut, W. Fuller, A. Mahendrasingam, C. Martin, Polymer **43**(19), 5197 (2002)

[77] N. Stribeck, X. Li, B. Eling, E. Pöselt, P. Veld, Journal of Applied Crystallography **48**(2), 0 (2015)

[78] R. Merlin, K. Bajema, R. Clarke, F.Y. Juang, P.K. Bhattacharya, Phys. Rev. Lett. **55**(17), 1768 (1985)

[79] X. Fu, Y. Liu, P. Zhou, W. Sritrakool, Phys. Rev. B **55**(5), 2882 (1997)

[80] C.G. Vonk, Colloid Polym. Sci. **257**, 1021 (1979)

[81] N. Stribeck, Colloid Polym. Sci. **271**(11), 1007 (1993)

[82] N. Stribeck, Colloid Polym. Sci. **280**(3), 254 (2002)

[83] J.J. Hermans, Rec. Trav. Chim. Pays-Bas **63**, 211 (1944)

[84] N. Stribeck, A. Almendarez Camarillo, R. Bayer, Macromol. Chem. Phys. **205**(11), 1463 (2004)

[85] A. Stribeck, X. Li, A. Zeinolebadi, E. Pöselt, B. Eling, S. Funari, Macromolecular Chemistry and Physics **216**(24), 2318 (2015)

[86] P.R. Laity, J.E. Taylor, S.S. Wong, P. Khunkamchoo, K. Norris, M. Cable, G.T. Andrews, A.F. Johnson, R.E. Cameron, Polymer **45**(21), 7273 (2004)

[87] A. Zeinolebadi, N. Stribeck, Z. Vuluga, C. Schloen, S. Botta, M. Ganjaee Sari, Polym. Adv. Technol. **24**(8), 693 (2013)

[88] N.R. Draper, H. Smith, *Applied Regression Analysis*, 2nd edn. (John Wiley {&} Sons, New York, 1980)

[89] N. Stribeck, Colloid Polym. Sci. **267**, 301 (1989)

[90] N. Stribeck, J. Phys. IV **3**(C8), 507 (1993)

[91] A. Stribeck, F. Jokari Sheshdeh, E. Pöselt, B. Eling, P.J. in't Veld, G.J. Goerigk, A. Hoell, J. Polym. Sci. Polym. Phys. **53**(17), 1213 (2015)

[92] A. Stribeck, X. Li, A. Zeinolebadi, E. Pöselt, B. Eling, S. Funari, Macromol. Chem. Phys. **submitted** (2015)

[93] P.J. Flory, J. Chem. Phys. **15**(6), 397 (1947)

[94] E.H. Andrews, J. Polym. Sci. Part A2 Polym. Phys. **4**(4), 668 (1966)

[95] T.L. Smith, J. Polym. Sci. Polym. Phys. **12**(9), 1825 (1974)

[96] D.K. Lee, H.B. Tsai, Journal of applied polymer science **75**(1), 167 (2000)

[97] M. Corcuera, L. Rueda, A. Saralegui, M. Martín, B. Fernández-d'Arlas, I. Mondragon, A. Eceiza, et al., Journal of Applied Polymer Science **122**(6), 3677 (2011)

[98] J.H. Wendorff, E.W. Fischer, Colloid Polym. Sci. **251**, 876 (1973)

[99] W. Wiegand, W. Ruland, Progr. Colloid Polym. Sci. **66**, 355 (1979)

[100] S. Sasaki, K. Tashiro, M. Kobayashi, Y. Izumi, K. Kobayashi, Polymer **40**(25), 7125 (1999)

[101] R. Bonart, Polymer **20**(11), 1389 (1979)

[102] R. Bonart, J. Macromol. Sci. Part B: Physics **2**(1), 115 (1968)

[103] L. Morbitzer, H. Hespe, Journal of Applied Polymer Science **16**(10), 2697 (1972)

[104] R.W. Seymour, S.L. Cooper, Macromolecules, **6**(1), 48 (1973)

[105] T.M. Madkour, S.K. Mohamed, J. Appl. Cryst. **46**(4), 980 (2013)

Index

Acknowledgments

The present work was made during my work as a research associate at the Institute of TMC in department of chemistry university Hamburg and BASF polyurethanes GmbH in Lemförde, Germany. The work on this thesis has generously been supported by a grant issued by BASF Polyurethanes. Without this support, it would have failed due to financial reasons, because my source of funding originally provided for could not be realized. My deep gratitude therefore applies in particular to Dr. Eipper and Prof. Dr. Eling from BASF as well as to my supervisor Prof. Dr. Stribeck. I would like to express my greatest thanks to Prof. Dr. Almut Sandra Stribeck for her professional supervision of the work. Without her unceasing support this thesis would not be a reality. Special thanks to BASF Polyurethanes GmbH for such a great professional and personal opportunity. I appreciate Prof. Dr. Berend Eling and Dr. Elmar Pöselt (BASF Polyurethanes GmbH) for their scientific support in Polyurethane chemistry science. The BESSY and the Helmholtz-Zentrum Berlin, I thank for the granting of measuring time at synchrotron beamline 7T-MPW-SAXS. For a great time with challenging experiments, interesting results and an inspiring working environment, I thank the teams of beamline: Dr. Armin Hoell and Dr. Günter Johannes Goerigk. I also would like to thank Dr. Ahmad Zeinolebadi from Polymer Consult Buchner GmbH and my colleagues at Hamburg University, in particular Dr. Xuke Li for their friendly help.

publication

1. Almut Stribeck, Farhad Jokari-Sheshdeh, Elmar Pöselt, Berend Eling, Pieter J. in't Veld, Günter Johannes Goerigk, Armin Hoell, "Machine prepared thermoplastic polyurethanes of varying hard segment content: Morphology and its evolution in tensile tests" , Journal of Polymer Science Part B: Polymer Physics, Volume 53, Issue 17, 1 September 2015 Pages 1213–1223.

list of hazardous

In this work, no hazardous substances used.

Hamburg, 10/01/2017

Farhad Jokari-Sheshdeh

Declaration on oath

I hereby declare on oath, that I have written the present dissertation by my own and have not used other than the acknowledged resources and aids. I hereby declare that I have not previously applied or pursued for a doctorate (Ph.D. studies).

Hamburg, 10/01/2017

Farhad Jokari-Sheshdeh